

**ANALYSIS OF HOT SPRINGS IN YELLOWSTONE NATIONAL PARK USING ASTER  
AND AVIRIS REMOTE SENSING**

by

Melanie J. Hellman

BS, Brandeis University, 1998

Submitted to the Graduate Faculty of  
Arts and Sciences in partial fulfillment  
of the requirements for the degree of  
Masters of Science

University of Pittsburgh

2002

UNIVERSITY OF PITTSBURGH

---

FACULTY OF ARTS AND SCIENCES

This thesis was presented

by

Melanie J. Hellman

---

It was defended on

July 16, 2002

---

and approved by

---

David Crown

---

Brian Stewart

---

Michael Ramsey

---

Dissertation Director

# ANALYSIS OF HOT SPRINGS IN YELLOWSTONE NATIONAL PARK USING ASTER AND AVIRIS REMOTE SENSING

Melanie J. Hellman, M.S.

University of Pittsburgh, 2002

Data from Advanced Spaceborne Thermal Emission and Reflection Radiometer (ASTER) and the Airborne Visible/IR Image Spectrometer (AVIRIS) were used to characterize hot spring deposits in the Lower, Midway, and Upper Geyser Basins of Yellowstone National Park at the visible/near infrared (VNIR) to thermal infrared (TIR) wavelengths. Field observations of these basins provided the critical ground truth for comparison to the remote sensing results. Fourteen study sites were selected based on diversity in size, deposit type, and thermal activity. Field work included detailed site surveys such as land cover analysis, photography, Global Positioning System (GPS) data collection, radiometric analysis, and VNIR spectroscopy. Samples of hot spring deposits, geyser deposits, and soil were also collected. Analysis of ASTER provided broad scale characteristics of the hot springs and their deposits, including the identification of thermal anomalies. AVIRIS high-spectral-resolution, short-wave infrared (SWIR) spectroscopy provided the ability to detect hydrothermally altered minerals as well as a calibration for the multispectral SWIR ASTER data. From the image analysis, differences in these basins were identified including the extent of thermal alteration, the location and abundance of alteration minerals, and differences between active, near-extinct, and extinct geysers. The activity level of each region was determined using a combination of the VNIR-SWIR-TIR spectral differences as well as the presence of elevated temperatures, detected by the TIR subsystem of ASTER. The results of this study can be applied to the exploration of extinct mineralized hydrothermal deposits on both Earth and Mars.

## ACKNOWLEDGMENTS

The author wishes to thank the National Park Service and the Yellowstone Research Permit Office, especially Christine Hendrix, Ann Rodman, Steve Miller, and Nancy Hinman, who made this field work possible. Michael Ramsey, my thesis advisor, for his guidance in this research and field assistance. Steve Anderson, Ava Horowitz, Mike Keller, and Rocco Paperiello provided helpful guidance and assistance on the research. In addition, William Stefanov provided use of the VNIR field spectrometer, and Robert O. Green and James Granahan provided access to the AVIRIS data and the atmospheric correction software. Thanks to David Crown and Brian Stewart for committee membership and providing excellent reviews that greatly improved this work. Research funding for this study has been provided by the NASA Solid Earth and Natural Hazards Program (NAG5-9439) as well as the ASTER science project.

## DEDICATION

*I dedicate this work to all of those who have helped me along the way. Without their continued support, this would only be a dream, not a reality. This is also dedicated to my little plaque, forever reminding me that it is never easy reaching for dreams, but those who do, walk in stardust. We are all in the gutter, but some of us are looking at the stars.*

## TABLE OF CONTENTS

Introduction: Thermal Springs and Remote Sensing .....	1
Section 1: Remote Sensing Background.....	4
I. General Background.....	4
II. Instrument Descriptions .....	5
A. AVIRIS .....	5
B. ASTER .....	6
C. TES.....	6
D. THEMIS.....	7
III. Mineral Detection Using Remote Sensing.....	8
Section 2: Geology of the Yellowstone Volcanic Region .....	12
I. General Background.....	12
II. Geysers and Hot Springs .....	13
III. Lower Geyser Basin (LGB).....	17
IV. Midway Geyser Basin (MGB).....	18
V. Upper Geyser Basin (UGB).....	18
Section 3: Methodology.....	21
I. Field Site Selection and Description .....	21
A. Site 1, White Creek Group.....	22
B. Site 2, Firehole Lake Group.....	22
C. Site 3, Myriad Group.....	23
D. Site 4, Fortress Geyser .....	24
E. Site 5, Rabbit Creek Hot Springs .....	24
F. Site 6, Morning Mist Springs.....	25
G. Site 7, Fountain Flats .....	25
H. Site 8, Extinct in Firehole .....	26
I. Site 9, Sunset Lake .....	26
J. Site 10, Sapphire Pool .....	26
K. Site 11, Mallard Lake.....	27
L. Site 12, Iris Group .....	27
M. Site 13, White Dome .....	28
N. Site 14, Fracture Group.....	28
II. Site Surveys.....	29
III. ASTER Data Acquisition and Processing.....	30
IV. AVIRIS Data Acquisition and Processing.....	31
Section 4: Results.....	64
I. Reflectance .....	64
A. Field-Based VNIR Reflectance Spectra.....	64
B. ASTER and AVIRIS VNIR Reflectance Spectra .....	65
C. ASTER and AVIRIS SWIR Reflectance .....	66

II. ASTER and AVIRIS Color Composites and Band Ratios.....	68
III. ASTER TIR Emissivity and Temperature .....	69
IV. Normalized Difference Vegetation Index (NDVI).....	71
V. Classifications .....	72
A. Unsupervised Classification.....	72
B. Supervised Classification .....	74
C. Spectral Angle Mapper.....	75
Section 5: Discussion.....	100
Section 6: Application to Mars .....	103
Section 7: Conclusions.....	113
Appendix A.....	117
Field VNIR Spectra (including GPS coordinates and field radiometric temperatures).....	117
Appendix B.....	157
ASTER and AVIRIS VNIR Reflectance Spectra .....	157
Appendix C .....	164
ASTER and AVIRIS SWIR Reflectance Spectra.....	164
Appendix D.....	171
ASTER TIR Emissivity Spectra .....	171
Appendix E .....	180
List of Commonly Used Acronyms .....	180
References.....	183

## LIST OF TABLES

<b>Table 1 Description of Field Sites.....</b>	<b>33</b>
<b>Table 2 Initial stage of georectification: Metadata information.....</b>	<b>34</b>
<b>Table 3 Second stage of georectification: Using GPS.....</b>	<b>35</b>
<b>Table 4 ASTER 4/6 and AVIRIS 139/195 SWIR band ratios.....</b>	<b>77</b>
<b>Table 5 ASTER Radiance values for the fourteen field sites.....</b>	<b>78</b>
<b>Table 6 Shape of emissivity spectra for the fourteen field sites.....</b>	<b>79</b>
<b>Table 7 Depth of the 9.2 <math>\mu\text{m}</math> feature.....</b>	<b>80</b>
<b>Table 8 Kinetic Temperatures for the fourteen field sites.....</b>	<b>81</b>
<b>Table 9 NDVI values for the fourteen field sites.....</b>	<b>82</b>
<b>Table 10 Class statistics for unsupervised k-means classification.....</b>	<b>83</b>
<b>Table 11 Class statistics for the supervised classification.....</b>	<b>84</b>
<b>Table 12 Planned instruments for the MER 2003 Mars mission.....</b>	<b>108</b>

## LIST OF FIGURES

<b>Figure 1 Comparison of TES and THEMIS.....</b>	<b>11</b>
<b>Figure 2 Yellowstone location map showing active and fossil hydrothermal systems .....</b>	<b>19</b>
<b>Figure 3 AVIRIS visible reflectance image of the LGB, MGB, and UGB.....</b>	<b>20</b>
<b>Figure 4a Location map of the LGB .....</b>	<b>36</b>
<b>Figure 4b Location map of the MGB .....</b>	<b>37</b>
<b>Figure 4c Location map of the UGB .....</b>	<b>38</b>
<b>Figure 5a Field photograph of Site 1.....</b>	<b>39</b>
<b>Figure 5b Field photograph of Site 2.....</b>	<b>40</b>
<b>Figure 5c Field photograph of Site 3 .....</b>	<b>41</b>
<b>Figure 5d Field photograph of Site 4.....</b>	<b>42</b>
<b>Figure 5e Field photograph of Site 5 .....</b>	<b>43</b>
<b>Figure 5f Field photograph of Site 6 .....</b>	<b>44</b>
<b>Figure 5g Field photograph of Site 7.....</b>	<b>45</b>
<b>Figure 5h Field photograph of Site 8.....</b>	<b>46</b>
<b>Figure 5i Field photograph of Site 9.....</b>	<b>47</b>
<b>Figure 5j Field photograph of Site 10 .....</b>	<b>48</b>
<b>Figure 5k Field photograph of Site 11.....</b>	<b>49</b>
<b>Figure 5l Field photograph of Site 12.....</b>	<b>50</b>
<b>Figure 5m Field photograph of Site 13 .....</b>	<b>51</b>
<b>Figure 5n Field photograph of Site 14.....</b>	<b>52</b>
<b>Figure 6a Close up view of hard pink geyserite .....</b>	<b>53</b>
<b>Figure 6b Close up view of fractured sinter .....</b>	<b>54</b>
<b>Figure 6c Close up view of finely powdered sinter .....</b>	<b>55</b>
<b>Figure 6d Close up view of hard sinter cement.....</b>	<b>56</b>
<b>Figure 6e Close up view of dry, brittle fragmental sinter .....</b>	<b>57</b>
<b>Figure 6f Close up view of sinter needles.....</b>	<b>58</b>
<b>Figure 6g Knobby biscuit-like sinter formations .....</b>	<b>59</b>
<b>Figure 6h Wet opaline geyserite + mat .....</b>	<b>60</b>
<b>Figure 6i Banded opaline and chalcedonic sinter .....</b>	<b>61</b>
<b>Figure 7a ASTER VNIR image of LGB and MGB.....</b>	<b>62</b>
<b>Figure 7b ASTER VNIR image of UGB .....</b>	<b>63</b>
<b>Figure 8a Example of the VNIR field spectra of an active site.....</b>	<b>85</b>
<b>Figure 8b Example of the VNIR field spectra of an extinct site .....</b>	<b>86</b>
<b>Figure 9 ASTER VNIR reflectance spectra of an active and extinct site .....</b>	<b>87</b>
<b>Figure 10 AVIRIS and ASTER SWIR reflectance spectra of an active site .....</b>	<b>88</b>
<b>Figure 11 AVIRIS and ASTER SWIR reflectance spectra of an extinct site.....</b>	<b>89</b>
<b>Figure 12 ASTER RGB color composite of the LGB and MGB .....</b>	<b>90</b>
<b>Figure 13 ASTER RGB color composite of the UGB .....</b>	<b>91</b>

<b>Figure 14 ASTER TIR image of the LGB and MGB .....</b>	<b>92</b>
<b>Figure 15a Typical emissivity spectra of an active site.....</b>	<b>93</b>
<b>Figure 15b Typical emissivity spectra of an extinct site.....</b>	<b>94</b>
<b>Figure 16a Unsupervised k-means classification of the LGB and MGB .....</b>	<b>95</b>
<b>Figure 16b Unsupervised k-means classification of the UGB.....</b>	<b>96</b>
<b>Figure 17a Supervised maximum likelihood classification of the LGB and MGB.....</b>	<b>97</b>
<b>Figure 17b Supervised maximum likelihood classification of the UGB .....</b>	<b>98</b>
<b>Figure 18 Spectral angle mapper classification of the LGB .....</b>	<b>99</b>
<b>Figure 19 Hematite concentration in Sinus Meridiani region of Mars, measured by TES</b>	<b>109</b>
<b>Figure 20 THEMIS VNIR image of Terra Meridiani, Mars .....</b>	<b>110</b>
<b>Figure 21 Location map of the proposed landing sites for 2003 MER. ....</b>	<b>111</b>
<b>Figure 22 Evaluation criteria for the top landing sites for 2003 MER .....</b>	<b>112</b>

## **Introduction: Thermal Springs and Remote Sensing**

There are thousands of known thermal springs on Earth, with the most abundant located in volcanic areas, such as the Yellowstone Caldera, New Zealand, and Iceland [Walter and DesMarais, 1993; Bryan, 2000]. Thermal spring deposits are produced by intense hydrothermal alteration of the surrounding parent rock. As spring waters cool, solubility rapidly decreases and sinter is deposited in springs [Walter and DesMarais, 1993]. Sinters, the chemical precipitates of hydrothermal systems, generally consist of minerals dominated by silica, carbonate, metallic sulfides and oxides, and clays [Farmer, 2000].

Hydrothermal systems may have been crucial to the early evolution of life and thermophilic organisms may be the common ancestors to all terrestrial life. The search for extant or extinct life on Mars and other planetary bodies has been of major importance to the NASA Astrobiology program. By using the Earth as an analogue, researchers suggest that if Martian life developed, it would have been in close association with hydrothermal systems [Farmer, 1999]. Finding potential hydrothermal sites is a high priority in Martian exploration, and possible hydrothermal activity has been suggested for numerous sites on Mars [Bulmer and Gregg, 1998; Dohm et al., 2000; Farmer, 1998; Gulick, 1998, Nelson et al., 1999].

Investigators including Christiansen et al. (1984) and Fournier and Pitt (1985) extensively described the geological and geophysical characteristics of Yellowstone. Most of the geyser basins have chloride rich waters that are neutral to slightly alkaline [Fournier, 1989]. The hydrothermal fluids from the basins range in temperature from 180 to 270° C at minimum depths

of 100 to 550 m [Fournier, 1989]. Bargar and Fournier (1988) sampled fluid inclusions in the hydrothermal minerals. They determined that hydrothermal activity has operated at its present level from the end of last glaciation (at least 15 ka). Previous studies have found abundant microfossil evidence in Yellowstone's lower temperature thermal spring deposits [Farmer et al., 1995; Farmer and DesMarais, 1999].

There has also been a renewed interest in Yellowstone's hot springs because of the potential medical applications of thermophilic organisms. For instance, the bacterium *Thermus aquaticus* was discovered in springs near the Great Fountain Geyser of the Lower Geyser Basin [Brock, 1994]. The bacteria contain Taq polymerase, an enzyme that has been cultured and is now the basis of a \$300 million industry; the enzyme is widely being used in medical diagnosis and forensics to copy and amplify DNA [Brock, 1994].

The present study focuses on extinct to active hot springs and hot spring deposits of the Lower, Midway, and Upper Geyser Basins in Yellowstone. ASTER (Advanced Spaceborne Thermal Emission and Reflection Radiometer) and AVIRIS (Airborne Visible/Infrared Image Spectrometer) data analysis was combined with field mapping of the hydrothermal deposits in order to detect differences in the size, activity, and mineralogy of the deposits [Hellman and Ramsey, 2001, 2002]. Yellowstone National Park was chosen for this study for several reasons: (1) it has the greatest concentration of geysers and hot springs on Earth; (2) the geyser basins typify the surface expression of a high-temperature hot-water system [Fournier, 1989]; (3) the preservation of these thermal features allows for a comprehensive study of their deposits; and (4) the remote sensing data availability was far greater than for other hydrothermal sites. The Lower, Midway, and Upper Geyser Basins of Yellowstone National Park were chosen for this study. The Lower Geyser Basin was selected because it is the largest thermal area in

Yellowstone. This large area allows for remote sensing studies using decreased spatial resolutions, that can be advantageous for planetary comparisons. Also, this basin has a diverse variety of active and extinct springs. The Midway Geyser Basin was chosen because it is essentially an extension of the Lower Geyser Basin. The Upper Geyser Basin was selected because it has the largest concentration of geysers in the world, allowing for remote sensing observations of intense thermal activity in a relatively small area.

The primary goal of this study was to compare and contrast the characteristics of Yellowstone's active and extinct hot springs. These characteristics were distinguished using field-based, airborne and spaceborne-based reflectance, emissivity and temperature, as well as various image processing techniques, such as band ratioing and classification algorithms. Because remote sensing instruments are commonly used in planetary studies and field-based validation may not be possible for other planetary bodies, this type of terrestrial remote sensing analysis can be useful for planetary comparisons. Potential active or extinct hot springs may be detected on Mars using similar techniques implemented in this study.

## **Section 1: Remote Sensing Background**

### **I. General Background**

The earliest use of satellite geological remote sensing was for mineral exploration in the 1970s [Vincent, 1997]. Abrams et al. (1977) identified hydrothermal alteration minerals in the Cuprite mining district from a NASA airborne multispectral scanner, but could only map altered rocks based on the absence of iron oxide and clay minerals. Several years later, Vincent et al. (1984) implemented multispectral airborne and spaceborne thermal data to map the Cuprite district on the basis of silica content. Most satellite sensors, such as Landsat Thematic Mapper (TM), do not have the needed spectral resolution to identify specific mineral spectral features [Sabins, 1999]. However, numerous studies have been done with multispectral remote sensing for the purposes of broad hydrothermal mineralization detection. Ruiz-Armenta and Prol-Ledesma (1996) studied the TM spectral response of hydrothermal alteration minerals in an area of the Transmexican Volcanic Belt. The two best techniques for enhancing the detection of the alteration were (1) principal components analysis, that is a statistical analysis to decorrelate the satellite image bands, and (2) HSI (hue, saturation, intensity) transformation, that is a simple non-linear transformation that can achieve a stronger color sense of an image without the larger statistical process of decorrelation.

## **II. Instrument Descriptions**

### **A. AVIRIS**

The AVIRIS instrument is a hyperspectral airborne instrument flown in a NASA high-altitude aircraft [Vane et al., 1987; Green et al. 1998; Rowan, 2000]. It is commonly used for quantitative mineral mapping, vegetation surveys and as a calibration for spaceborne VNIR (visible to near-infrared) instruments [Hook and Rast, 1990; Clark, 1991; Kruse, 1999]. Radiance data are recorded in 224 contiguous bands from the visible blue to the short-wave infrared region (0.4 – 2.5  $\mu\text{m}$ ), in swath widths that are commonly tens of kilometers long [Sabins, 1999]. The spectral sampling interval is  $\leq 10$  nm [Macenka and Chrisp, 1987]. The ER-2 aircraft flies at the standard flight altitude (20 km), collecting data at the 20 m/pixel spatial resolution for all wavelengths. At the low altitude (1.83 km – 5.334 km), the Twin Otter aircraft collects data at a 4 m/pixel spatial resolution.

The AVIRIS instrument itself consists of six optical subsystems and five electrical subsystems [Porter and Enmark, 1987]. The optics subsystem consists of a whiskbroom scanner connected by optical fibers to four spectrometers. An onboard reference source is also connected by optical fibers to the spectrometers, providing information for spectral and radiometric calibration [Macenka and Chrisp, 1987]. In the spectrometers, the dispersed spectrum is imaged on cooled linear arrays of silicon detectors for the VNIR spectral range, and on iridium antimonide arrays for the NIR (near-infrared) spectral range [Macenka and Chrisp, 1987]. Data encoding was 10 bit through 1994, and 12 bit from 1995. AVIRIS operations are controlled by the AVIRIS Science Team, the Data Facility Team (DFT), and the Instrument Team. All the data are processed by the AVIRIS Data Facility at the Jet Propulsion Laboratory (JPL). Refer to <http://malaku.jpl.nasa.gov/aviris.html> for more information.

## **B. ASTER**

The ASTER sensor is an imaging instrument currently flying on the Terra satellite [Yamaguchi et al. 1998; Ramsey and Flynn, 2002]. It was launched in December 1999 as part of NASA's Earth Observing System (EOS), and has a science team composed of members from the United States, Japan, France and Australia.

ASTER contains three separate instrument subsystems (VNIR, SWIR (short-wave infrared), and TIR (thermal infrared)) with 14 bands from the visible green to the thermal infrared (0.52 – 11.65  $\mu\text{m}$ ). The instrument has a swath width of 60 km and a spatial resolution of 15, 30 and 90 m/pixel, in the VNIR, SWIR and TIR regions, respectively [Kahle et al., 1991]. Data are quantized as 8 bit for the VNIR and SWIR, and 12 bit for TIR. The VNIR subsystem has both a nadir-looking and backward-looking telescope used for the generation of optically-derived digital elevation models (DEMs). The SWIR subsystem uses a single fixed refracting telescope; a platinum silicide-silicon detector is used in each SWIR channel. The TIR subsystem uses a Newtonian system with a primary mirror and lens. The telescope of the TIR subsystem is fixed and the mirror executes the pointing and scanning. Ten Mercury-Cadmium-Telluride detectors are in each TIR channel. A high emissivity reference plate is used as an on-board calibration reference for the TIR subsystem. Refer to <http://asterweb.jpl.nasa.gov/> for more information.

## **C. TES**

Exploration of the Martian surface using remote sensing has been ongoing for nearly four decades. TIR remote sensing has been one of the fundamental datasets used to assess the surface temperature, mineralogy, surface rock abundance, and atmospheric composition [Christensen et al. 2000a]. Current TIR instruments such as the Thermal Emission Spectrometer (TES) are continuing this legacy with increasing spatial and spectral resolutions [Christensen et al., 2000b].

The TES instrument is currently onboard the Mars Global Surveyor. TES is composed of three subsystems, a Michelson interferometer, radiance sensor, and a solar reflectance sensor. The interferometer spans from 6 to 50 microns and has a 5 and 10  $\text{cm}^{-1}$  spectral resolution. The radiance sensor measures single band radiance from 5.5 to 100 microns. The reflectance sensor ranges 0.3 to 2.7 microns. The spatial resolution of TES is 3 km/pixel. TES can produce 2D images and emissivity spectra. TES is capable of identifying most crystalline minerals that occur in large regions on Mars, spanning tens of kilometers or more [Bishop, 2001]. Refer to <http://tes.asu.edu/> for more information.

#### **D. THEMIS**

With the recent emphasis on water and the search for potential life indicators on Mars, the emphasis has shifted to higher spatial resolution data in order to map potentially smaller deposits [Farmer et al. 2000]. The new THEMIS (Thermal Emission Imaging System) instrument has ten multispectral thermal bands (100 m/pixel spatial resolution) in the 6.5-14.5 micron region as well as 5 bands (20 m/pixel spatial resolution) in the VNIR [Christensen et al., 1999]. The increased spatial resolution may allow for more detailed mineral mapping on Mars, compared to the current 3 km/pixel resolution of TES (Figure 1). The primary goal of the THEMIS instrument, onboard the Mars Odyssey spacecraft, is to identify areas of past hydrothermal activity and determine the associated mineralogy. A secondary goal is to search for thermal anomalies associated with still-active hot springs on Mars [Christensen et al., 1999]. Potential hydrothermal sites identified by THEMIS would likely become candidates for future landing sites and sample return missions. Refer to <http://themis.la.asu.edu/> for more information.

Because detection of potential Mars relict hot springs will be done remotely, it is important to understand how to detect and study these deposits on Earth. The THEMIS spatial and spectral resolutions are comparable to ASTER. This similarity allows ASTER data to be

used as a terrestrial proxy for studies of geologic processes that have operated or are now operating on the Martian surface. Because the commonly required field-based validation necessary to verify model and mapping results is not possible at Mars, it is useful to take advantage of terrestrial analog site studies such as the hydrothermal features of Yellowstone Caldera.

### **III. Mineral Detection Using Remote Sensing**

Thermal springs and their associated deposits have distinctive chemical signatures detectable by remote sensing [Walter and DesMarais 1993, Ruiz-Armenta and Prol-Ledesma, 1998]. Laboratory-based Mössbauer spectroscopy was used to successfully identify hydrothermal alteration minerals near the vent, on the surface, and in the subsurface of iron-rich springs at Yellowstone [Wade et al. 1999]. Other common remote sensing techniques include VNIR, SWIR, and TIR spectroscopy, and emissivity and temperature extraction. Various image processing techniques include band ratioing, supervised and unsupervised classification techniques, and decorrelation stretching.

Weathered or altered iron oxides are detected in the visible to near-infrared region (VNIR) with silicon sensing technology [Huntington, 1992]. In the VNIR, materials containing  $\text{Fe}^{2+}$ ,  $\text{Fe}^{3+}$ , Mn, Cr, and Ni produce different and identifiable spectra. There are variations in iron oxide species; for example, hematite is more abundant in stable landscapes, whereas goethite more common in active erosional or depositional environments [Huntington, 1992]. Goethite is a secondary iron mineral and forms in all types of hydrothermal replacement deposits [Chesterman, 1979]. Aluminum substitution in iron oxides causes a wavelength variation of the

850-900 nm iron oxide crystal field absorption [Huntington, 1992]. The VNIR is also the region for chlorophyll absorption [Huntington, 1992].

The short-wave infrared region (SWIR) is the overall best region for sensing the products of hydrothermal alteration. Many clay minerals are bleached and hard to identify by the eye without SWIR remote sensing. Therefore, this is the best wavelength region to explore for hydroxyl bearing clays, sulfates and carbonate minerals that occur in and typify hydrothermal alteration systems. The primary objective in this wavelength region is to map the spatial distribution and zones of hydrothermal alteration minerals containing OH<sup>-</sup> groups.

Phyllosilicates, Al(OH)- and Mg(OH)-bearing minerals, OH-bearing sulfates, ammonium bearing minerals, and carbonates can be mapped with SWIR. Pixels that have mixed spectral signatures can be separated, and semi-quantitative mineral abundance maps can be produced free of the diluting effects of vegetation; separation is possible in areas of up to 50% vegetation [Huntington, 1992]. Detection of small proportions of some minerals is possible; targets such as veins that are smaller than a pixel may be mapped if they contain spectrally contrasting materials. It is possible to map chemical substitutions, involving Na, K, Al, Mg, and Fe in SWIR spectra of micas, biotites, alunites, carbonates, and chlorites, as changes in cation composition give rise to measurable wavelength shifts. For example, K-rich mica (muscovite) has a measurable absorption band at 2207 nm. However, a cation change from potassium to sodium gives rise to Na-rich mica (paragonite). Paragonite has a shifted absorption band at 2189 nm.

SWIR (2 - 2.5  $\mu\text{m}$ ) remote sensing can be used to identify hydrothermal alteration deposits such as clay mineralogy [Hook and Rast, 1990; Clark et al. 1991]. Clark (1993), Kokaly et al. (1998), and Kruse (1999) performed studies of Yellowstone's thermal areas using AVIRIS for mineral mapping. Kokaly et al. (1998) created mineral maps from AVIRIS data. These maps

showed the difference between the cooler, alkaline geyser basins and the hotter, acidic geyser basins, as a change in detected minerals from siliceous sinter and montmorillonite to alunite and kaolinite.

In addition to having visible and short wave infrared bands, ASTER has five 90 m resolution thermal infrared bands. This capability is useful where dealing with areas of thermal activity, such as the Yellowstone hot springs. ASTER provides regional coverage useful for the overall characteristics of these hydrothermal systems on a larger scale. ASTER also can be useful for the identification of hydrothermal silica [Sabins, 1999]. The TIR region is extremely useful in mapping rock-forming minerals. For example, Ramsey et al. (1999) discriminated mineralogical variations, including quartz content, within the Kelso sand dunes using TIMS (Thermal Infrared Multispectral Scanner) imagery. Hook et al. (1994) successfully implemented TIMS data to detected variations in silicate mineralogy and map the complex metamorphosed igneous and sedimentary rocks of the Piute Mountains.

Huntington (1992) proposed a plan for detection for terrestrial and other potential planetary hydrothermal minerals. This includes field based mapping for ground-truthing purposes using field spectrometers, airborne mapping for detailed studies, and satellite mapping for regional scale characteristics. The proposal included an orbiting hyperspectral imaging system that can identify hydrous alteration minerals in places where the Martian surface has been disrupted by erosion or volcanic activity. An unmanned Fourier-transform VNIR spectrometer rover (400-2500 nm) was also proposed to detect the spectral signatures of these minerals.

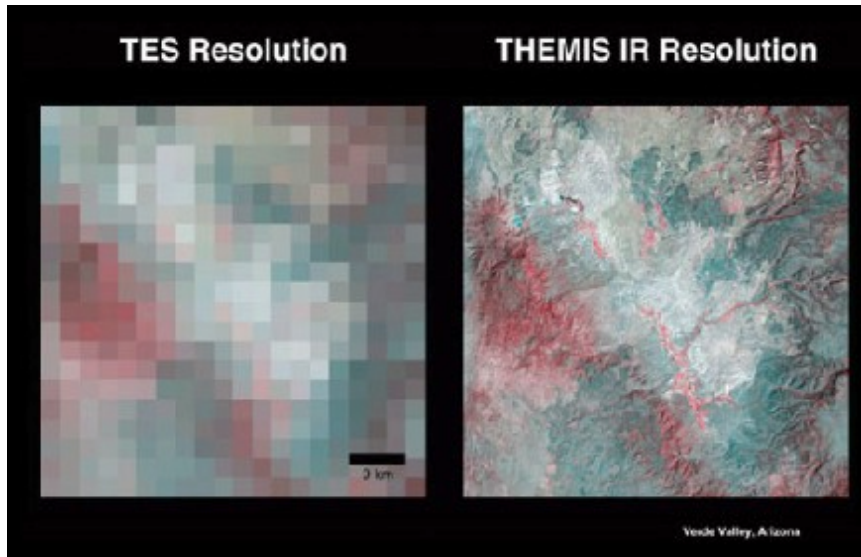


**Figure 1** Comparison of TES (3km/pixel) and THEMIS (100m/pixel) spatial resolutions (<http://tes.asu.edu>).

## **Section 2: Geology of the Yellowstone Volcanic Region**

### **I. General Background**

The present geothermal activity of Yellowstone is a result of large-scale extrusive volcanism that began 2 Ma and continued until about 70 ka [Christiansen, 1984; Walter and DesMarais, 1993]. The Yellowstone plateau is composed of rhyolites, rhyolitic welded tufts and basalts [Christiansen, 1984; Walter and DesMarais, 1993]. The distribution of active and recently-active hydrothermal features in Yellowstone is shown in Figure 2. Most of the hydrothermal features are located in the 0.6 Ma caldera, near the outer edge of the main ring fracture zone, or at the margins of the two resurgent domes [Fournier, 1989]. Springs are scattered over several 1000 km<sup>2</sup> and there are approximately 3000 springs in about 100 clusters [Walter and DesMarais, 1993]. Many clusters are grouped into geyser basins, that are areas of intensive geothermal activity [Walter and DesMarais, 1993].

Three major caldera-forming eruptions occurred in the Greater Yellowstone ecosystem. The first and largest of these was at 2 Ma and created the Island Park Caldera (volume > 2450 km<sup>3</sup>). This eruption produced more than 2500 times the volume of volcanic material as the 1980 eruption of Mt. St. Helens Volcano [Christiansen, 1982; Embree and Hoggan, 1999]. The remaining trace of this caldera rim, known as the Big Bend ridge, lies beyond the southern park border and extends west into Island Park, Idaho [Fritz, 1985; Embree and Hoggan, 1999]. The

welded Huckleberry Ridge Tuff produced from this cycle covers much of the Yellowstone region, lying on older rhyolite and basalt lava flows [Fritz, 1985; Embree and Hoggan, 1999].

At approximately 1.3 Ma, the second large eruption produced Henry's Fork Caldera, a smaller caldera centered around the Island Park, Idaho region [Christiansen, 1984; Embree and Hoggan, 1999]. This eruption formed the Mesa Falls Tuff, an ignimbrite sheet with a volume of  $> 2700 \text{ km}^3$  [Christiansen, 1982; Embree and Hoggan, 1999]. This unit consists primarily of pyroclastic flows outside of the park in Idaho [Fritz, 1985].

The third and last large eruption (0.6 Ma) created the present-day Yellowstone caldera (75 km x 45 km) and Lava Creek Tuff of central Yellowstone National Park [Christiansen, 1984]. Although some of the caldera rim has been covered by subsequent lava flows, much of the rim remains as a series of low hills along the central plateau. This last major series of eruptions produced about  $1000 \text{ km}^3$  of welded-ash and basalt flows, covering much of the park [Christiansen, 1982; Fritz, 1985; Embree and Hoggan, 1999].

Fissure eruptions of intermittent size have occurred after the last caldera-forming eruption (600 – 70 ka). The "West Thumb" of Yellowstone Lake is a secondary caldera produced by a smaller eruption approximately 150 ka. The Pitchstone Plateau was formed by the youngest rhyolite flows between 80 and 70 ka, and marks the last time lava flows have been erupted in the caldera [Fritz, 1985].

## **II. Geysers and Hot Springs**

Geysers are essentially hot springs that become thermodynamically and hydrodynamically unstable. Every geyser field in the world is located near a volcanic, shallow heat source. Geyser fields generally located near lithospheric plate boundaries, typically

characterized by active volcanism. Other geyser fields, such as Yellowstone, are assumed to lie above hot spots or plumes. The majority of all geyser fields lie above large bodies of rhyolite, although some fields are associated with more mafic volcanic rocks, including andesite or basalt. However, geysers are extremely rare on Earth. There are only approximately fifty geyser fields known to exist and about two-thirds contain five or fewer active geysers [Bryan, 2000]. Yellowstone has more geysers than any other known field, by nearly an order of magnitude. The three essential elements of a geyser are: 1) an abundant water supply, 2) a potent heat source, and 3) a reservoir and associated plumbing system [Bryan, 1995]. However, there are many other factors that influence the type and frequency of eruptions.

The vast majority of water in a geyser system is meteoric. Geothermal features are located where rainwater and snowmelt percolate into the ground and cycle back up again through layers of porous rock. This cycling process can take several hundred to several thousand years. The length of the cycle can be determined by measuring the tritium content in the geyser water; younger water contains considerable tritium, whereas older water contains little to no tritium [Bryan, 1995]. Tritium is nearly absent in most Yellowstone waters; tritium content shows the groundwater expelled from a typical geyser system is about 500 years old [Bryan, 1995].

The eruptive pattern for geysers is as follows, as summarized by Bryan, 1995. At a depth of nearly 3,000 meters, water is heated to temperatures over 200 °C through contact with volcanic rocks associated with the shallow magma chamber beneath the surface. Some of the water flashes to steam because the water temperature is well above boiling. Additional cooler water also flows into the geyser from the porous rocks closer to the surface. The steam bubbles formed at depth rise and interact with the cooler water, creating convection currents within the plumbing system. This allows the steam bubbles to eventually rise, heating the surface water

until it reaches boiling. The water within the plumbing system is hotter than surface boiling, but it is stable because of the pressure exerted by the overlying water and rocks. The filling and heating process continues until the geyser is full/nearly full of water, and the geyser can erupt. A small geyser may take seconds to fill, whereas larger geysers may take days. There needs to be an adequate source of heat within the rocks lining the plumbing system in order for the eruption to last for more than a few seconds.

Because the water of the entire plumbing system has been heated to boiling, the rising steam bubbles no longer collapse near the surface. Instead, as more hot water enters the geyser at depth, more and larger steam bubbles form and rise toward the surface. Initially, the bubbles rise to the surface with no difficulties. However, as more and more steam bubbles rise, they encounter constrictions in the plumbing system. Geysers, unlike hot springs, have constrictions near the surface of their channel systems. Constrictions are blocks in the path to the surface, possibly by sinter or a winding fracture system. The pressure builds up until it forces some water out of the channel so that the steam bubbles can escape. The loss of water reduces the pressure of the residual water in the geyser, lowering the boiling temperature. This water that was already boiling, now boils more vigorously and forms more steam bubbles. The steam rapidly expands to over 1500 times its original liquid volume, and the reservoir empties itself catastrophically, causing a violent explosion and rapidly ejecting steam and water into the air. The eruption continues until the depletion of water or the temperature drops below boiling. Once an eruption ends, the entire process of reservoir filling, heating, and boiling will repeat periodically, leading to another eruption.

The two types of geysers are fountain (pool) geysers and columnar (cone) geysers. Fountain geysers erupt water in various directions through a pool. Columnar geysers are built up

formations of sinter that erupt water in a narrow stream, generally from a vent in the cone. Sinter deposits are formed by the precipitation of silica-rich waters during an eruption. A large sinter mound does not always mean an old thermal feature, but most sinter accumulation is only a minute fraction of an inch annually [Schreier, 1992]. Drilling and core samples from the Upper Geyser Basin revealed a sinter layer about 6 meters thick [Schreier, 1992], but sinter thicknesses and rates of silica deposition are highly variable.

A hot spring, warm spring or pool will form instead of a geyser if heat energy is released in a steady manner and water flows freely to the surface [Smith and Siegal, 2000]. Hot springs are similar to geysers, but unlike a geyser, the water is not trapped in a pressurized reservoir because their underground channels are large enough to allow rapid circulation of water. The convection currents maintain equilibrium by returning the cooler groundwater to the system as the rising hot water releases energy by evaporation or hot water runoff. If relatively little hot water flows through clays or other colored soils, chemicals in the water dissolve the clays, forming different colored mudpots [Smith and Siegal, 2000]. If steam is released without much hot water, a fumarole forms. These vents are commonly encrusted with dissolved mineral deposits from the hot water and steam supply [Smith and Siegal 2000].

The locations of these thermal features include flat-bottomed valleys between lava flows. The stream- and glacier-sediment covered valleys allow water to percolate in the ground, and the water becomes heated. Thermal features also occur along active faults inside and outside the caldera, at the bottom of slopes where groundwater pools after running off higher ground, and along the ring shaped fracture zone where the caldera floor is depressed [Smith and Siegal, 2000]. These are places where water can percolate easily underground.

Bacteria and algae are mainly responsible for the brightly colored runoff channels of hot springs and geysers (Figure 5a and Figure 6h). Different water temperatures permit different bacterial communities. The run-off channel from a hot spring is white or clear near its source. Only a few single-cell bacteria live in this boiling water, which is 93 °C at the average Yellowstone elevation of 2286 meters [Schreier, 1992]. As the water cools to 75 °C farther down stream, the first cyanobacterium (*Synechococcus lividus*), filamentous green nonsulfur bacterium (*Chloroflexus aurantiacus*), and others (*ChromatiunItepidum*) begin to colonize and form laminated bacterial mats [Schreier, 1992]. Only the first millimeter of a microbial mat actively grows; the top bacteria layer shades the bacteria below and new individuals grow upon the remains of the previous generation, thus forming a layered laminated mat [Schreier, 1992].

### **III. Lower Geyser Basin (LGB)**

LGB is the largest thermal area in Yellowstone (19.3 km<sup>2</sup>). It is geomorphically expressed as a flat plain covered with glacial sediments, large areas of siliceous sinter, and interspersed by lodgepole pine. Figure 3 shows the extent of siliceous sinter in the LGB from the AVIRIS remote sensing image. Rhyolite ridges surround the plain, forming steep escarpments in some sections. Glacial moraines border the ridges on the north and east sides, and extend into the basin. Geological evidence suggests that these moraines are the sites of pre-glacial hot springs [Marler, 1964]. Groups of hot springs are widely scattered over the entire basin, but most are found in the eastern portion of the LGB. Even though the Lower Geyser Basin has a smaller number of geysers than other geyser basins, it is much larger in terms of hot water discharge volume [Marler, 1964].

#### **IV. Midway Geyser Basin (MGB)**

MGB is located in a low, flat-lying area (Figure 3) that is topographically part of the Lower Geyser Basin, but separated by dense forests to the north and west [Bryan, 1995; Smith, 2000]. East of this basin, Mallard Lake Dome was uplifted, creating two faults that run from southeast to northwest on the dome summit. The faults fracture the rock, allowing rain and snowmelt to percolate downward and become heated. The brine then rises upward along fault fractures that supply hot water to Midway's hydrothermal features [Smith, 2000]. The hot springs extend along Firehole River for about 1.5 km, and then an additional 1.5 km along Rabbit Creek drainage. Springs are numerous along both drainages, but geysers are scarce. Notable springs include Grand Prismatic Spring, the largest and deepest spring in Yellowstone (113 m in diameter and 34 m deep), as well as the powerful Excelsior Geyser, known for its tremendous discharge of water [Marler, 1964].

#### **V. Upper Geyser Basin (UGB)**

UGB has an area of only 3.2 km<sup>2</sup>, yet contains nearly one-quarter of all the geysers in the world (Figure 3). It is part of the Firehole River Valley and is surrounded by cliffs on the west, northwest and east. The valley is drained by Firehole and Little Firehole Rivers, as well as Iron Spring Creek. Important geysers are located near the main rivers [Marler, 1964].

Small outcrops of the West Yellowstone rhyolite unit are located between Firehole River and Iron Spring Creek, but are mainly covered by glacial gravels and soil. In the southern section, glacial outwash, consisting largely of obsidian sand, covers the floor, but most of the basin is covered with siliceous sinter deposits from the hot springs [Marler, 1964].

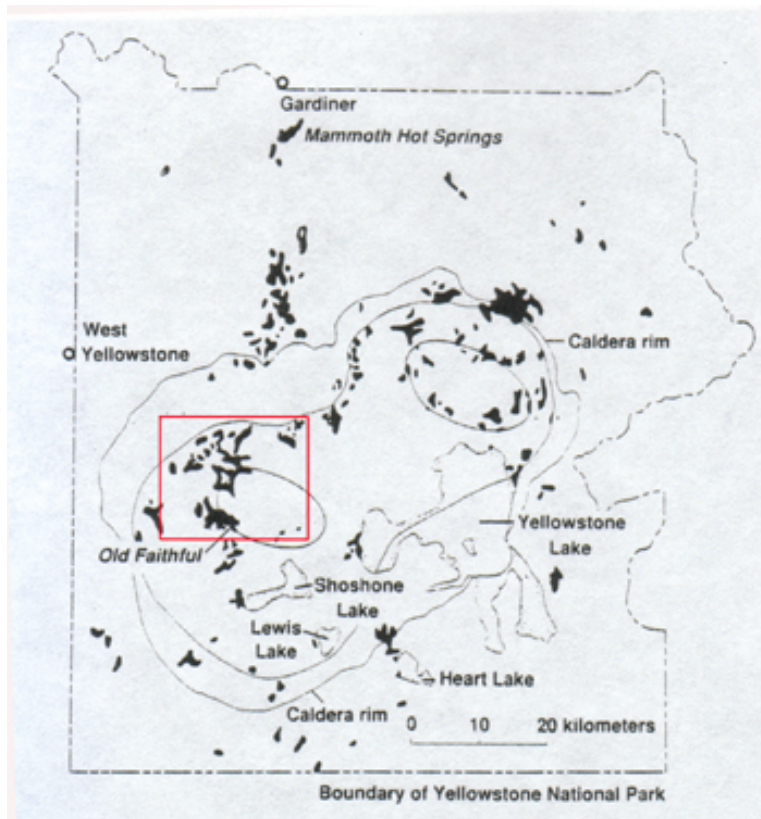


**Figure 2** Yellowstone location map showing active and fossil hydrothermal systems (Walter and DesMarais, 1993). Active and fossil springs are both outlined in black. The Yellowstone caldera rim and the two resurgent domes are shown. Red box shows the approximate location of the study area (seen in Figure 3).



**Figure 3** AVIRIS visible reflectance image of the LGB, MGB, and UGB of Yellowstone National Park with band 31 ( $0.666 \mu\text{m}$ ) in red, band 20 ( $0.557 \mu\text{m}$ ) in green, and band 12 ( $0.478 \mu\text{m}$ ) in blue. Pixel resolution is 20 m. Geyser basins are defined in white and show broad regions of siliceous sinter. White Dome (WD) ( $44^{\circ}32' 21.81''$ ,  $-110^{\circ}48' 10.36''$ ) and Firehole River are labeled for reference. Latitude/longitude coordinates are in UTM zone 12/ WGS84 datum.

## **Section 3: Methodology**

### **I. Field Site Selection and Description**

Field work was conducted in Yellowstone National Park from July 21 to August 2, 2001 under the park assigned permit number YELL-2001-SCI-0203. Springs were surveyed over a large area, and included several in each geyser basin. Specific springs mapped exhibited variations in size, types of deposits, and activity, i.e. active and near- to fully-extinct springs. These areas were selected in consultation with National Park Service personnel to target areas of primary geologic interest. The primary factors preventing full access to every site included safety and popularity. Certain sites could not be sampled because they are located on unstable thermal ground. In most cases, popular sites were also ruled out, because of the close proximity of tourists. Fourteen sites were ultimately surveyed. Table 1 provides a summary of each of the fourteen field sites. Six active sites (Sites 1, 4, 5, 9, 10, 13), five extinct sites (Sites 3, 7, 8, 12, 14), two near-extinct sites (Sites 2, 6), and one active and extinct site (Site 11) were selected. See Figures 4a-c for site locations within each basin. Active sites are defined as sites that have geyser activity and surficial water runoff, and/or hot springs with an abundant water supply, generally in close association with colored bacterial mats. Extinct sites are defined as sites with no geyser activity, dried-up hot springs, and/or lack of water in the area. Within these extinct sites, there is evidence of past geyser activity, indicated by a cone remnant and/or old sinter deposits. Near-extinct sites have little water, no active geysers, and perhaps a few small hot

springs. The active and extinct site was a large field site that was active in one area of the site and extinct in another area; dense vegetation separated the active from the extinct site.

### **A. Site 1, White Creek Group**

Site 1 is located at White Creek Group in the LGB (Figure 4a), studied on July 21, 2001. White Creek is a group of mild activity, with few areas of soft thermal ground. This renders it a safer area than some of the other field sites studied. The group of active springs that were studied is unnamed and is located near Octopus Spring (Figure 5a). It includes two springs/pools and two smaller springs. Old sinter is widespread and patches of grass are dispersed throughout. The primary deposits are fragmental sinters. These are the most common type of opaline sinter [Wohletz and Heiken, 1992]. It breaks easily into fragments where the deposits dry out and are exposed to weathering. Some of the fragmental debris remains in its original place, but some appeared to have been transported by wind and/or water. The grass is more widespread by the creek and across the creek. Thermal microbes are abundant in the runoff channels of some of the springs. One of the springs is located on a small hill, slightly higher than the other springs.

### **B. Site 2, Firehole Lake Group**

Site 2 is located at Firehole Lake Group in the LGB (Figure 4a), studied on July 22, 2001. The most outstanding feature of the area is the massive amounts of manganese oxide present in the boulders, rocky soil, and fine soil. Travertine is a rare occurrence in the LGB, but is present around Steady Geyser and the terraces of Firehole Lake. Travertine indicates the presence of increased amounts of CO<sub>2</sub> in the area [Bryan, 1995]. As the water is heated it reacts with carbonate rocks and liberates CO<sub>2</sub>. As the water reaches the surface it is cooled. The CO<sub>2</sub> escapes and the water becomes supersaturated with CaCO<sub>3</sub> and precipitates travertine. East of Firehole Lake, high standing cliffs are present on the north side, with MnO present in the soil [Bryan, 1995]. The study site is in a remote location about 45 m from Firehole Lake (Figure 5b).

Firehole Lake Group has many active geysers, but the field site is near-extinct, with little to no activity. Burned tree branches are randomly scattered throughout. The easternmost spring here is unnamed, small (~ 1m), and boiling with prominent green algae along its rim. Despite the algae, thermal microbes are not evident in the majority of the area. A few mudpots are present around the area. Another hot spring south of this one has relatively abundant sinter around it, and is bright white (but not as bright white as some of the other sinters studied). The majority of the site is covered with MnO soil mixed with fine sinter deposits.

### **C. Site 3, Myriad Group**

Site 3 is located at the Myriad Group in the Upper Geyser Basin (Figure 5c). Studied on July 22, 2001, this group is closed to public entry because it is extremely dangerous, having over 1000 vents in a relatively small area. The Ruin is a cone remnant of an extinct spring (Figure 5c). The Ruin is composed of predominantly dark sinter and also contains some older chalcedonic sinter, common within older deposits [Wohletz and Heiken, 1992]. Chalcedonic sinter is formed during late-stage solution and deposition. Chalcedony and quartz are deposited and earlier opal phases are at least partially recrystallized [Wohletz and Heiken, 1992]. It contains predominantly dark gray sinter with some white sinter formations, surrounded by grass. The grass is only a few centimeters tall and is abundant near the Ruin and the area surrounding the Ruin. Most of the grass is yellow-green or brown-green. Fresh green grass is not present, but further towards the main road, it is visible from the small parking lot near the Ruin. The active part of Myriad has little to no grass. A small cluster of about 20 pine trees are situated several meters away from the thermal activity of the springs. Between the Ruin and Many Spring Pond there is no thermal activity; only small meter-sized extinct geyserite patches are evident. Geyserite is a common opal deposit; a non-gem form of opal. The active part of Myriad is about 15 m west of the Ruin. At least 30 or more vents can be seen giving off small amounts of steam. The Ruin and many of

the active springs are on slightly higher ground (approximately a ten degree incline) relative to the surrounding area between Many Spring Pond and the Ruin. Although subtle, the smell of the hydrogen sulfide gas is noticeable during windy periods.

#### **D. Site 4, Fortress Geysers**

Site 4 is Fortress Geysers, located in River Group in the LGB (Figure 4a). The River Group is a highly dangerous area of the park. Extremely soft thermal ground is located in many areas and violent geysers and boiling pools are scattered throughout. Studied on July, 22, 2001, Fortress is an extremely active and regular geyser (Figure 5d). It has a large sinter cone, having a shape resembling a fortress. Orange- and brown-colored mats are indicative of the thermal microbes present in the watery deposits and runoff channels surrounding the cone. There are also several smaller pools and geysers surrounding the area. Vegetation is abundant and the ground is soft and thermally unstable. The sinter here is also known as geysersite, or opaline sinter. This type of sinter is most common on sinter cones as the sinter is deposited by the geyser. The boiling water contains a high silica content. After the water is ejected, it cools and evaporates quickly, precipitating silica as the water reaches the surface. The deposits are generally characterized by fine banding and botryoidal shapes. Figure 6a a close up view of the hard pink geysersite present in this area. The pink color in the sinter is caused by a trace of manganese oxide. If there were any more MnO present, the sinter would be black-colored, not pink.

#### **E. Site 5, Rabbit Creek Hot Springs**

Site 5 is Rabbit Creek Hot Springs, located in the MGB (Figure 4b), studied on July, 23, 2001. This is an extremely remote location with dense forest surrounding the entire area. Many burned trees are downed nearby and lead into this hilly area. The main geyser is hot and active (Figure 5e). A large extinct thermally altered field surrounds this area, and is interspersed with some dead yellow grass. Most of the deposits are made of silica cement and fine fragmental

sinter. Silica cement is an intermediate stage between clastic sediments and sinter deposits. This group is on Rabbit Creek, therefore sinter-cemented alluvial gravels readily form. Orange- and brown-colored mats indicate abundant thermal microbes in the streams of many of the springs.

#### **F. Site 6, Morning Mist Springs**

Site 6 is Morning Mist Springs, located in the Lower Geysier Basin (Figure 4a), studied on July 25, 2001. This is a short hike from the main road (Grand Loop Road). There are patches of soft thermally altered ground throughout the area (Figure 5f). Dozens of small pools are clustered near each other. There is no geyser activity nearby, only quiet pools or extinct springs. Lodgepole pines can be seen from this area, although they are not present in the immediate area. Thermal microbes are only seen near the rims of some of the small pools. The active deposits have fragmental and finely powdered sinter. The extinct deposits are harder and more brittle, exhibiting knobbier textures and polygonal-like fracturing. Figure 6b shows a close up view of the extinct sinter exhibiting large amounts of fracturing.

#### **G. Site 7, Fountain Flats**

Site 7 is Fountain Flats in the LGB (Figure 4a), studied on July 25, 2001. The area has many small patches of geyselite, the remnants of extinct springs. There is a small stream that cuts through a large portion of the area. There are also some mudpots and pools, but no active geysers. Vegetation covers most of the area, except the extinct patches (Figure 5g). Figure 6c shows a close up view of the finely powdered fragmental extinct sinter. There are also knobby sinter textures closer to the runoff channels of the pools. The knobby textures are a darker color and generally have vegetation growing on them. Thermal microbes are essentially absent throughout the area.

#### **H. Site 8, Extinct in Firehole**

Site 8 is an extinct region (29.6m by 10.6 m) in Firehole Lake Group in the LGB (Figure 4a), studied on July 26, 2001. This is a relatively large extinct field a few meters from Firehole Lake Drive (Figure 5h). The field itself is practically devoid of vegetation although the immediate surrounding region is abundant with fresh green grass. No thermal microbes are present. The deposit is a hard, brittle silica cement that is highly fractured.

#### **I. Site 9, Sunset Lake**

Site 9 is the Sunset Lake area of Black Sand Basin in the UGB (Figure 4c), studied on July 26, 2001. High rhyolite cliffs surround this low-lying basin area. The cliffs are mostly grass covered and support numerous trees, most of which were burned from previous fires. Rainbow Pool is the largest and most prominent feature (Figure 5i). A tremendous amount of steam rises from some of the springs, especially from Rainbow Pool. The field site is a large geyserite field nearby Sunset Pool, bordered by a stream on one side. Sinter deposits are abundant and darker sinter is less abundant. Close to the pool, abundant thermal microbes are visible. The sinter deposits are mostly fragmented, finely powdered sinter. Figure 6d shows a close up view of the hard sinter cement present in the area. Figure 6e shows a close up view of the dry brittle fragmental sinter that borders Figure 6d.

#### **J. Site 10, Sapphire Pool**

Site 10 is located near the runoff of Sapphire Pool in Biscuit Basin in the UGB (Figure 4c). It was studied on July 26, 2001. This basin, north of Black Sand Basin, also displays rhyolite cliffs to the east. Firehole River borders it on its west. Numerous obsidian rhyolite boulders are present near the river. The area is heavily vegetated; there is plentiful grass but not many trees. Steam is abundant above Sapphire Pool. Sinter deposits are darker in color than in Black Sand, implying more obsidian content here. Rhyolite cliffs are mostly covered with vegetation, and

there are many burned trees. The study area by Sapphire Pool is near burned lodgepole pines with bobbysox (Figure 5j). Bobbysox are white silica deposits that saturate the base of tree trunks. Types of sinter at this site include sinter needles (Figure 6f), finely powdered fragmental sinter, and sinter cement. Also common at this site, and indigenous to Biscuit Basin, are the delicate and knobby biscuit-like formations (Figure 6g) that give the basin its name.

#### **K. Site 11, Mallard Lake**

Site 11 is the Mallard Lake Area (also known as Pipeline Meadows) in the UGB (Figure 4c). It was studied on July 27, 2001. East of Old Faithful, this densely vegetated area is bordered by Firehole River on one side. There are many small, randomly spaced mudpots. Bend Cone is a pair of two geyserte cones, and is the highest standing and most prominent feature in the area. There are two major sinter fields in this area; the Bend Cone field and the surrounding Midas Spring field (Figure 5k). The majority of sinter is bright white. The sinter is a mix of finely powdered, fractured sinter further from the active springs and knobby sinter throughout the area. Close to the rim of Bend Cone, smooth opaline sinter deposits (wet geyserte) are commonly associated with orange mats (Figure 6h). Visible microbes are present surrounding the rims of Bend Cone. Midas Spring is known for its golden-colored sinter deposits.

#### **L. Site 12, Iris Group**

Site 12 is the Iris Group in the MGB (Figure 4b), which is closed to the public. It was studied on July 28, 2001. It is an extremely large, extinct, well-preserved sinter field with little vegetation (Figure 5l). A couple of active geysers are present as well, but these approximately 60 m from the large extinct field. The area is just south of Grand Prismatic Spring. There are a wide variety of sinter deposits, including sinter needles and fractured sinter. The vegetated areas are growing on darker sinters with a knobbier texture.

### **M. Site 13, White Dome**

Site 13 is White Dome Geyser in the LGB (Figure 4a), studied on July 28, 2001. White Dome is a prominent cone geyser with many runoff channels branching away from the dome (Figure 5m). White Dome consists of a younger cone geyser sitting on top of an older cone formation. The road, Firehole Lake Drive, cuts into one side of the surrounding area. However, the other side of the surrounding dome area is preserved. On this side, there is soft thermal ground with abundant vegetation surrounding it. The runoff channels on the north side extend for many meters, although they are quite narrow (less than a meter in width). The older domes are visible and are underneath the newer domes. Eruptions are rather frequent and irregular, but short. Intervals between eruptions are not more than about 4 hours, but eruptions only last about 2 minutes [Rocco Paperiello, personal communication]. Black algae and brown bacteria are present in the runoff channels located at the eastern portion of the dome (facing the road and the boardwalk). A wide variety of different sinter types, colors, and textures indicate the dome underwent dramatic changes over the years. Sinter deposits on the cone include fractured sinter, banded opaline sinter, chalcedonic sinter, and opaline sinter. The geyselite, or banded opaline sinter is similar to the sinter deposits observed at Site 4. Opaline sinter is formed as opal is deposited by percolating water. Older sinter deposits decrease in porosity as they are buried by younger deposits; this process locally produces glassy opal. At the base of the cone, finely powdered fractured sinter dominates.

### **N. Site 14, Fracture Group**

Site 14 is the Fracture Group in Pine Springs in the UGB (Figure 4c), studied on July 29, 2001. Pine Springs is about 1 km from Black Sand Basin. This site is located on an elevated plateau overlooking Black Sand Basin. The Fracture group has a large old and eroded sinter platform remnant, its most recognizable feature (Figure 5n). This mound displays banding,

characteristic of banded opaline sinter. A close up view of this banding is shown in Figure 6i. Chalcedonic sinter deposits are also on the cone. This type of sinter is common within older deposits. This area is devoid of hot springs; therefore water is not present. Many of the thermal features are represented by fractures, craters, or cracks in the rock with hot steam vents. The numerous fractures are all approximately the same temperature and are all about meter-sized or less.

## **II. Site Surveys**

Each field site was analyzed using similar non-invasive methods. These included land cover analysis, photographs, GPS data collection, radiometric analyses, and field spectroscopy. Small amounts of soil samples, as well as hand samples of rocks and minerals were collected at some sites.

Field spectra were acquired using an Analytical Spectral Devices (ASD) FieldSpec Pro that collected information from visible to near infrared wavelengths (350 to 1100 nm). The sampling interval is 1.4 nm over the entire wavelength range. These data were collected in order to map small-scale spectral variations produced as well as for a comparison to the AVIRIS and ASTER VNIR data. The FieldSpec Pro is a portable, silicon detector array-based spectrometer consisting of a spectrometer unit and 1 m long fiber optic cable inserted into a foreoptic. The spectrometer has a rapid response time, taking spectral readings in a fraction of a second. Spectral data is viewed in real time through an attached portable laptop computer. The dark current of the instrument is determined, which is the signal recorded where no light falls on the detector. Before beginning data collection, appropriate integration time is set to avoid detector saturation. The instrument automatically does this if it is optimized on the brightest target it

sees, a spectralon plate. The spectralon calibration plate is a perfectly diffuse reflecting material. The plate was used as a reflectance calibration before collecting each spectrum. This is an important step in acquiring accurate spectra, especially in variable atmospheric conditions. The spectrometer integrates several spectral scans to produce one output spectrum. The default is 10 scans per screen update. After collected, spectra can be saved as reflectance files to the hard drive of the laptop.

The GPS unit is a Trimble Pro XRS dGPS receiver with a TSC1 assay surveyor data logger. The purpose of the GPS unit was to obtain the map coordinates of the main roads and tourist boardwalks in the park and to mark specific locations of spectral and temperature data collection points at each site.

### **III. ASTER Data Acquisition and Processing**

Two daytime ASTER level 1B (L1B) scenes were acquired on November 4, 2000, covering all three geyser basins of Yellowstone National Park (Figure 7a and b). The radiometrically and geometrically corrected scenes were initially georectified from metadata information (Table 2). After data validation studies were conducted in the field, GPS data showed that the initial georectification was displaced by approximately 45 to 60 m for the VNIR and SWIR regions. The second stage of georectification involved re-registration of the ASTER data using the GPS vector data, resulting in <1 m error between the two data sets (Table 3). Because the TIR region has a much larger pixel size, initial georectification was deemed sufficient. The ASTER level 2 (L2) products for VNIR and SWIR (radiance at ground and surface reflectance), and the TIR L2 products (radiance at ground, kinetic temperature, and emissivity) were obtained for the same scenes. The Earth Observing System Data Gateway

Distributed Active Archive Center (EDG DAAC) has an online search for all ASTER scenes. The L1B and L2 data were ordered by submitting a data acquisition request (DAR) via the DAR Tool [Abrams, 2000]. The higher L2 products are under a provisional release status and have not been fully validated by the ASTER team at the time of the analyses. However, extensive work by Thome et al. (1998) and Ramsey and Dehn (2002) show that the data are well calibrated and the L2 processing algorithms appear to be working correctly.

#### **IV. AVIRIS Data Acquisition and Processing**

AVIRIS data were acquired from the NASA Jet Propulsion Laboratory (JPL) through a proposal for free data for graduate students. These data are for the Lower, Midway, and Upper Geyser Basins of Yellowstone National Park. Three geometrically and radiance calibrated scenes were used from one flight line acquired on July 14, 1997 (Figure 3). In order to convert AVIRIS data from radiance to reflectance, the data were corrected for the influence of several variables, including solar irradiance, atmospheric gas absorptions, and path radiance. These corrections were done using the Atmospheric Correction Now (ACORN) software program, which uses radiative transfer modeling [<http://www.aigllc.com/acorn/intro.asp>]. Nash and Johnson (2002) determined that ACORN gave the closest match to laboratory spectra, in comparison to the Atmospheric Removal Program (ATREM) and the internal average reflectance (IAR) method; ACORN was recommended for use in detailed mineralogical mapping. Because AVIRIS is an airborne sensor, the same process used to georectify the ASTER images could not be used. Rather, an RST warp using nearest neighbor was done using Environment for the Visualization of Images (ENVI) v.3.5 software.

All ASTER and AVIRIS data processing was performed on a Solaris Unix UltraSparc 10 workstation. The software used for the image processing was ENVI v3.5. Images were resized and final adjustments were made using Corel Draw 8.0 and Adobe Photoshop version 5.5. The GPS points collected were loaded into the GPS Pathfinder Office software program. Non-real time differential corrections were done using base station points at Idaho Falls, Idaho. The corrected dGPS data was loaded into ENVI as a vector (.evf) file.

Site No.	Name	Geyser Basin	Latitude (N) UTM (meters) DMS	Longitude (W) UTM (meters) DMS	Activity	Notes
1	White Creek Group	LGB	4931116.56 44°31'59.51"	516121.02 -110°47'49.56"	Active	Small pools/ geysers; some extinct sinter deposits nearby
2	Firehole Lake Group	LGB	4932320.30 44°32'38.41"	517459.31 -110°46'48.77"	Near extinct/ extinct	Small pools filled with algae, fumaroles; areas of extinct sinter
3	The Ruin	UGB	4922805.00 44°27'30.34"	513302.04 -110°49'58.05"	Extinct spring	Near Myriad Group – highly active/dangerous
4	Fortress Geyser	LGB	4933686.22 44°33'22.99"	513325.51 -110°49'55.98"	Active geyser	Large geyser with many sinter deposits
5	Rabbit Creek Hot Springs	MGB	4929557.73 44°31'9.06"	515110.19 -110°48'35.52"	Active geyser	Small geyser/fumaroles surrounded by large extinct sinter field; surrounded by deep forest
6	Morning Mist	LGB	4935403.33 44°34'16.79"	515239.04 -110°48'34.40"	Near extinct	Many small pools and extinct large sinter areas
7	Fountain Flats	LGB	4934860.13 44°33'59.24"	514463.98 -110°49'4.26"	Extinct/ Near extinct	Extinct sinter areas and tiny nearly dried up pools/ mudpots surrounded by much vegetation
8	Extinct unnamed	LGB	4932182.75 44°32'34.02"	516606.56 -110°47'27.43"	Extinct	Dry cracked sinter surrounded by vegetation
9	Sunset Lake	UGB	4923289.66 44°27'46.16"	511547.74 -110°51'17.40"	Active	Large geothermal pool surrounded by extinct deposits
10	Sapphire Pool	UGB	4925719.40 44°29'4.91"	511477.94 -110°51'20.37"	Active	Large geothermal pool surrounded by extinct deposits
11	Mallard Lake Group	UGB	4923097.83 44°27'39.78"	514063.34 -110°49'23.58"	Active/ Extinct	Small active springs interspersed with extinct deposits; Heavily vegetated; scattered mudpots
12	Iris Group	MGB	4929700.49 44°31'13.81"	513456.55 -110°49'50.42"	Mostly extinct	Large extinct field with two moderately sized pools/active geyser nearby
13	White Dome	LGB	4931803.73 44°32' 21.81"	515660.31 -110°48'10.36"	Active	Large highly developed sinter cone
14	Fracture Group	LGB	4923646.53 44°27'57.70"	511985.32 -110°50'57.57"	Extinct spring/ steam vents	Small steam vents surrounded by extinct deposits

**Table 1** Description of Field Sites.

<b>ASTER scene</b>	<b>Latitude (upper left corner)</b>	<b>Longitude (upper left corner)</b>	<b>Scene Orientation angle</b>	<b>UTM Zone</b>	<b>Datum</b>
LGB	45.082555	-110.878407	-11.161188	12	WGS-84
UGB	44.555545	-111.061955	-11.188743	12	WGS-84

**Table 2** Initial stage of georectification: Metadata information.

<b>ASTER scene</b>	<b>Latitude (upper left corner)</b>	<b>Longitude (upper left corner)</b>	<b>Scene Orientation angle</b>	<b>UTM Zone</b>	<b>Datum</b>
LGB VNIR	44.516964	-110.889003	-11.161188	12	WGS-84
LGB SWIR	45.082750	-110.878017	-11.161188	12	WGS-84
LGB TIR	45.083350	-110.878186	-11.161188	12	WGS-84
UGB VNIR	44.556075	-111.060817	-11.188743	12	WGS-84
UGB SWIR	44.555758	-111.061175	-11.188743	12	WGS-84
UGB TIR	44.556339	-111.061736	-11.188743	12	WGS-84

**Table 3** Second stage of georectification: Using GPS.

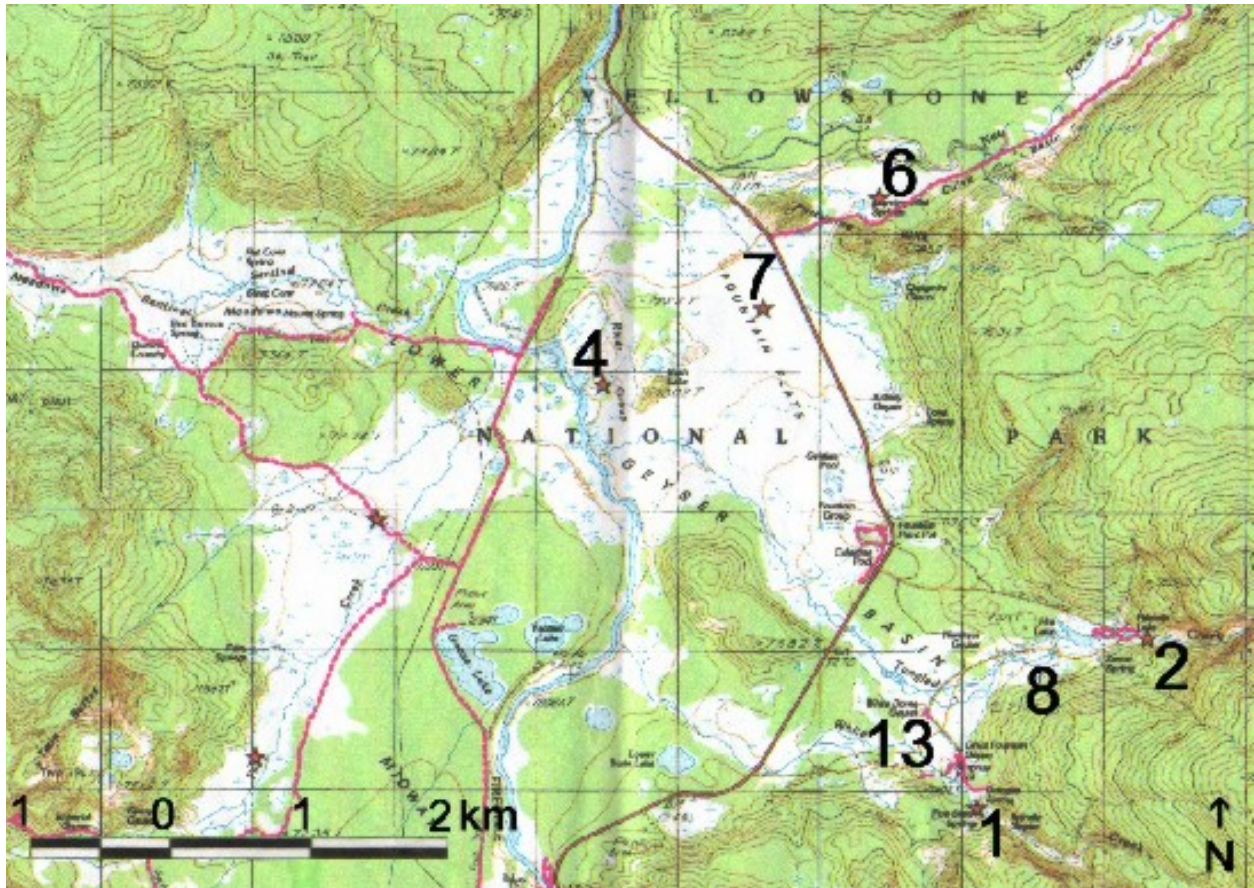


**Figure 4a** Location map of the LGB with numbered field sites, showing the seven field sites in the basin (Site 1, 2, 4, 6, 7, 8, 13) (Spatial Analysis Center at YNP).

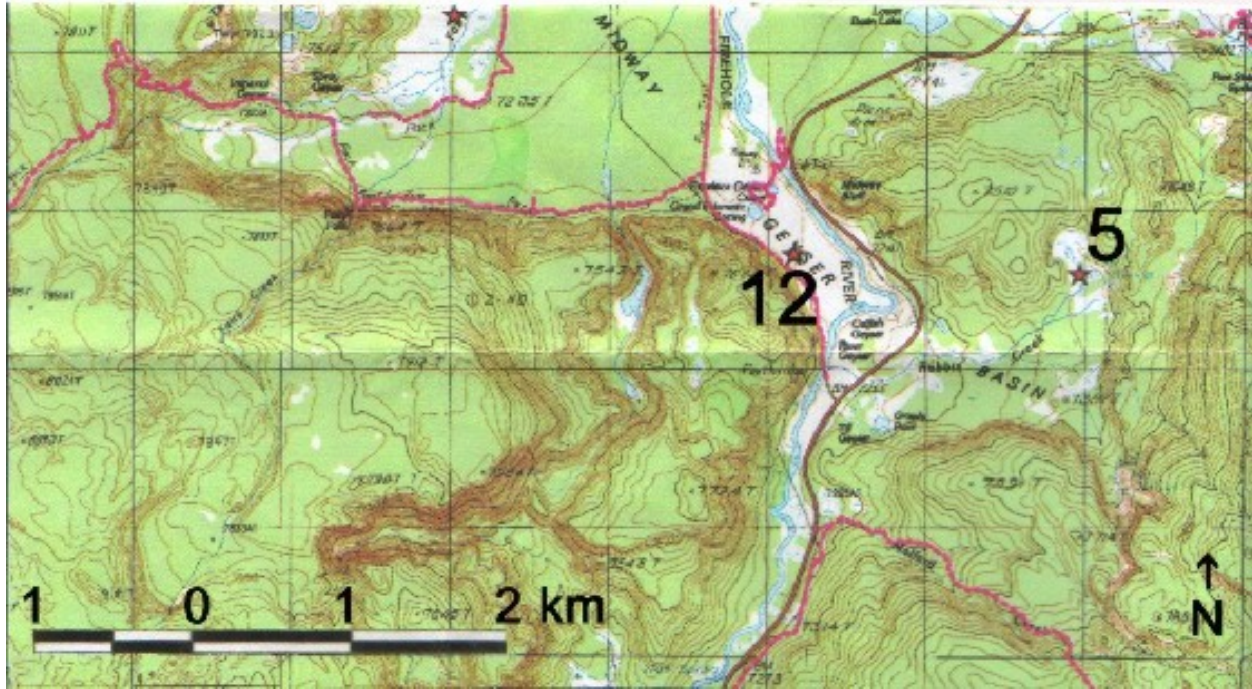


**Figure 4b** Location map of the MGB with numbered field sites, showing the two field sites in the basin (Site 5, 12) (Spatial Analysis Center at YNP).

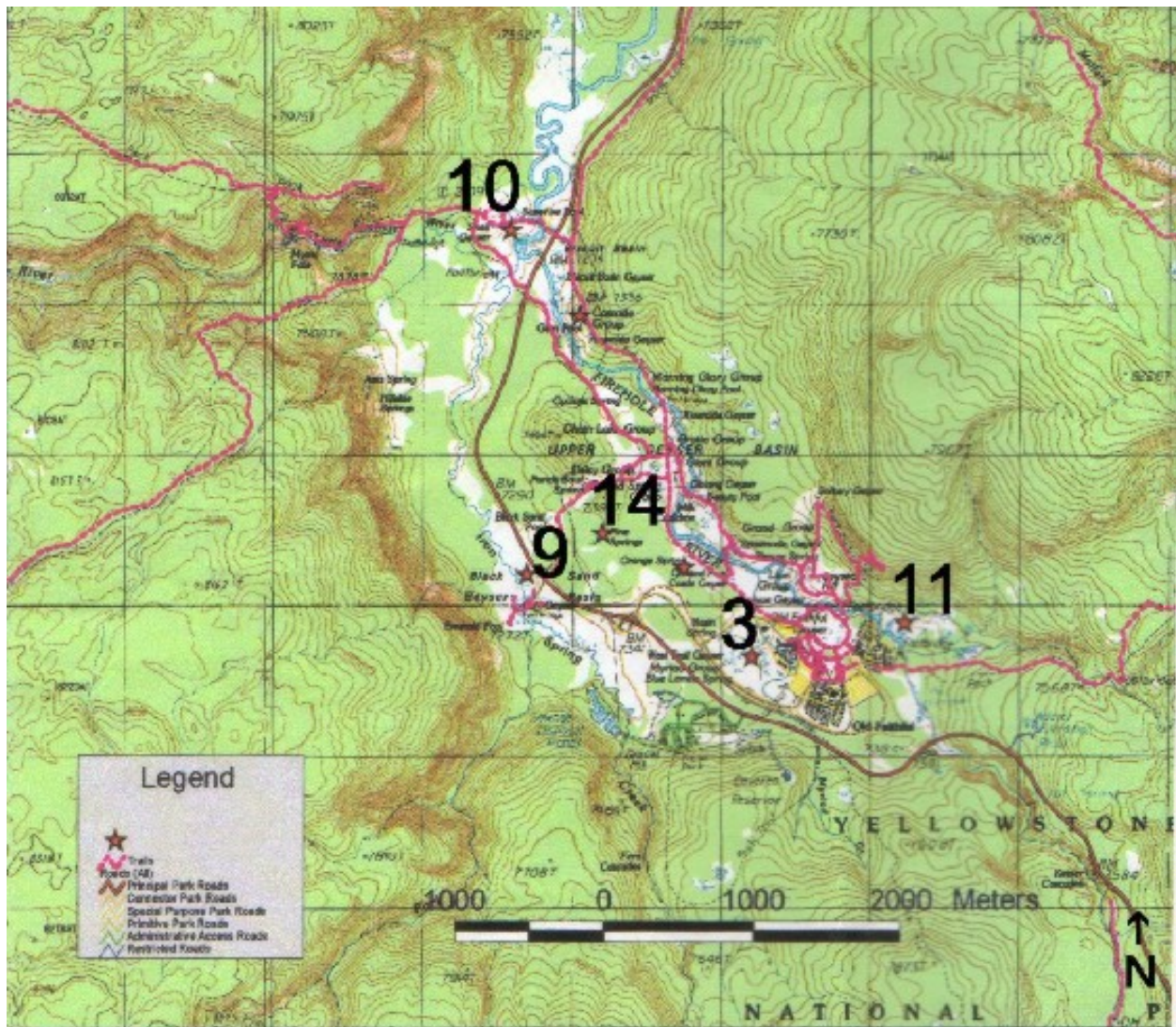


**Figure 4c** Location map of the UGB with numbered field sites, showing the five field sites in the basin (Site 3, 9, 10, 11, 14) (Spatial Analysis Center at YNP).



**Figure 5a** Field photograph of Site 1 (White Creek Group). This is an active area containing several pools and geysers. A small pool is shown above. In the runoff channel, orange and green-brown thermal microbes dominate. Siliceous sinter deposits surround the rim of the spring (*see text for complete descriptions*).



**Figure 5b** Field photograph of Site 2 (Firehole Lake Group). This is a near-extinct to extinct thermal area. Black manganese oxide is contained in the soil, as seen above (*see text for complete descriptions*).



**Figure 5c** Field photograph of Site 3 (The Ruin). This is a large remnant of an extinct spring deposit located in a highly active group(Myriad Group) (*see text for complete descriptions*).



**Figure 5d** Field photograph of Site 4 (Fortress Geyser). This is an extremely active geyser having a siliceous sinter cone formation. Orange thermal microbes dominate in the watery runoff channels (*see text for complete descriptions*).



**Figure 5e** Field photograph of Site 5 (Rabbit Creek Hot Springs). Located in a remote area, this geyser is active and siliceous sinter can be seen around the vent and orange thermal microbes can be seen to the far left of the image (*see text for complete descriptions*).



**Figure 5f** Field photograph of Site 6 (Morning Mist Springs). This is a near-extinct area showing a large extinct hot spring field with scattered patches of vegetation. Lodgepole pines are seen in the background (*see text for complete descriptions*).



**Figure 5g** Field photograph of Site 7 (Fountain Flats). This is a large extinct sinter field with no thermal microbes and some vegetation cover (*see text for complete descriptions*).



**Figure 5h** Field photograph of Site 8 (Extinct in Firehole Lake Group). This is an extinct desiccated hot spring field with dense vegetation surrounding the perimeter. Fractures can be seen in the sinter (*see text for complete descriptions*).



**Figure 5i** Field photograph of Site 9 (Sunset Lake). This is a large hot spring with various colored thermal microbes surrounding the rim. Siliceous sinter deposits are located in the foreground (*see text for complete descriptions*).



**Figure 5j** Field photograph of Site 10 (Sapphire Pool). This is an active site with the large pool to the left of the image. A variety of sinter deposits and textures can be seen here. Bobbysox (silica-saturated) tree trunks are seen in the background to the right of the image (*see text for complete descriptions*).



**Figure 5k** Field photograph of Site 11 (Mallard Lake Group). This is a large site with some areas that are active, and some areas that are extinct. The active Bend Cone geyser can be seen in the background. Vegetation separates some of the extinct deposits that are located in the foreground of this image (*see text for complete descriptions*).



**Figure 5I** Field photograph of Site 12 (Iris Group). This is a large extinct thermal field with broad siliceous sinter deposits (*see text for complete descriptions*).



**Figure 5m** Field photograph of Site 13 (White Dome). This is an active geyser with a large siliceous sinter cone (*see text for complete descriptions*).



**Figure 5n** Field photograph of Site 14 (Fracture Group). This is an extinct remnant of a thermal spring. All that remains surrounding this deposit are small patches of siliceous sinter and several steam vents (*see text for complete descriptions*).



**Figure 6a** Close up view of hard pink geysers at Site 4.



**Figure 6b** Close up view of fractured sinter at Site 6.



**Figure 6c** Close up view of finely powdered sinter at Site 7.



**Figure 6d** Close up view of hard sinter cement at Site 9.



**Figure 6e** Close up view of dry, brittle fragmental sinter at Site 9.



**Figure 6f** Close up view of sinter needles at Site 10.



**Figure 6g** Knobby biscuit-like sinter formations at Site 10.



**Figure 6h** Wet opaline geysers + mat at Site 11.



**Figure 6i** Banded opaline and chalcedonic sinter from Site 14.

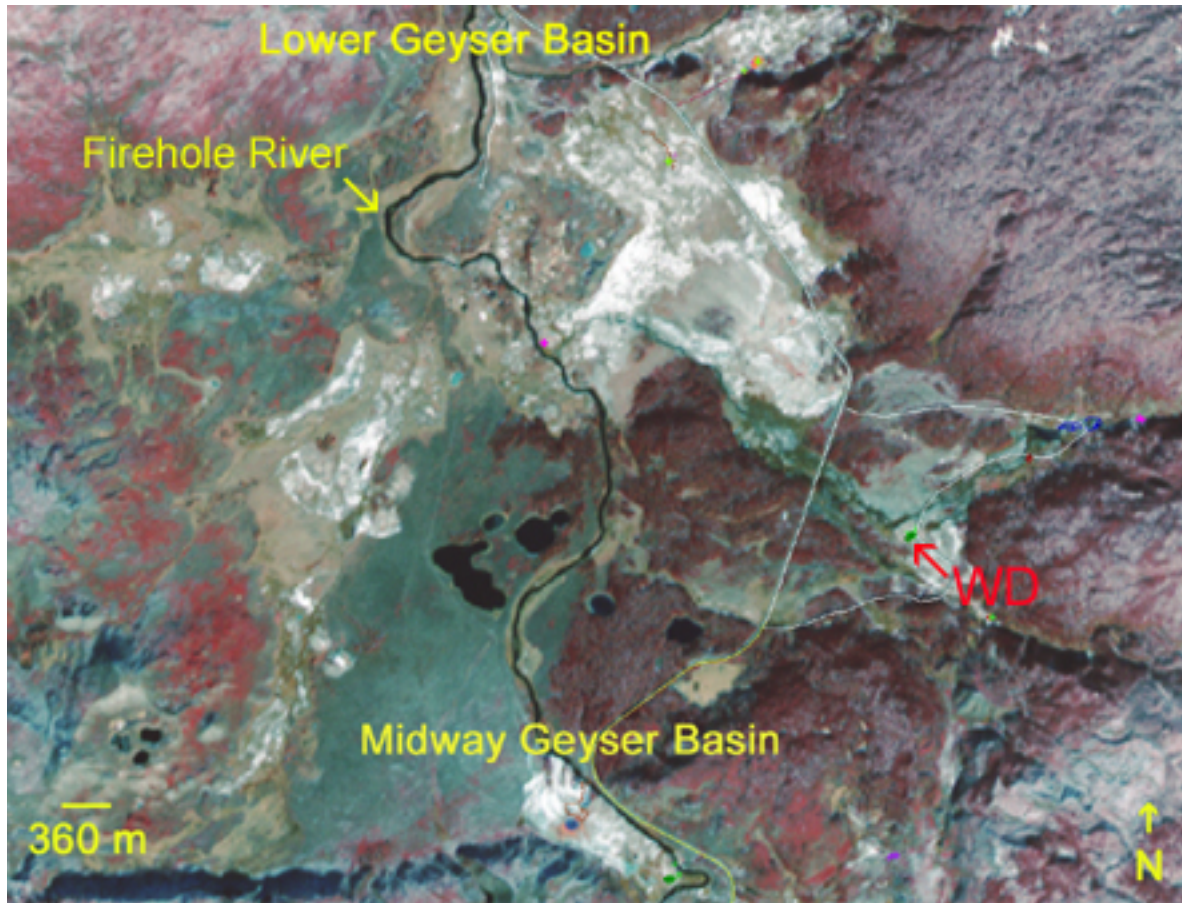


**Figure 7a** ASTER VNIR image of LGB and MGB (15m/pixel resolution) with GPS overlay. Geyser basins are defined in white and show broad regions of siliceous sinter. White Dome (WD) ( $44^{\circ}32' 21.81''$ ,  $-110^{\circ}48' 10.36''$ ) and Firehole River are labeled for reference. Latitude/longitude coordinates are in UTM zone 12/ WGS84 datum.

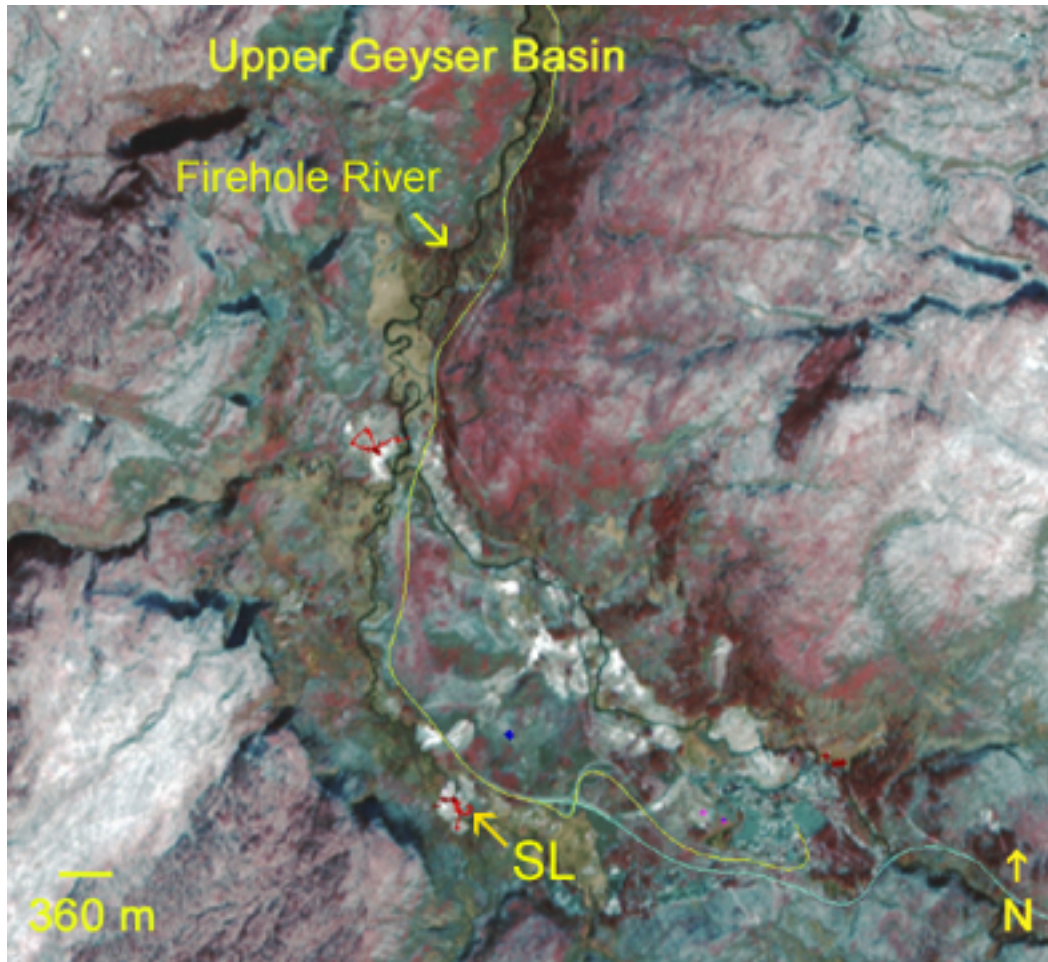


**Figure 7b** ASTER VNIR image of UGB (15m/pixel resolution) with GPS overlay. Geyser basins are defined in white and show broad regions of siliceous sinter. Sunset Lake (SL) ( $44^{\circ}27' 46.16''$ ,  $-110^{\circ}51' 17.40''$ ) and Firehole River are labeled for reference. Latitude/longitude coordinates are in UTM zone 12/ WGS84 datum.

## **Section 4: Results**

### **I. Reflectance**

#### **A. Field-Based VNIR Reflectance Spectra**

During field surveys, reflectance spectra of selected ground cover types were measured for active, near-extinct, and extinct springs. The type of spectra acquired was based upon an on-site determination of the most common ground cover types at each field area. At each site, spectra for the various types of wet and/or dry sinter deposits and/or other mineral deposits, vegetation, and bacterial mats were generally collected. Each field spectrum represents a ground area of 0.3 m. The number of field spectra acquired and examined totaled 156. Each spectrum can be seen in Appendix A. In this study, a “typical spectra” refers to spectra collected at a single field site representing the characteristics of other field sites exhibiting similar thermal activity.

Typical field spectra for an active site (Site 1, White Creek Group) are shown in Figure 8a. This particular unnamed group contains two pools and two smaller active microbial hot springs located near Octopus Spring. Hot springs bacteria and algae have unique spectra compared to vegetation. Spectra 002 and 005 display the characteristic shape of *Synechococcus lividus*, a common hot springs bacteria that creates a dark-green mat in the springs [Brock, 1994]; the spectra is similar to the bacterial spectral signature identified by Kokaly et al, (1998). The chlorophyll a absorption at 680 nm is narrow and the water absorption at 970 nm is strong. Red edge spectra at 765 nm and absorptions at 798 and 874 nm are seen. A minor absorption occurs at 620 nm that may reflect organics from the hyperthermophiles. The strength of the water absorption is due to a thin layer of hot water running over the bacterial surface [Kokaly, 1998].

In these active areas, the mineral signature is weak due to the overprinting of the water and bacterial cover [Kokaly, 1998]. A slight iron oxide reflectance minima, caused by the charge transfer effect, was observed in some of the field spectra around 950 nm. A reflectance increase was locally observed at around 550 nm, caused by iron oxide electronic transitions.

Typical spectra for an extinct site (Site 12, Iris Group) are shown in Figure 8b. This site is a large extinct sinter field interspersed with some vegetation. Spectrum 00e is a vegetation spectrum, identified by its characteristic high reflectance due to chlorophyll in the near-infrared spectral region. The extinct sinter is siliceous (Spectra 00a-00d) has a flat, featureless spectra in the VNIR. Reflectance rises from the visible to the infrared with the steepest slopes at less than 600 nm. Maximum reflectance occurs around 1000 nm. The active sites with visible microbes and iron oxide display a reflectance peak at about 560 nm. The prominence of this feature is variable, but in most cases was evident. In the extinct sites, this peak was commonly subtle or absent. Bound water absorptions are absent.

## **B. ASTER and AVIRIS VNIR Reflectance Spectra**

The wavelength studied for the VNIR spectra ranges from 0.55 – 0.82 microns. The ASTER and AVIRIS VNIR reflectance spectra for each field site can be seen in Appendix B. The field sites ranged in size from 1-10 pixels on the ASTER and AVIRIS images, where one pixel represents 15 m and 20 m, respectively.

ASTER VNIR spectra of an active site (Site 9, Sunset Lake) and an extinct site (Site 7, Fountain Flats) are shown in Figure 9a and 9b, respectively. Site 9 is part of the Biscuit Basin, which is surrounded by rhyolite cliffs. The cliffs are mostly grass covered and support numerous trees, most of which were burned during the large fires of 1988 [Franke, 2000]. The site is a large geyserite field near Sunset Lake, bordered by a stream on one side. Sinter deposits are abundant, darker sinter is less abundant. Site 7 has a small stream that cuts through a large

portion of the area. There are also some mudpots and pools, but no active geysers. Vegetation covers most of the area, except over the extinct patches of sinter.

ASTER and AVIRIS VNIR spectra for the active and extinct sites are dominated by vegetation. ASTER band 3 is located in the near-infrared and shows a large reflectance increase (red-edge). Band 2 is located in the visible red and chlorophyll absorption dominates. Band 1 is located in the visible green; here, a chlorophyll reflectance peak is present in some of the spectra. All of the active sites, with one exception, exhibited the band 1 reflectance peak. More than half of the extinct sites lacked the band 1 peak. Other differences between active sinter and extinct springs could not be distinguished. Probable reasons for this include the broad band passes of ASTER in conjunction with the large 15 m pixel size and the large 20 m pixel size of AVIRIS. The spectra indicate sub-pixel mixing, as the spectra do not resemble dry or green grass. Reflectance in the visible red and green is higher for these spectra than grass spectra.

### **C. ASTER and AVIRIS SWIR Reflectance**

The wavelength studied for the SWIR spectra ranges from 1.65 – 2.4 microns. The ASTER and AVIRIS SWIR reflectance spectra for each field site can be seen in Appendix C. The field sites ranged in size from 1-9 pixels on the ASTER and AVIRIS images, where one pixel represents 30 m and 20 m, respectively.

AVIRIS SWIR spectra of an active site (Site 13, White Dome) are shown in Figure 10a. White Dome (Figure 5m) is a prominent cone geyser with several runoff channels branching from the dome. A wide variety of different sinter types, colors, and textures indicate the dome underwent several changes over time. The older domes are visible and are located underneath the newer domes. Eruptions from this geyser are frequent, short and irregular. Black algae and brown bacteria are present in the runoff channels located on the eastern portion of the dome. The

2.25  $\mu\text{m}$  absorption feature for siliceous sinter [Kruse, 1999] is present in the AVIRIS spectra, although it is not particularly deep.

AVIRIS SWIR spectra of an extinct field (Site 12, Iris Group) are shown in Figure 11a. This sinter field occupies much of the basin; therefore it is easily detected in the ASTER (30 m pixel) and AVIRIS (20 m pixel) SWIR data. Based on the absorption feature near 2.25  $\mu\text{m}$  in the AVIRIS spectra, distribution of the siliceous sinter is visible [Kruse, 1999]. For most of the extinct sites examined, the 2.25  $\mu\text{m}$  absorption feature is deeper and more pronounced than the active spectra. At 2.2  $\mu\text{m}$ , there are minor absorptions, indicating the presence of small amounts of clay minerals, i.e. montmorillonite and kaolinite. Near 2.4  $\mu\text{m}$ , the extinct site spectra have a small reflectance peak that is not observed in the active site spectra. The 2.4  $\mu\text{m}$  reflectance peak is absent from the active sites because the sinter is wet, and the water may be suppressing (or flattening) the subtle reflectance peak [Kruse, 1999].

The ASTER SWIR spectra of both the active and extinct sites are shown in Figure 10b and 11b, respectively. The siliceous sinter absorption feature at 2.25  $\mu\text{m}$  cannot be easily identified because of the broader spectral band passes. The spectra most resemble a mix of dry and green vegetation, with a small reflectance peak at 2.2  $\mu\text{m}$  and absorption at around 2.37  $\mu\text{m}$ , but significant spectral mixing occurs in pixel sizes of 30 m.

Overall, spectra for the Lower, Midway, and Upper Geyser Basins indicate broad regions of siliceous sinter combined with small amounts of clays (i.e. kaolinite and montmorillonite) and other minerals (i.e. iron oxide) in some areas. The dominance of the siliceous sinter in these basins indicates the presence of neutral to alkaline waters. White et al. (1988) proposed that montmorillonite and siliceous-sinter are formed from neutral pH waters high in chlorine and quartz [Kokaly, 1998], such as those waters in the Lower, Midway, and Upper Geyser Basins.

More acidic hydrothermal systems, such as Norris Geyser Basin, contain higher amounts of clays and sulfate minerals associated with more acidic waters [Clark, 1993].

## **II. ASTER and AVIRIS Color Composites and Band Ratios**

Al-OH and Mg-OH rotational effects associated with clays and other hydroxylated minerals result in absorption in ASTER band 6 and AVIRIS band 195 [Sabins, 1999]. Hydroxyl absorption bands are caused by overtone and combination bands of primary OH<sup>-</sup> molecular vibration bands located at wavelengths longer than 2.5 microns [Vincent, 1997]. Overtone bands occur at wavelengths where the frequency of a primary absorption band is doubled, tripled, etc., and combination bands occur where the frequencies of two primary bands are added [Vincent, 1997]. The locations of the OH<sup>-</sup> absorption bands depend on the position of the hydroxyl ion in the crystal lattice [Vincent, 1997].

The ASTER SWIR bands were spatially resampled from 30m to 15m. Color composites of bands 6, 2, 1 (displayed as RGB) are shown in figure 12 and 13 for the LGB/MGB and UGB, respectively. The SWIR band 6 (red in the RGB image) is dominant over most of the LGB and UGB. The red color is a result of a weak absorption in band 6, and strong chlorophyll absorption in bands 2 and 1. However, the hot spring areas are clearly defined in cyan (green + blue, or bands 2 + 1), indicating a strong absorption in band 6 from the hydrothermal alteration minerals. Burned vegetation (fire scars) appears in cyan because of low chlorophyll, indicating a weak absorption in bands 2 and 1.

The Landsat TM 5/7 band ratio highlights altered clay-rich rocks, with a high ratio indicating a high degree of hydrothermal or clay mineral alteration [Sultan et al., 1987]. This ratio corresponds to the ASTER 4/6 band ratio and the AVIRIS 139/195 band ratio, or 1.67 $\mu$ m

/2.22  $\mu\text{m}$ . Table 4 shows the ASTER and AVIRIS band ratios for the fourteen field sites. Altered rocks typically have ratios greater than unity [Sultan et al., 1987]. All the field sites had 4/6 ratios and 139/195 ratios greater than unity, indicating that the band ratio technique accurately identified the rocks present at field sites as hydrothermally altered. Although in most cases, the ASTER and AVIRIS ratios were similar to one another, the AVIRIS ratio was slightly greater than ASTER (Table 4). The sites that exhibited the highest ratios were active Site 13 (ratio = 2.33) and extinct Site 12 (ratio = 2.16). Most of the extinct springs sites not masked by vegetation (i.e. Sites 7, 8, and 12) had a higher 4/6 ratio than active spring sites. Sites 3, 6, and 14 are extinct sites with vegetation covering the alteration, and do not have high 4/6 ratios. The extremely active sites (i.e. Sites 9, 10, and 13) had high 4/6 ratios, but their ratios were not as high the extinct sites. The only exception is Site 4, a very active site exhibiting a high 4/6 ratio (ratio = 1.95).

### **III. ASTER TIR Emissivity and Temperature**

Hydrothermal silica occurs is an important component of most hydrothermal alteration systems. Because silica and other rock-forming minerals have unique spectral features in the TIR region, remote sensing instruments such ASTER with multispectral TIR systems are ideal for detection of these minerals [Gillespie et al., 1984; Hook et al., 1994]. Figure 14 shows an ASTER TIR image of the Lower Geyser Basin. The entire basin is bright compared to the surrounding region, indicating a large thermal anomaly ( $\sim 19.3 \text{ km}^2$ ). In most cases, the active and extinct hot spring areas within the basin are brighter (i.e., warmer) than the overall basin. No detail of the hot springs can be seen in this resolution; only a bright pixel(s) representing the thermal area is evident. Radiance values are shown in Table 5.

The ASTER emissivity product is on provisional release status and cannot yet be considered completely accurate. Although the ASTER emissivity and surface kinetic temperature products were examined, many of the field sites had emissivity values greater than 1.0. Because true emissivity values range from 0-1, the ASTER emissivity values were not evaluated further. In light of this, the emissivity normalization technique was used with a maximum assumed emissivity of 0.985 [Realmuto, 1990].

The ASTER emissivity spectra for each field site can be seen in Appendix D. The field sites occupied an area less than 1 pixel on the ASTER images, where one pixel represents 90 m, respectively. Most of the field sites resembled the emissivity spectrum of silica, with a primary trough at approximately 9.2  $\mu\text{m}$  (Table 6). The depth of the 9.2  $\mu\text{m}$  feature is directly related to the abundance of silica [Hook et al. 1992]. The deeper the spectral feature, the more silica-rich. The depth of the 9.2  $\mu\text{m}$  emissivity feature for each site is shown in Table 7. The emissivity value for the depth of the 9.2  $\mu\text{m}$  absorption feature was averaged for the active and extinct sites. The active sites [Figure 15a] had an average emissivity depth of 0.9665. The extinct sites [Figure 15b] had an average emissivity depth of 0.9622. Therefore, the extinct sites contain more silica than the active sites. Note that the particle size for the mineral grains would be a contributing factor for laboratory emissivity spectra only. Thus, particle size need not be considered here, and emissivity spectral depth for these 90 m pixels simply indicates abundance of materials with depth.

Rocks with increasingly mafic mineralogies exhibit bands that shift to longer wavelengths [Hunt, 1980; Kahle, 1987; Salisbury and D'Aria, 1992]. The emissivity spectra showed no band shifts at any of the field sites, as all of the sites had a distinct absorption feature at 9.2  $\mu\text{m}$ , indicating that the sites had the similar felsic silica mineralogies.

The ASTER acquisition date was November 2000, and although the geothermal features do not vary dramatically in temperature throughout the year, mixing of ground cover types (including mineral deposits, vegetation, rock/soil, and water) is assumed. Because of this mixing in the 90 m spatial resolution of the TIR, the derived kinetic temperatures were not as high as the temperatures measured with the field radiometer. Table 8 shows the kinetic temperatures for each of the field sites. Most of the active sites visited had small thermal features (from ~ 1- 30 m<sup>2</sup>). The largest active thermal feature was at Sunset Lake, corresponding to a third of a pixel in the ASTER TIR region. The extinct fields were generally larger in size (from ~ 30 – 270 m<sup>2</sup>). The largest extinct thermal feature was at the Iris Group, corresponding to several pixels in the ASTER TIR region. The sites that had the highest kinetic temperatures were Site 9 (active; 17.2 °C), Site 8 (extinct; 15.9 °C), Site 12 (extinct; 11.9 °C), Site 13 (active; 9.3 °C), and Site 10 (active; 9.2 °C). The other sites ranged in temperature from 2.9 – 7.1 °C. Several of the extinct springs had some of the highest calculated temperatures, indicating that thermal anomalies still can be identified from sites no longer considered active.

#### **IV. Normalized Difference Vegetation Index (NDVI)**

Geobotanical remote sensing is important because many unexplored areas for metals are heavily vegetated [Vincent, 1997]. NDVI is common remote sensing technique that can determine the robustness of vegetation cover [Vincent, 1997]. NDVI is a ratio of the visible and near-infrared bands [Vincent, 1997]. For ASTER, the NDVI equation is as follows: (Band 3 – Band 2) / (Band 3 + Band 2). This equation was applied to the images and a measure of the “greenness index” was determined. The bright pixels in the image represent a high NDVI (close

to 1), indicating much vegetation. The dark pixels represent a low NDVI (close to zero), indicating little vegetation. NDVI successfully determined the vegetation concentrations, showing low to moderate vegetation coverage in the area. The ASTER NDVI images were noisier than the AVIRIS NDVI images because of the broader band passes. Table 9 shows the NDVI ratios for each of the fourteen field sites. The extinct sites had an average NDVI value of 0.1719. The active sites had an average NDVI value of 0.1689. Thus, this suggests the extinct sites have more robust vegetation than the active sites. The active sites eject hot waters that destroy most of the vegetation during eruptions. The dormancy of the extinct sites permits vegetation growth. However, field surveys indicated that for both the active and extinct sites, vegetation is generally present surrounding the sinter, and relatively little vegetation actually grows on the sinter itself. Consolidated sinter does not seem to provide a good substrate for vegetation growth. As previously mentioned, most of the active and extinct springs are small features less than 15 m. Most of the calculated NDVI values are a measure of vegetation for the entire 15 m pixel, and the values reflect the vegetation surrounding the springs, rather than the vegetation within the springs.

## **V. Classifications**

### **A. Unsupervised Classification**

A k-means classification was performed on the ASTER VNIR scenes of the geyser basins. The k-means approximation is the most common clustering method [Vincent, 1997], which requires the user to specify the number of clusters to be classified. The algorithm locates the data clusters and their centers. A pixel is assigned to each cluster, and means and vectors are

recomputed, and statistical separation of each class is rechecked. A maximum of seven classes were selected using 10 iterations. The occurrence of non-intuitive classes was prevented by setting the maximum value at a low number.

Class statistics are as shown in Table 10. Field observations were compared to the pixels of each cluster class. Although every pixel in the scenes was classified, there were some pixels that were clearly misclassified. For example, the forest and other vegetation classes were commonly misidentified as one another. Also, the manmade areas were overestimated. However, the unsupervised classification successfully identified basin areas and identified areas of siliceous sinter (Figure 16a and 16b). However, this classification was unable to identify the entire extent of the siliceous sinter. Other errors include the water and shadows pixels that were misidentified as one another. Despite some of these expected errors in the iterations, the classes seem to best represent water, hot spring deposits, manmade features (roads, boardwalks, parking lots), forest/moist to wet grass, bacterial mat, dry grass/soil/swamp, and fire scars.

Unsupervised ISODATA (Iterative Self-Organizing Data Analysis Technique Algorithm) classifications were also performed on the scenes. ISODATA is commonly used on multispectral data sets to create land cover maps [Spruce, 2001]. The ISODATA results yielded similar results to the k-means approximation, as the classes identified in both algorithms covered the same areas of the images. Cluster-busting techniques (i.e. masking to isolate raw data) may have been necessary to reduce misclassification. But even with these techniques, ISODATA and k-means approximations cannot map rare and spectrally subtle features [Spruce, 2001]. The classifications are further hindered by the large pixel sizes of the data sets. However, these classifications seem to be sufficient for broad land cover classification of common types within the scenes [Spruce, 2001].

## **B. Supervised Classification**

After ground truth of several ground cover types in the geyser basins, an identity of classes was known. A supervised classification was done for the VNIR, SWIR regions of ASTER and AVIRIS, and the TIR of ASTER. Classifications were not performed on the full ASTER scenes; a portion (17 km by 13.8 km) pertaining only to the LGB, MGB, and UGB was selected. The VNIR classifications were divided into 2 scenes for ASTER: LGB (that included the MGB) and UGB.

The VNIR region was used in the classifications, because it has the best spatial resolution available (15m in ASTER); thus classifications in this region yielded more accurate classifications than in the other wavelength regions. A maximum likelihood classification was used. The maximum likelihood classification is generally the most accurate method of classification, although it requires a long computer run time and requires a large number of pixels to accurately define the classes [Vincent, 1997]. The classification creates an n-dimensional ellipsoid around each class and statistically determines whether an unknown pixel falls into the ellipsoid. The algorithm was run using a zero probability threshold, allowing all pixels to be classified. The ground coverage types were divided into 8 main classes: water, shadows, hot spring deposits, manmade features (roads, boardwalks, parking lots), forest/moist to wet grass, bacterial mat, dry grass/soil/swamp, and fire scars. ROIs (regions of interest) were selected by drawing polygons around the desired pixel clusters. Class statistics are shown in Table 11.

Rule images were created and examined for each of the classes. Rule images allow each class to be extracted as a separate image in order to analyze individual classes. The ENVI color table was applied to the rule images to better visualize each class. In each rule image, the black areas were chosen to contain the specified class, and the white areas were chosen to not contain

the specified class. In some cases (i.e. the mat rule image), only the darkest black areas contain the class; the lighter black areas do not. Water and shadow pixels were originally identified in their appropriate class. However, the classification algorithm misidentified one as the other, and combined them as one class for the LGB. For the UGB scene, the water and shadows were successfully separated. The algorithm also confused some of the bright areas of the forest (areas of high NIR reflectance) and identified them as mat. Also, the manmade class was overestimated, but the limitations of the algorithm prevented proper correction of this class. Despite these minor errors, the rule images of the supervised classification concur with the ground truth study of these basins.

In contrast to the unsupervised classification (Figure 16), figure 17a and 17b clearly show that the classes were better delineated for the supervised classification. There are only minor numbers of misclassified pixels.

### **C. Spectral Angle Mapper**

This technique, developed by J.W. Boardman, matches image spectra to reference spectra in n-dimensions [Yuhas et al., 1992]. Spectral Angle Mapper (SAM) compares the angle between end member spectra and each pixel in n-dimensional space (Yuhas, et al., 1992). SAM produces a classified image and a set of rule images based on the SAM maximum angle threshold. The SAM technique was performed on the AVIRIS image of the geyser basins. The angle chosen was 0.1, a commonly used SAM angle. If the angle is too high, the image will be more spatially coherent, but the pixel matches will not be as good. A total of 42 end members were found using the ENVI Spectral Wizard, a technique where the computer defines potential end members. However, 21 of these end members spectrally overlapped with other end members, so only 21 end members are considered. Figure 18 shows the classified SAM image using the ENVI Wizard. Within this image, at least five minor changes of vegetation can be

discriminated. Forest vegetation (magenta) dominates most of the scene. It is also evident that water and shadows (black) could not be separated from each other. Thermally altered areas show up in a several different classes, indicating that their spectral response is varied. The variation is especially different in locations such as the Fountain Paint Pots area, an extremely diversified area with geysers, hot springs, and fumaroles, and multi-colored mudpots. This area has a variety of different minerals that can be individually discriminated as individual classes.

<b>Site No.</b>	<b>ASTER 4/6 ratio</b>	<b>AVIRIS 139/195 ratio</b>
1 White Creek Group	1.53 – 1.55	1.55 – 1.61
2 Firehole Lake Group	1.34 – 1.42	1.37 – 1.46
3 The Ruin	1.63	1.41
4 Fortress Geyser	1.69 – 1.71	1.65 – 1.95
5 Rabbit Creek Hot Springs	1.54 – 1.61	1.21 – 1.25
6 Morning Mist	1.40 – 1.76	1.55 – 1.66
7 Fountain Flats	1.57– 1.78	1.42 –1.87
8 Extinct unnamed	1.61 – 1.66	1.78 – 1.93
9 Sunset Lake	1.48 – 1.65	1.43 – 1.54
10 Sapphire Pool	1.55 – 1.58	1.60 – 1.62
11 Mallard Lake Group	1.66 – 1.86	1.28 – 1.76
12 Iris Group	1.58 – 1.73	1.80 – 2.16
13 White Dome	1.59 – 1.68	1.00 – 2.33
14 Fracture Group	1.48 – 1.53	1.33 – 1.34

**Table 4** ASTER 4/6 and AVIRIS 139/195 SWIR band ratios.

Site No.	Radiance Values (W/m <sup>2</sup> /sr/μm)				
	Band 14	Band 13	Band 12	Band 11	Band 10
1	6.36	6.40	6.04	5.78	5.43
2	6.67	6.84	6.54	6.39	6.12
3	6.68/6.66	6.76/6.69	6.28/6.26	6.07/6.03	5.96/5.80
4	6.56- 6.60	6.61 - 6.73	6.24 – 6.39	6.07 – 6.26	5.72 – 6.01
5	6.62	6.73	6.38	6.20	5.99
6	6.28/6.38	6.32/6.47	5.93/6.10	5.67/5.83	5.45/5.55
7	6.49/6.38	6.60/6.44	6.17/6.08	5.95/5.77	5.69/5.48
8	7.47	7.91	7.72	7.58	7.38
9	6.61/7.33/7.90	6.65/7.24/8.16	6.22/6.89/8.12	6.01/6.71/7.88	5.79/6.43/7.49
10	6.97	7.15	6.83	6.66	6.41
11	6.55/6.69	6.68/6.75	6.33/6.48	6.14/6.17	5.84/5.93
12	7.27	7.44	7.13	7.02	6.80
13	6.81	6.93	6.63	6.40	6.19
14	6.57	6.66	6.29	6.06	5.74

**Table 5** ASTER Radiance values for the fourteen field sites.

Site No.	8.3 $\mu\text{m}$	8.65 $\mu\text{m}$	9.1 $\mu\text{m}$	10.6 $\mu\text{m}$	11.3 $\mu\text{m}$
1 White Creek Group	t	p	t	-	p
2 Firehole Lake Group	p	-	t	p	t
3 The Ruin	p	-	t	-	p
4 Fortress Geyser	p	-	t	p	t
5 Rabbit Creek Hot Springs	p	-	t	p	t
6 Morning Mist	t	-	t	p	t
7 Fountain Flats	t	-	-	-	p
8 Extinct unnamed	p	-	t	p	t
9 Sunset Lake a) extinct b) active	a) t b) p	a) p b) -	a) t b) t	a) - b) -	a) p b) p
10 Sapphire Pool	p	-	t	p	t
11 Mallard Lake Group a) b)	a) p b) t	a) t b) p	a) p b) t	a) t b) p	a) p b) t
12 Iris Group	p	-	t	p	t
13 White Dome	p	-	t	-	-
14 Fracture Group	t	p	t	-	p

**Table 6** Shape of emissivity spectra for the fourteen field sites.

Site No.	Emissivity depth at 9.2 $\mu$ m
1 White Creek Group	0.9725
2 Firehole Lake Group	0.96625
3 The Ruin	0.945
4 Fortress Geyser	0.96
5 Rabbit Creek Hot Springs	0.960625
6 Morning Mist	0.978667
7 Fountain Flats	0.97625*
8 Extinct unnamed	0.96
9 Sunset Lake	0.955625
10 Sapphire Pool	0.96625
11 Mallard Lake Group	0.9815*
12 Iris Group	0.955625
13 White Dome	0.96875
14 Fracture Group	0.974

\* These are not troughs

**Table 7** Depth of the 9.2  $\mu$ m feature.

Site No.	Kinetic Temperature (°C)	Kinetic Temperature (°C)
	Normalization Technique	ASTER product
1 White Creek Group	2.9	1.5
2 Firehole Lake Group	7.1	6.1
3 The Ruin	5.9	6.7
4 Fortress Geyser	6.3	5.1
5 Rabbit Creek Hot Springs	6.1	5.1
6 Morning Mist	3.1	2.7
7 Fountain Flats	3.0	2.0
8 Extinct unnamed	15.8	16.7
9 Sunset Lake	5.2 – 17.2	3.5 – 16.5
10 Sapphire Pool	9.2	8.4
11 Mallard Lake Group	3.4 – 5.8	2.3 – 5.3
12 Iris Group	11.9	10.7
13 White Dome	9.6	10.6
14 Fracture Group	4.8	4.1

**Table 8** Kinetic Temperatures for the fourteen field sites.

Site No.	NDVI value
1 White Creek Group	0.155 – 0.279
2 Firehole Lake Group	0.198 – 0.281
3 The Ruin	0.228
4 Fortress Geyser	0.174 – 0.246
5 Rabbit Creek Hot Springs	0.176 – 0.220
6 Morning Mist	0.132
7 Fountain Flats a) active b) extinct	a) 0.186 – 0.194 b) 0.100
8 Extinct unnamed	0.180
9 Sunset Lake	0.079 – 0.256
10 Sapphire Pool	0.112 – 0.127
11 Mallard Lake Group	0.208 – 0.302
12 Iris Group	0.063 – 0.142
13 White Dome	0.088 – 0.115
14 Fracture Group	0.184 – 0.220

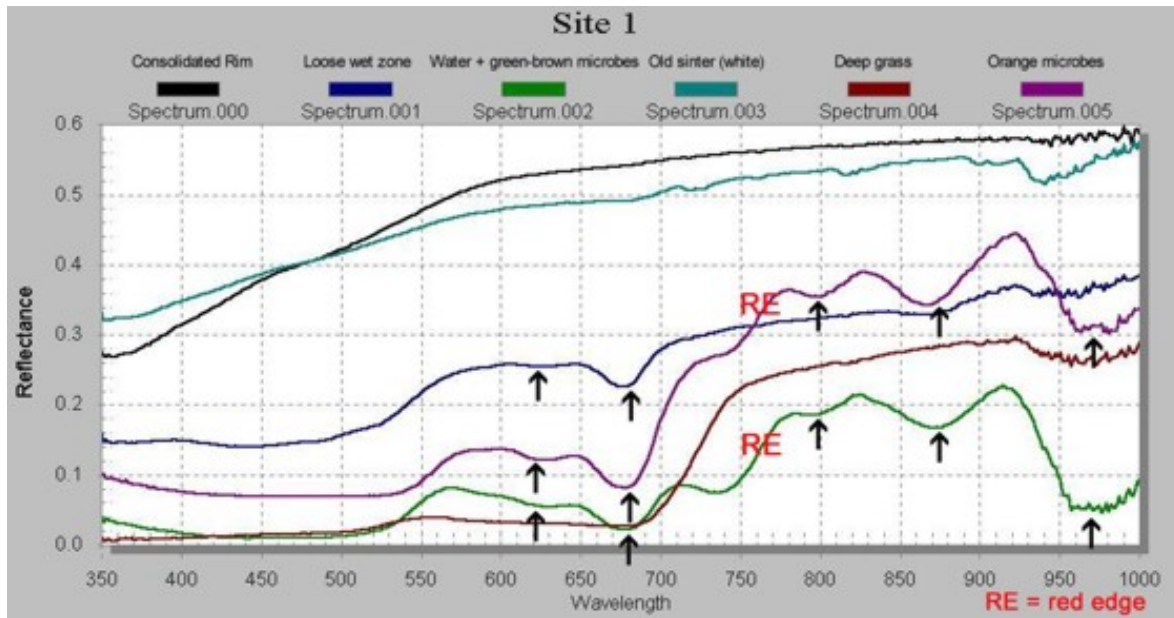
**Table 9** NDVI values for the fourteen field sites.

<b>Geyser Basin</b>	<b>class</b>	<b># pixels classified</b>	<b>% classified</b>
Lower and Midway	1	64610	5.3975
	2	317547	26.5277
	3	273648	22.8604
	4	189705	15.8479
	5	146630	12.2494
	6	128844	10.7636
	7	76055	6.3536
Upper	1	94473	11.7591
	2	175835	21.8863
	3	159177	19.8128
	4	121970	15.1817
	5	103375	12.8671
	6	88784	11.0510
	7	59789	7.442

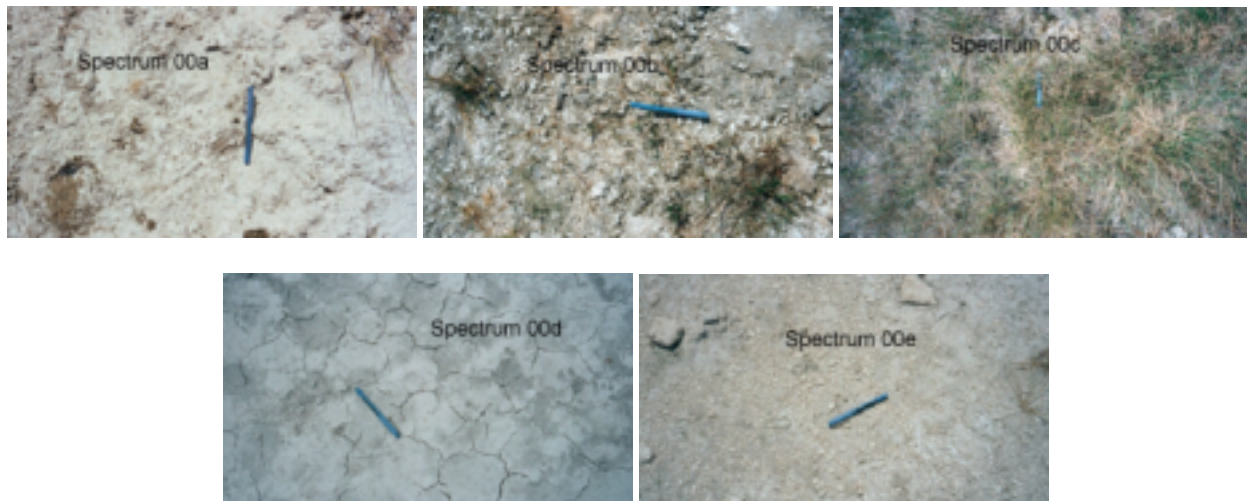
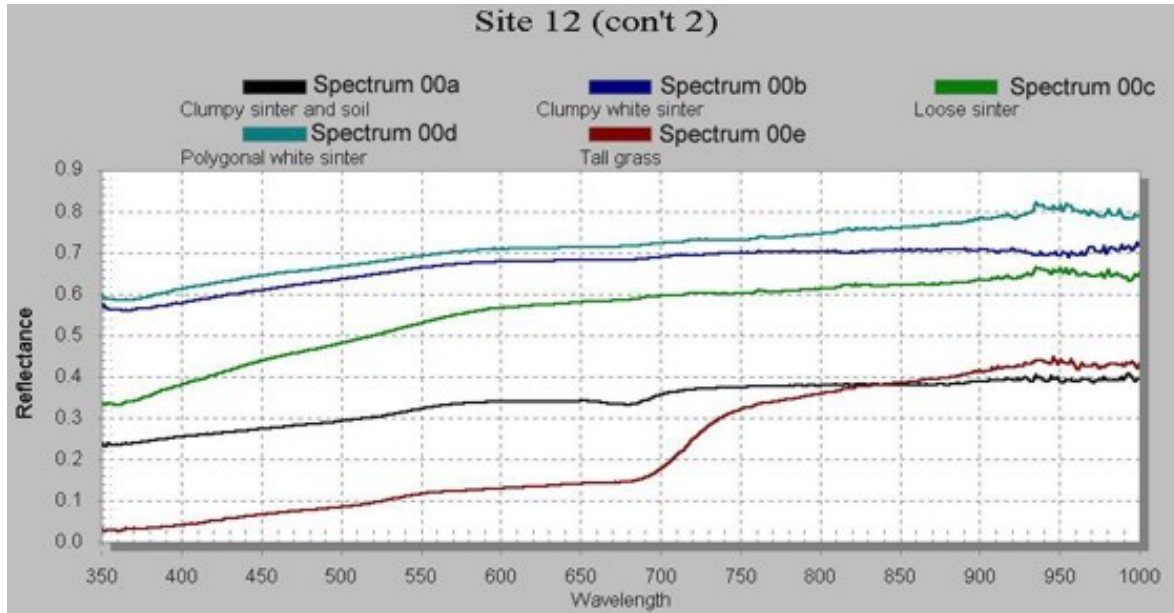
**Table 10** Class statistics for unsupervised k-means classification.

<b>Geyser Basin</b>	<b>class</b>	<b># pixels classified</b>	<b>% classified</b>
Lower and Midway	1 – water/shadows	42175	3.52
	2 – spring deposits	66709	5.57
	3 – manmade	91640	7.66
	4 - forest	630578	52.68
	5 - mat	49109	4.10
	6 - other (soil/swamp)	100086	8.36
	7 – fire scars	216742	18.11
Upper	1 - water	17841	2.22
	2 – spring deposits	51276	6.38
	3 – manmade	122672	15.27
	4 - forest	423731	52.74
	5 - mat	17659	2.20
	6 - other (soil/swamp)	17183	2.14
	7 – shadow	48352	6.02
	8 – fire scars	104689	13.03

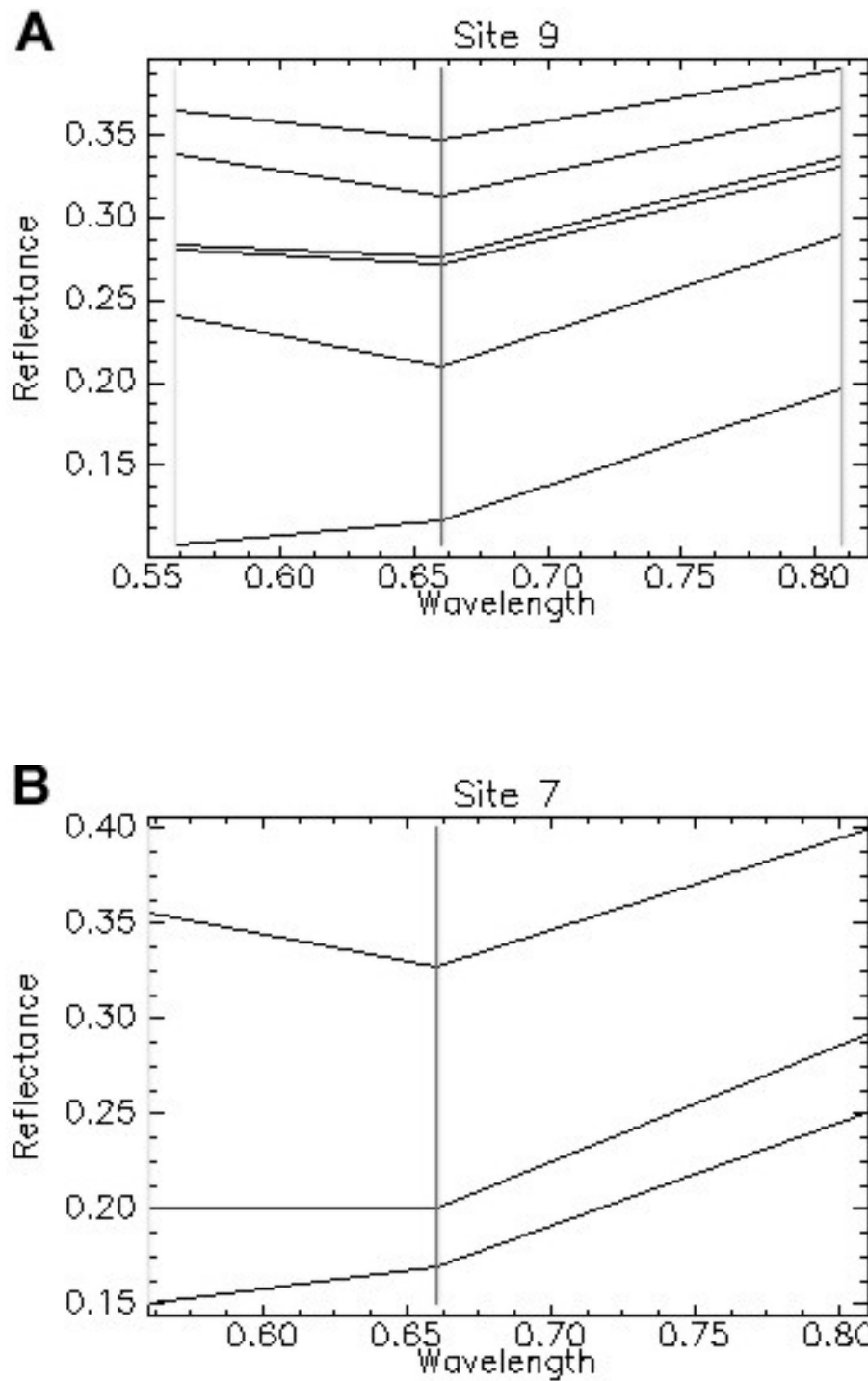
**Table 11** Class statistics for the supervised classification.



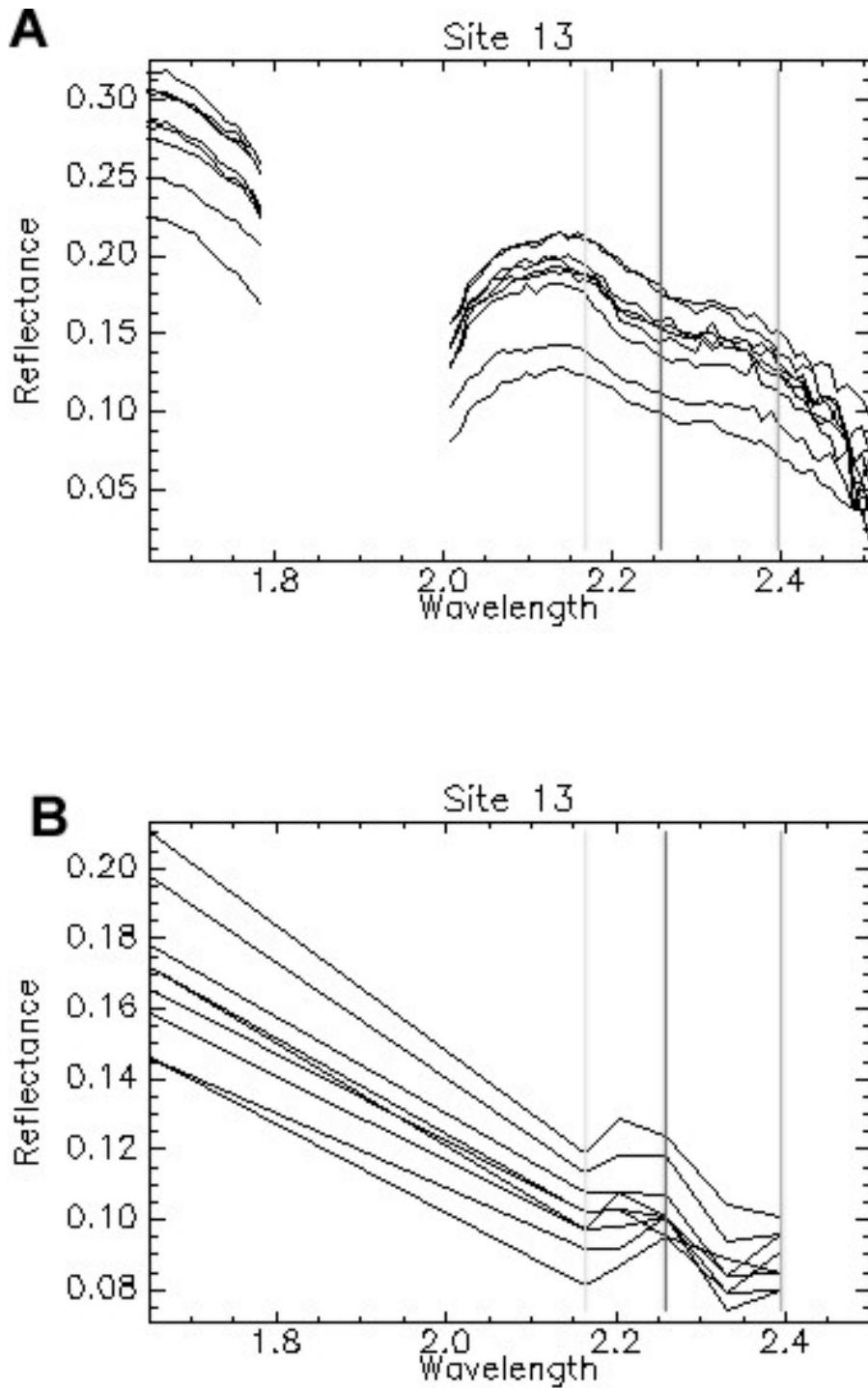
**Figure 8a** Example of the VNIR field spectra collected with the ASD instrument (wavelength range is 0.350 – 1.000 μm). White Creek Group (site 1) is an active spring in the Lower Geyser Basin. Hot springs bacteria and algae have unique spectra compared to vegetation. Chlorophyll and water absorptions are also identified. Each photograph shows the material for the particular field spectrum collected (*see text for descriptions*).



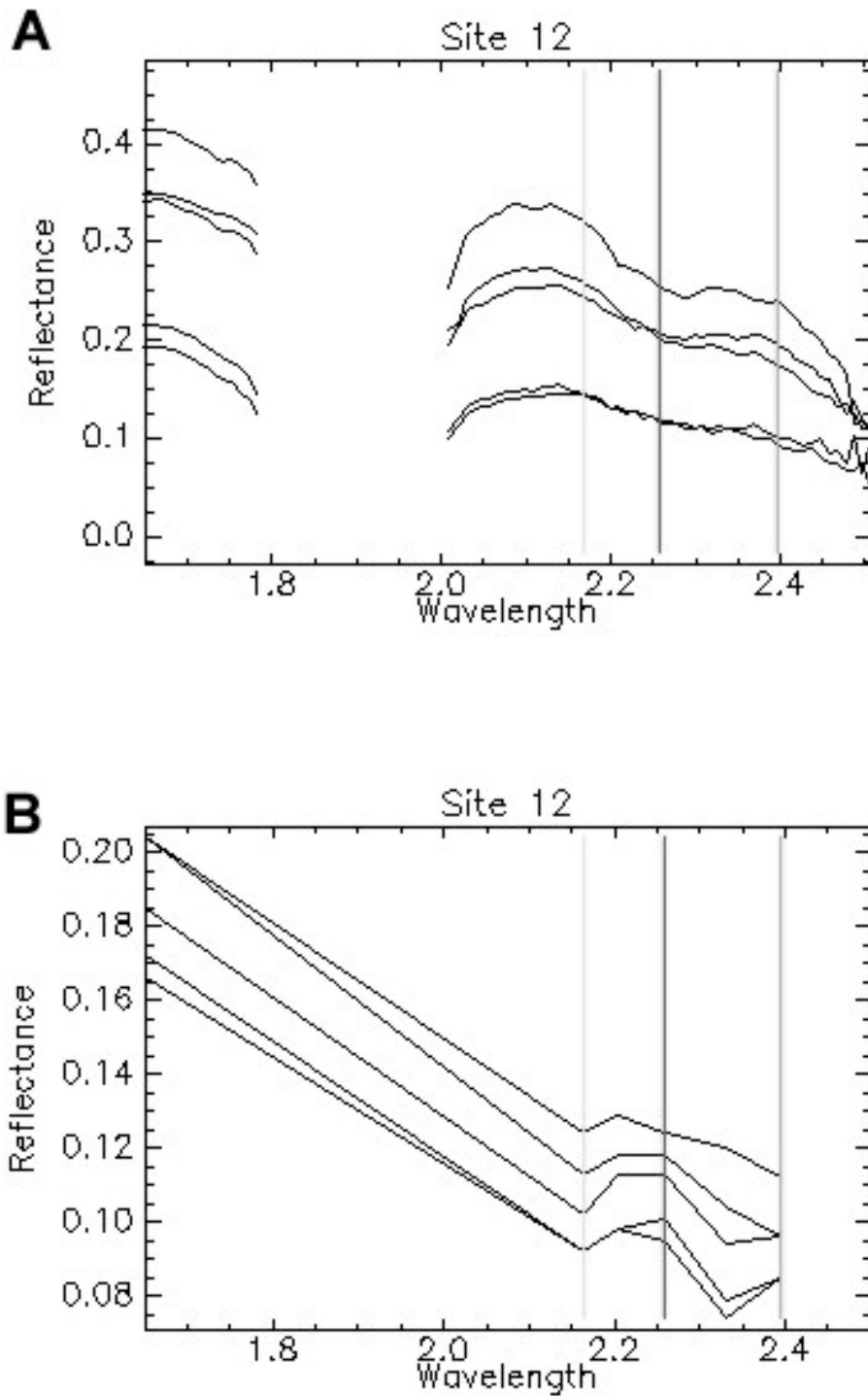
**Figure 8b** Example of the VNIR field spectra collected with the ASD instrument (wavelength range is 0.350 – 1.000  $\mu\text{m}$ ). Iris Group (site 12) is an extinct spring in the Midway Geyser Basin. The extinct sinter has flat, featureless spectra in this region. Vegetation spectra are also identified. Each photograph shows the material for the particular field spectrum collected (*see text for descriptions*).



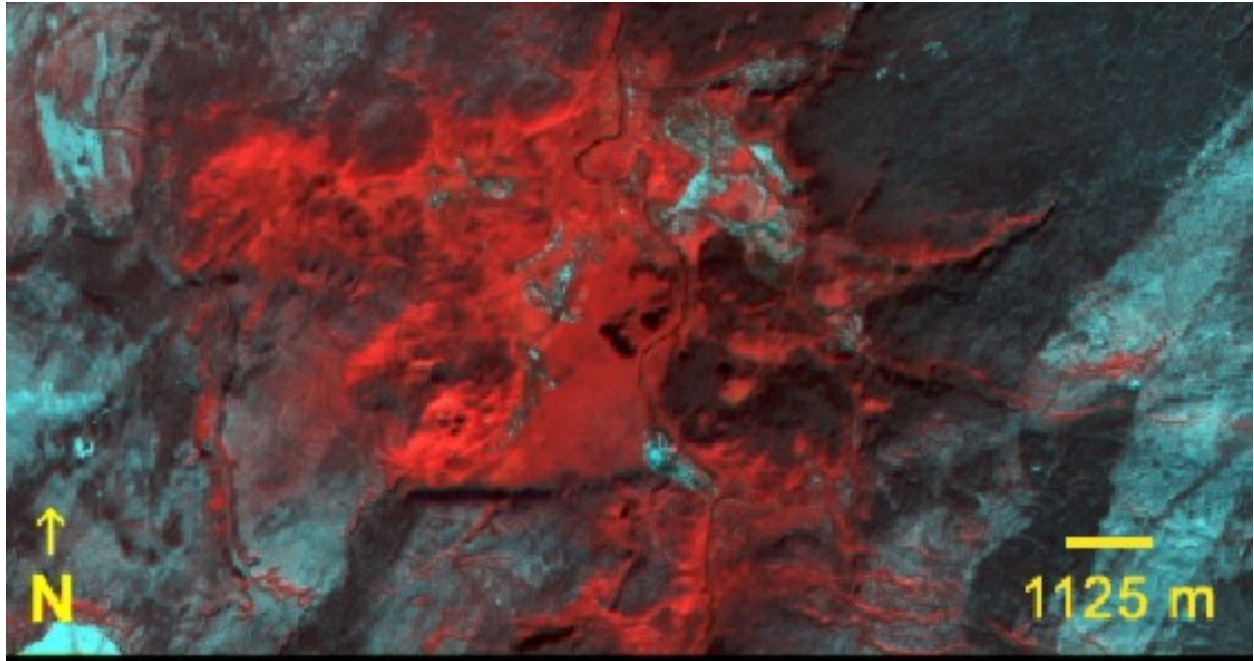
**Figure 9** ASTER VNIR reflectance spectra , with band 3 = (0.76 – 0.86 μm), band 2 = (0.63 – 0.69 μm), and band 1 = (0.52 – 0.60 μm). (A) Sunset Lake (site 9) is an active spring in the Upper Geyser Basin. (B) Fountain Flats (site 7) is an extinct spring in the Lower Geyser Basin. The spectra are vegetation dominated, however they do not resemble pure vegetation. Spectral mixing with the soil background is likely because of the higher reflectance in the 0.52 – 0.69 μm region.



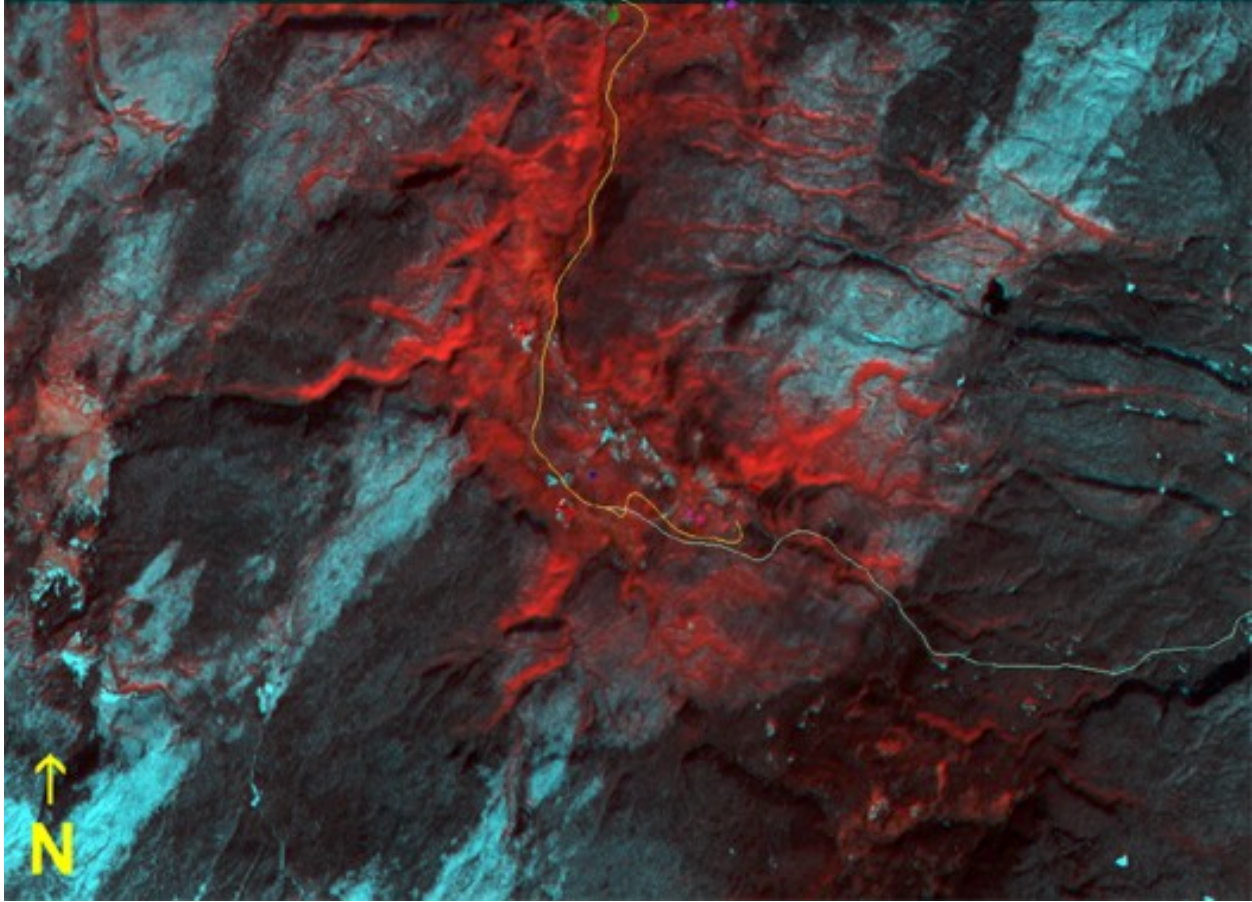
**Figure 10** SWIR reflectance spectra from White Dome (site 13) in the Lower Geyser Basin (an active spring). (A) AVIRIS spectra (1.65 - 2.51  $\mu\text{m}$ ) showing the absorption feature of siliceous sinter at 2.25  $\mu\text{m}$ . (B) ASTER reflectance spectra (1.65 - 2.40  $\mu\text{m}$ ) showing that the siliceous sinter cannot be easily identified due to the broader spectral band passes. The spectra most resemble a mix of dry and green vegetation, but significant spectral mixing occurs.



**Figure 11** SWIR reflectance spectra from the Iris Group (site 12) in the Midway Geyser Basin (an extinct spring). (A) AVIRIS spectra (1.65 - 2.51  $\mu\text{m}$ ) showing the deeper absorption feature of siliceous sinter at 2.25  $\mu\text{m}$  as compared to Figure 10a. A subtle reflectance peak is also located near 2.4 microns and not observed in the active site spectra. (B) ASTER reflectance spectra (1.65 - 2.40  $\mu\text{m}$ ) also showing the lack of a positive identification of siliceous sinter. The spectra most resemble a mix of dry and green vegetation, but significant spectral mixing occurs.



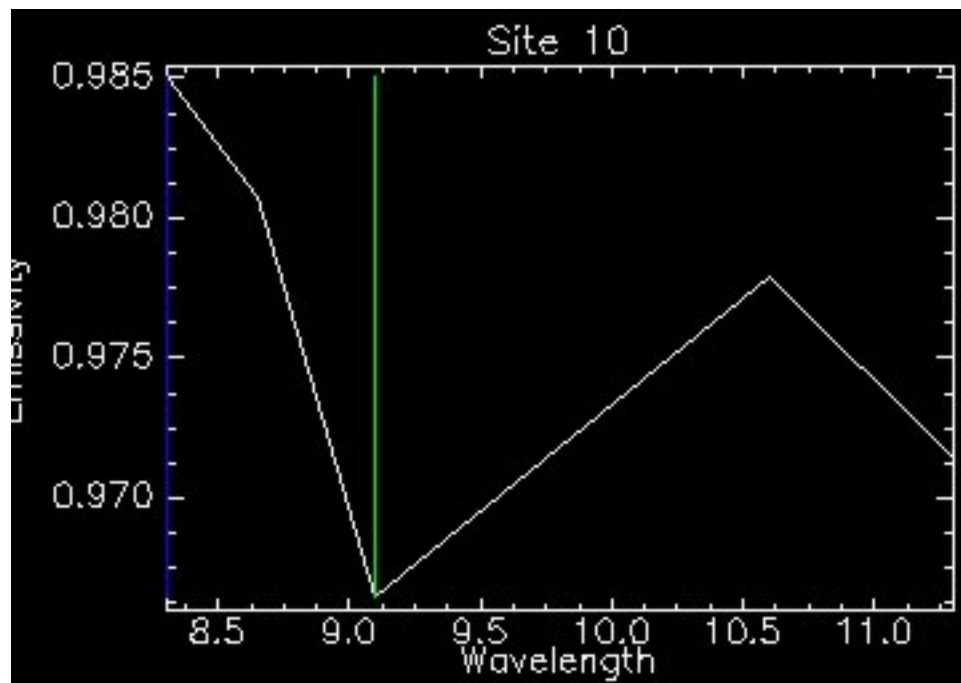
**Figure 12** ASTER RGB color composite of bands 6,2,1 of the Lower and Midway Geysers Basins. Hot spring areas defined in cyan (bands 2 + 1), indicating a strong absorption in band 6 from the hydrothermal alteration minerals.



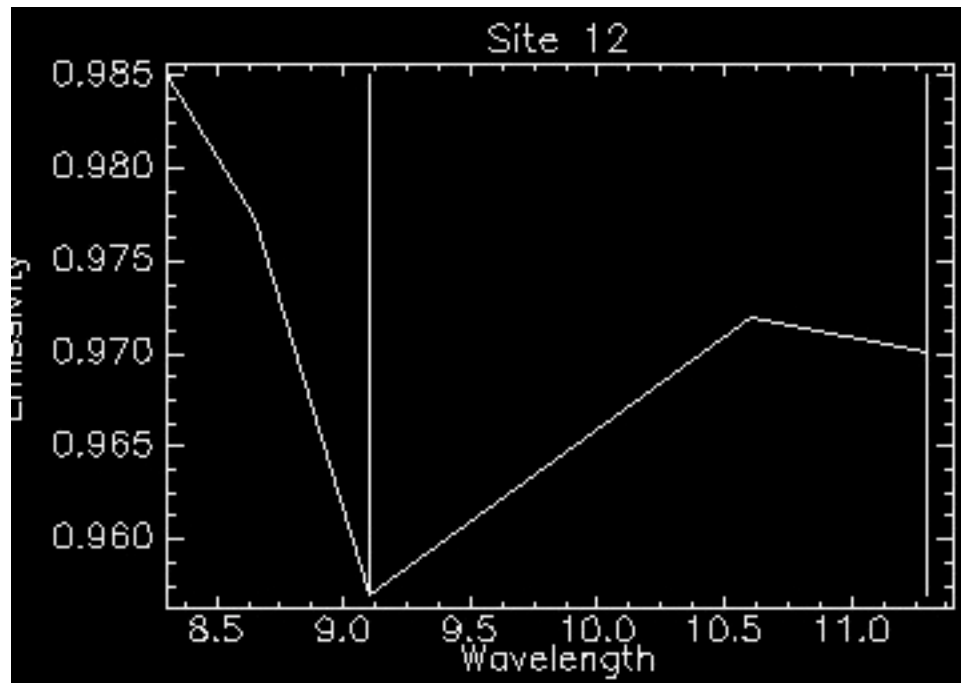
**Figure 13** ASTER RGB color composite of bands 6,2,1 of the Upper Geyser Basin. Hot spring areas defined in cyan (bands 2 + 1), indicating a strong absorption in band 6 from the hydrothermal alteration minerals. Note: scale is same as Figure 12.



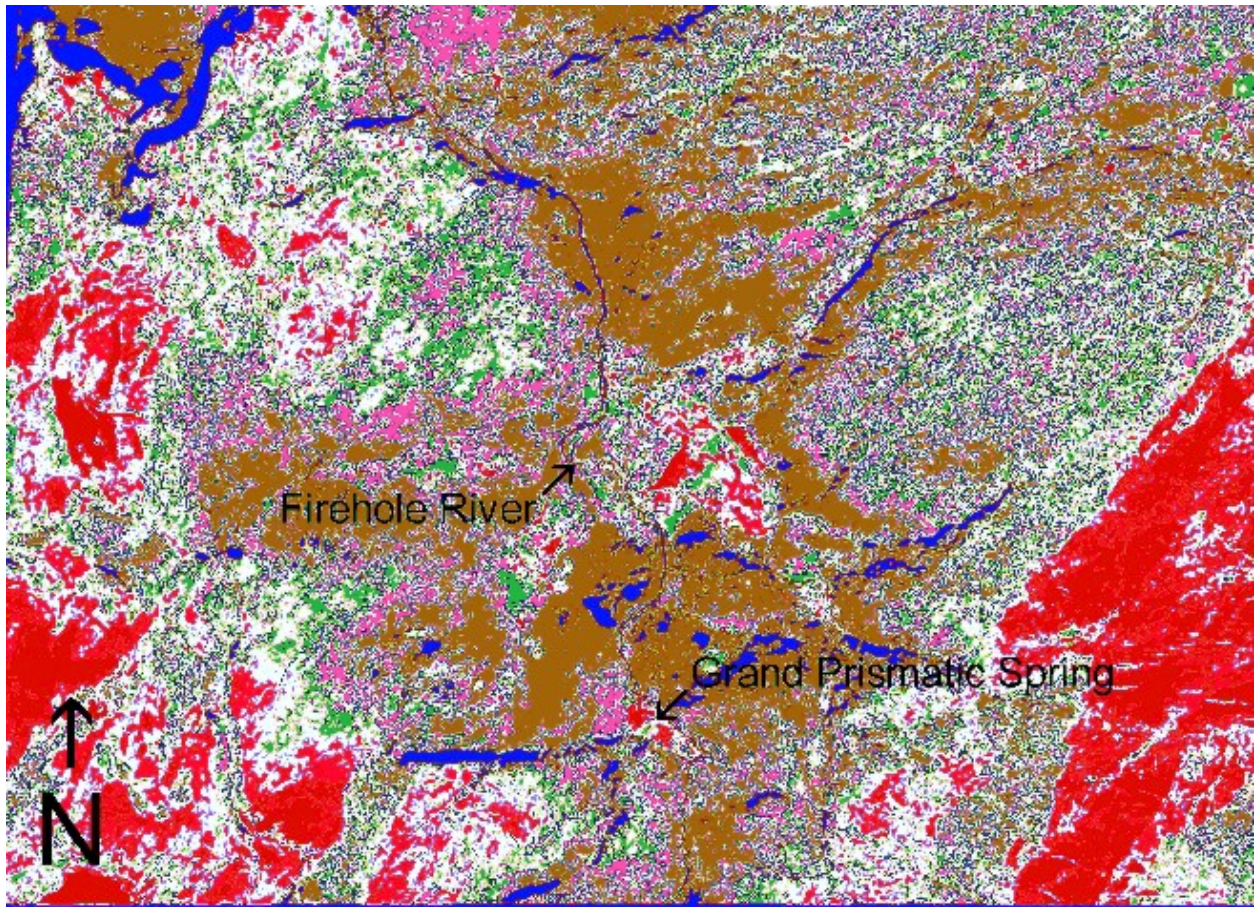
**Figure 14** ASTER thermal infrared image of the LGB and MGB with GPS overlay, with band 14 ( $10.95 \mu\text{m} - 11.65 \mu\text{m}$ ), band 12 ( $8.925 - 9.275 \mu\text{m}$ ), and band 10 ( $8.125 \mu\text{m} - 8.475 \mu\text{m}$ ) in red, green, blue, respectively. Field sites within the basin are numbered. The entire basin is brighter than the surrounding region, indicating a large thermal anomaly. Active and extinct hot spring areas within the basin are brighter (warmer) than the overall basin, however, the individual hot springs cannot be identified at this resolution.



**Figure 15a** Typical emissivity spectrum of an active site (Site 10) showing absorption at 9.2 microns. Spectrum is for one 90 m pixel.



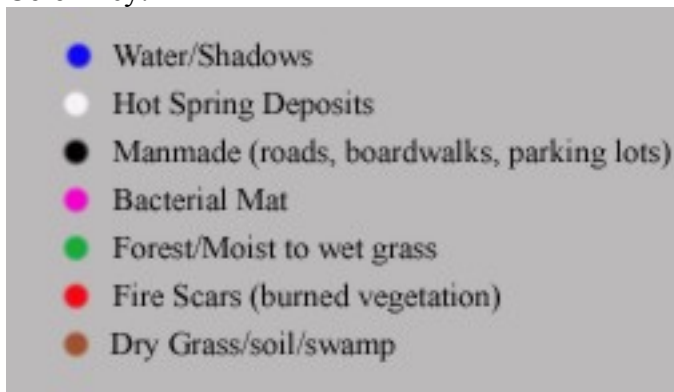
**Figure 15b** Typical emissivity spectra of an extinct site (Site 12) showing absorption at 9.2 microns. Spectrum is for one 90 m pixel.

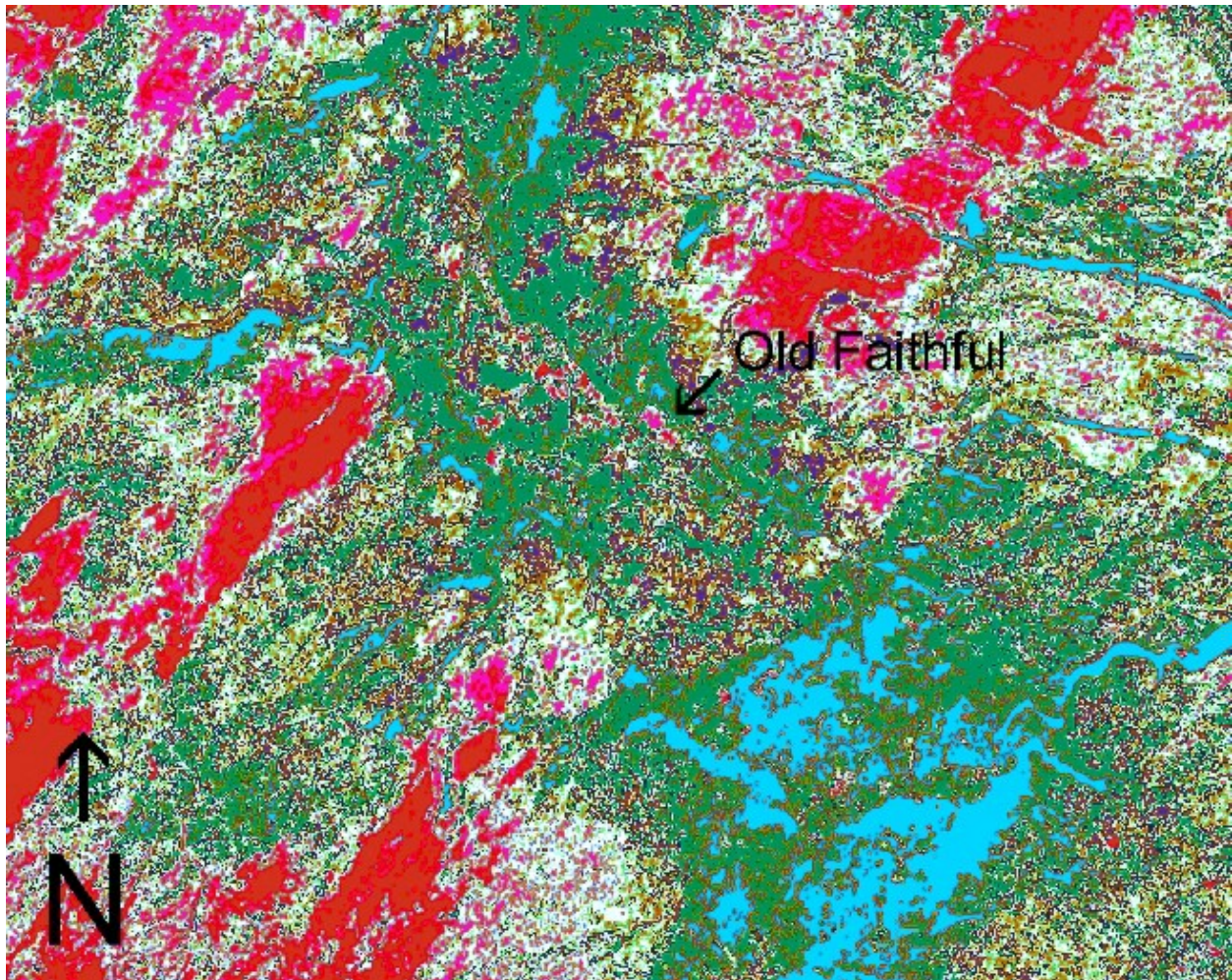


**Figure 16a** Unsupervised k-means classification of the LGB and MGB using the 3 VNIR bands of ASTER. The ground coverage types were divided into 7 main classes, as seen in the color key below.

Note: See supervised classification in Figure 17a for improved accuracy.

Color Key:

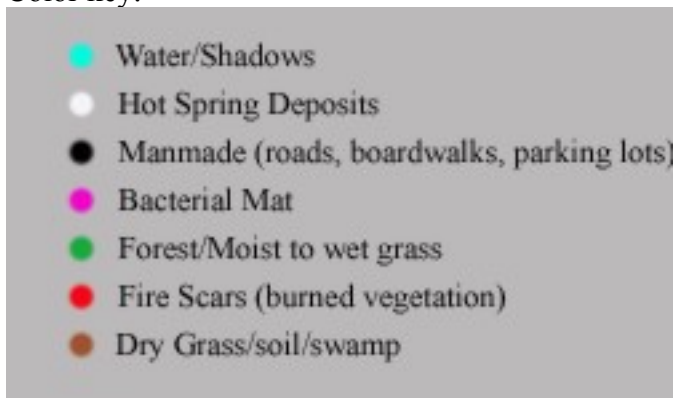


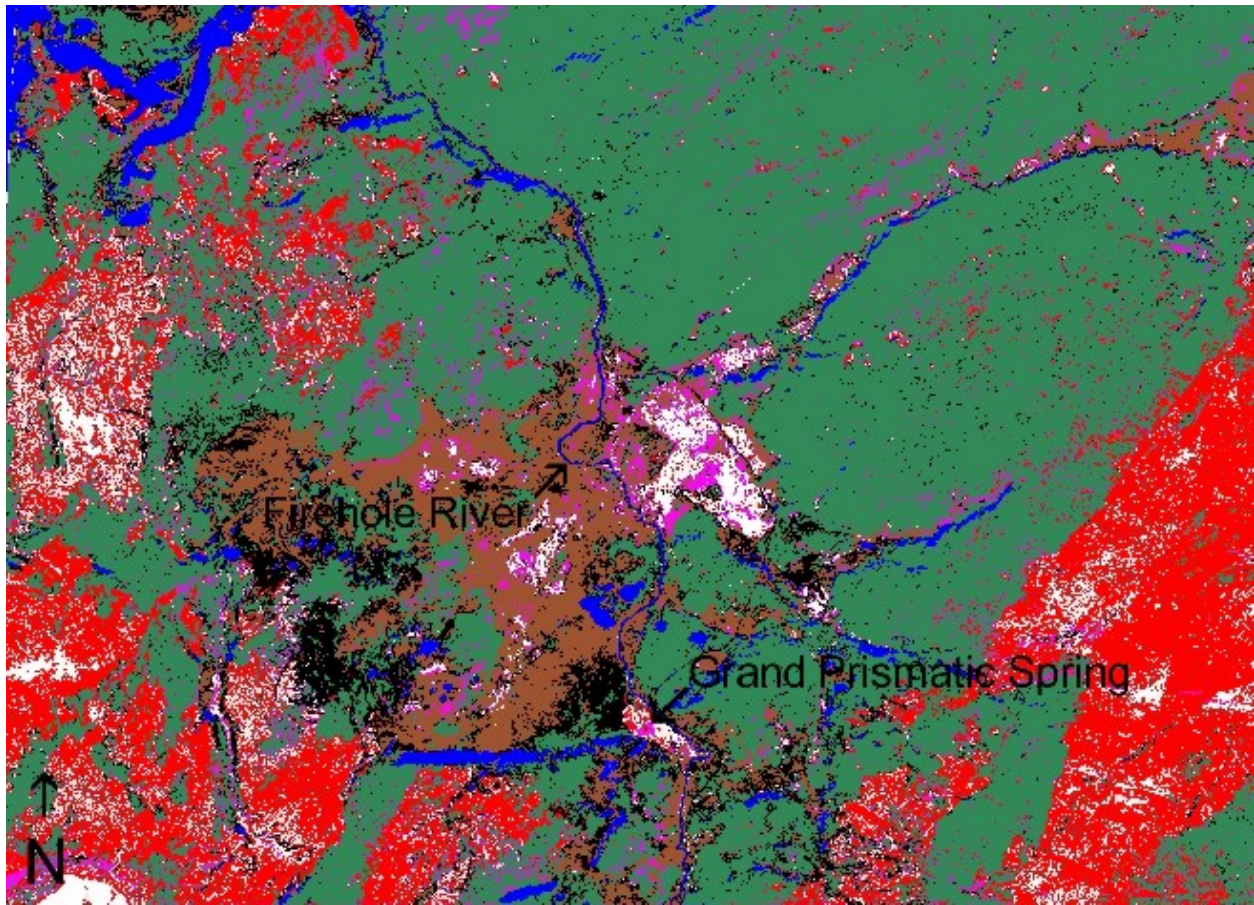


**Figure 16b** Unsupervised k-means classification of the UGB using the 3 VNIR bands of ASTER. The ground coverage types were divided into 7 main classes, as seen in the color key below.

Note: See supervised classification in Figure 17b for improved accuracy.

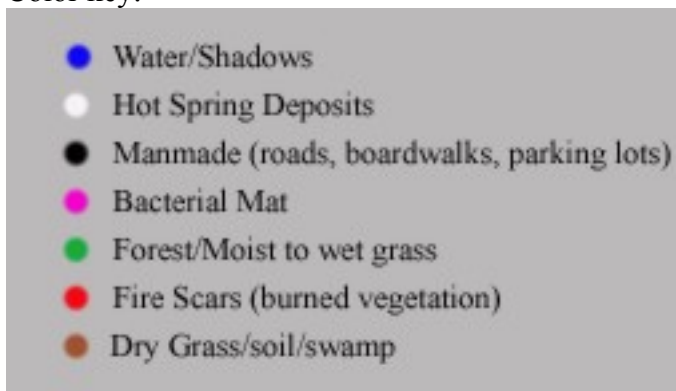
Color key:

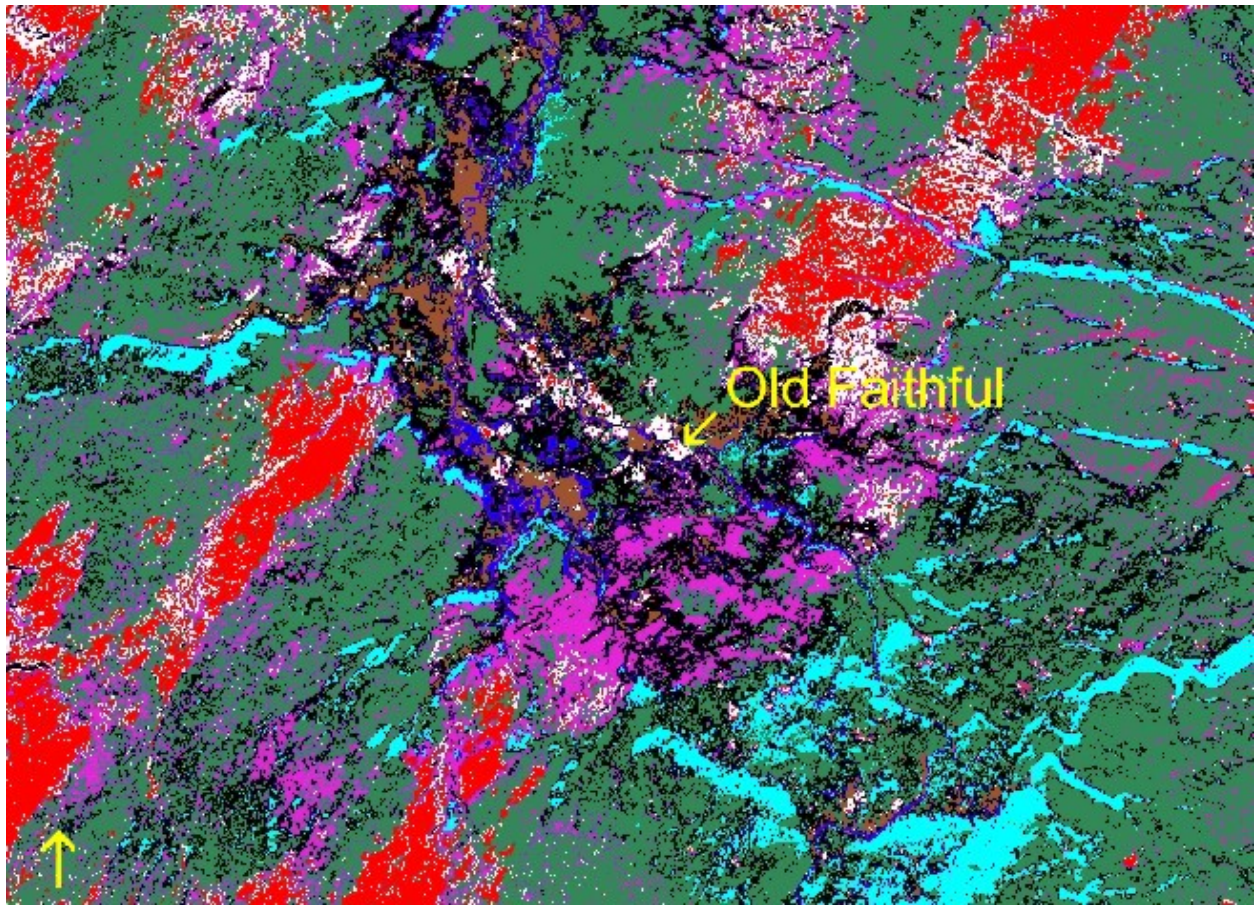




**Figure 17a** Supervised maximum likelihood classification of the LGB and MGB using the 3 VNIR bands of ASTER. The ground coverage types were originally divided into 8 main classes, although 7 classes were ultimately delineated. See color key below for class identifications.

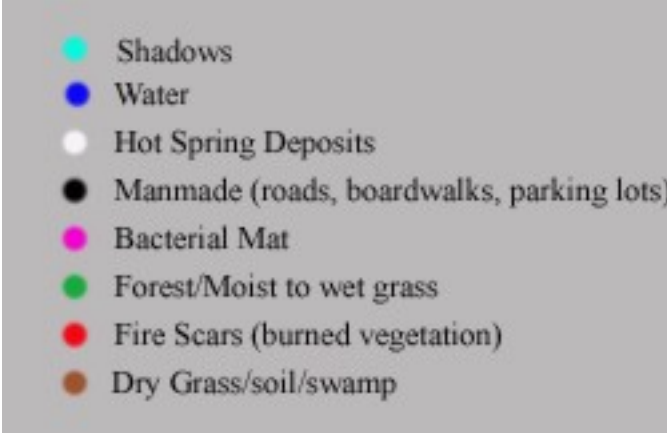
Color key:





**Figure 17b** Supervised maximum likelihood classification of the UGB using the 3 VNIR bands of ASTER. The ground coverage types were divided into 8 main classes, as seen in the color key below.

Color key:



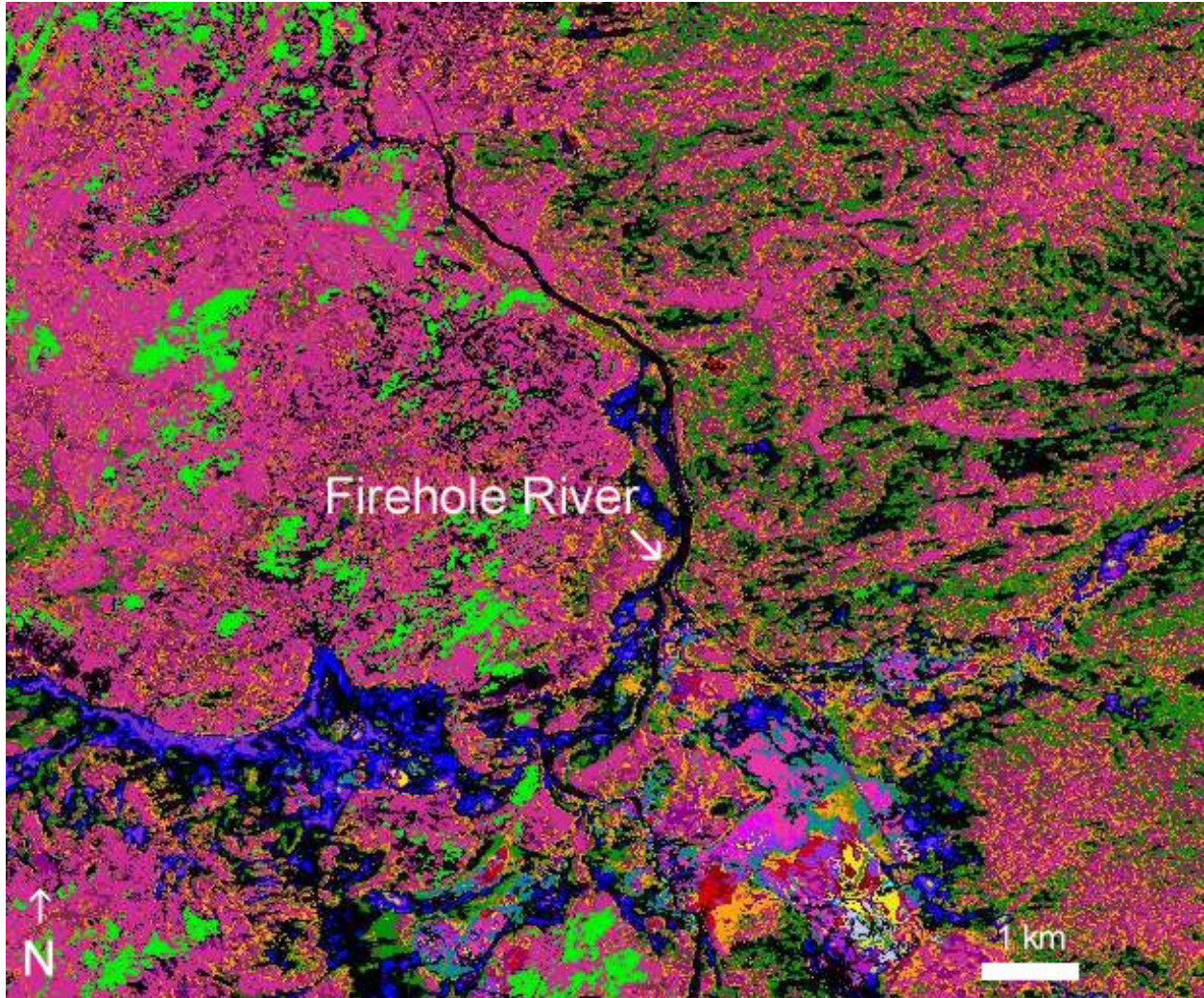


**Figure 18** Spectral angle mapper classification of the LGB AVIRIS scene.

## **Section 5: Discussion**

Each selected study area had characteristics detectable by the field and remote sensing techniques employed in this study. The active springs had strong water and chlorophyll absorptions that set them apart from the extinct springs. For the extinct spring sites, field VNIR spectroscopy showed featureless spectra, except in vegetated areas, where red edge spectra dominated. Most active springs exhibited bacterial signatures detectable by field VNIR spectroscopy. Field spectra detected unique spectral characteristics of the hyperthermophiles; this provides a basis for understanding how such organisms (most likely in fossil form) might be recognized on Mars.

Upon initial examination, the AVIRIS SWIR reflectance for both the active and extinct springs look similar. However, the extinct springs have a deeper and more distinct 2.25 micron absorption feature than the active springs. Also, the extinct site spectra have a subtle reflectance peak near 2.4 microns that is not observed in the active site spectra. The probable reason for this difference is that extinct sinters are dry and active sinters are generally wet, with water in the active sinter deposits suppressing the reflectance peak.

ASTER VNIR and SWIR spectroscopy for active and extinct sites was similar and could not easily be discriminated. The active sites had a chlorophyll reflectance peak that the extinct sites locally lacked. But, the broad spectral band passes of ASTER, combined with the 15 m and 30 m pixel sizes, made it difficult to discriminate specific materials, and led to the spectral dominance of dry and green vegetation in each pixel. However, the spectra were not pure vegetation. It was evident that there were other materials (i.e. chlorophyll, alteration minerals,

etc.) that increased the reflectance in the visible green and red, but because the spectra were too broad, other materials could not be specifically identified.

Both the ASTER 4/6 and the AVIRIS 139/195 SWIR band ratios proved useful for identifying areas of thermal alteration. Altered rocks always have a alteration ratio greater than unity and all field sites had a ratio greater than unity, suggesting that ASTER and AVIRIS band ratioing techniques can effectively detect altered rocks in these geyser basins. In most cases, the extinct sites had a higher alteration ratio than the active sites, provided those sites were not masked by vegetation.

The ASTER thermal infrared region was useful in detecting thermal anomalies of both active and extinct springs. Emissivity depth of 9.2 micron feature is directly related to silica abundance. On average, the extinct springs contained more silica than the active spring sites. Using ASTER TIR imagery, temperatures over the extinct springs were commonly determined to be higher or the same as the active springs. Probable reasons for this include cooling winds generated over the active sites during eruptions, masking actual surface temperatures. Also, the extinct sites may have different plumbing system geometries than the active sites, allowing more heat to build up, causing higher kinetic temperatures.

Active and extinct springs have differences detectable by remote sensing. Techniques that proved to be useful in this discrimination included field VNIR spectroscopy, AVIRIS SWIR reflectance, ASTER and AVIRIS band ratioing, and ASTER TIR imagery, including emissivity and temperature. In the VNIR, the active sites had detectable microbes and pronounced water and chlorophyll absorptions that the extinct sites lacked. The extinct sites had flat, featureless spectra in the VNIR. In the SWIR, the extinct field sites have a deeper 2.25 micron feature than the active sites, and a 2.4 micron feature that the active sites lacked. The extinct field sites

generally had a higher alteration ratio than the active sites. The emissivity of the 9.2 micron feature is deeper in the extinct sites than the active sites, indicating a higher silica abundance for the extinct sites. Thermal anomalies of active and extinct springs were identified using ASTER TIR imagery. If active or extinct hydrothermal systems exist on Mars on a scale similar to or larger than Yellowstone's springs, THEMIS should be able to identify them, providing complications, such as the eolian dust mantle, are limited.

The classification techniques employed in this study included unsupervised classifications, a supervised classification, and spectral angle mapper. The unsupervised classification techniques roughly identified the extent of thermal alteration in each basin, but could not identify individual hot springs or determine differences between active and extinct areas. The supervised classification more clearly defined the boundaries of the hot spring areas, but still could not delineate between active and extinct springs. Spectral angle mapper appears to be the best of the three classification techniques. It was able to detect spectral differences in individual hot springs, and especially for thermal areas with various mineralogical deposits and thermal features, such as the Fountain Paint Pots. Because classes commonly overlapped using all three techniques, classifications should only be used as a rough estimate of ground coverage types and should be used in conjunction with more accurate methods of identification, such as spectroscopy.

## **Section 6: Application to Mars**

There are several possible sites on Mars designated as areas of past (or present) hydrothermal activity [Bulmer and Gregg, 1998; Dohm et al. 2000; Farmer, 1998; Gulick, 1998, Nelson et al., 1999]. Indirect evidence of near-surface water includes the region surrounding Apollinaris Patera (90S 186W), an ancient Martian volcano, located in the Elysium Basin-Terra Cimmeria region [Farmer, 2000]. The chaos features and outflow channels are abundant near the volcano base and could have formed by subsurface cryosphere melting [Farmer, 2000]. The proximity of the chaotic features to the volcano suggest the possibility of prolonged hydrothermal activity [Farmer, 1996, 2000]. Potential direct evidence of near-surface water has also been recently detected with the Gamma Ray Spectrometer also onboard the Mars Odyssey spacecraft [Boynton et al., 2002].

The Thermal Emission Spectrometer (TES) instrument onboard the Mars Global Surveyor (MGS) detected a large specular (coarse-grained) gray hematite deposit at Sinus Meridiani [Christensen et al., 2000b]. Because this type of hematite is thought to have formed by aqueous precipitation at high temperatures, its discovery may be evidence that hydrothermal systems could have operated on Mars in the recent past [Christensen et al., 2000b; Farmer, 2000]. Coarse-grained hematite is generally found in volcanic regions, i.e. the Yellowstone hydrothermal system, and forms as hot water percolates through iron-bearing rocks [Christensen et al., 2000b]. As the water cools, the iron dissolves and precipitates in cracks and veins of the surrounding rock. The gray hematite can also form as large amounts of iron are dissolved in large bodies of water [Christensen et al., 2000b]. Figure 19 shows the concentration of hematite

as measured by TES. The abundance of hematite is shown in red, with the highest concentrations increasing in brightness. The TES data are superimposed on a Viking photomosaic context image. The area of the image measures 1500 km x 1200 km.

The Mars Odyssey is now in a mapping orbit around Mars, and the THEMIS instrument being used to detect mineralization and potential thermal anomalies associated with hydrothermal activity. Targeting these hydrothermal sites is seemingly possible, given the comparatively high (100 m/pixel) spatial resolution of the instrument. A THEMIS VNIR image of Terra Meridiani region is shown in Figure 20. This area lies at eastern boundary of the hematite unit (1.471 N, 359.468 W). The variations of brightness and texture of the surface seen in this image can be attributed to different rock layers. Numerous layers exposed across the surface may indicate extensive volcanic and sedimentary deposition, followed by erosion. The 19 km diameter crater located in the southern portion (bottom) of the image shows distinct layering, which may be sedimentary in origin. The THEMIS infrared images of this area show different temperatures within many of these rock layers, indicating varying physical properties in each layer. The temperature differences suggest temporal variations in environmental conditions as these layers were deposited or solidified [<http://themis.la.asu.edu/>].

Thus far, the hematite site (2.07S, 6.07W) has been designated as the prime landing site candidate for the 2003 Mars Exploration Rover (MER) missions [Grant, 2002]. MER will have two identical rovers going to two different sites. The rovers will contain a mast mounted remote sensing package, consisting of a panoramic camera (Pancam) for stereoscopic and color imaging, and the mini-TES instrument, as well as arm-based instruments, including a Mössbauer spectrometer and a rock abrasion tool, to expose fresh rock surfaces (Table 12) [Seelos, 2002]. Pancam can view the surface around the rover using two high resolution cameras and can help

determine what rocks and soils to analyze in detail and what samples to acquire. The Mössbauer spectrometer can determine the composition and abundance of iron-bearing minerals with low detection limits. Mössbauer can detect Fe carbonates, sulfates, and nitrates, and determine the oxidation state of Fe minerals, which may give information about early environmental conditions. Mössbauer can also identify hydrothermal iron minerals and nanophase iron that could preserve biological materials [Wade et al., 1999].

The second and third potential sites for the MER 2003 mission include Gusev Crater (14.82S, 184.85W) and Isidis Planitia (4.31 N, 271.97 W), respectively. Melas Chasma (8.88 S, 77.48 W) was considered, but has recently been dismissed because of high winds and steep slopes. Melas Chasma is a small section of the larger 4000 km Valles Marineris canyon, and its floor shows diversity in textures and properties. The mesas at Melas Chasma are slightly rougher than some other proposed sites, and because it is at the bottom of a canyon, high winds could hinder airbag deployment. The backup site is Athabasca Vallis (Elysium Planitia; 8.92 N, 205.21 W). The second backup site was Eos Chasma (13.34 S, 41.39 W), but that has recently been decided against as well, because of similar reasons to Melas Chasma. Figure 21 provides a location map for the proposed sites.

These sites were selected because they all seem to be modified by water at some point in their history. Figure 22 evaluates the criteria for these potential landing sites. For the hematite site, the hydrothermal deposits are thought to be located in the ejecta blanket of a 19 km crater (near 2S, 6W) [Newsom et al., 2003]. Gusev Crater is approximately 150 km in diameter and is believed to be the site of an ancient lake. There are features within the crater that suggest water has flowed in and out of the area, leaving sediments behind. In Gusev crater, the hydrothermal deposits are thought to be located on the rim of Thyra and in fluvial deposits [Newsom et al.,

2003]. Isidis Planitia is an ancient and broad flat plain overlying the boundary between the Martian highlands and plains. The floor exhibits chains of pitted ridges, numerous smaller impact craters, light toned ripples and small dunes. There are many small channels and valleys throughout the area. In Isidis Planitia, the hydrothermal deposits may be located in fluvial deposits [Newsom et al., 2003]. Athabasca Vallis is an extremely young outflow channel with recent volcanic activity.

However, there are some drawbacks to the proposed sites. A downside for the hematite site is that it may be too cold, posing a problem for rover longevity. The site is deemed good for landing however, because its surface is relatively smooth. Gusev crater appears to have high eolian activity containing large quantities of dust, evidenced by dust devils, which may contaminate the rover's solar panels and cover up the underlying surface. TES observations indicate that Isidis Planitia appears to contain potentially hazardous rocks that may cut into the landing airbags and hinder rover maneuverability. Eos Chasma and Athabasca Vallis also appear to have rough surfaces, indicating trafficability problems.

Siliceous sinter deposits are common constituents of the Lower, Midway, and Upper Geyser Basins of Yellowstone. These deposits have been cited as important targets in the search for an ancient biosphere on Mars [Walter and DesMarais, 1996; Farmer, 2000]. Guidry and Chafetz, 1999 showed microbes are well-preserved in old siliceous sinter deposits in Yellowstone. By studying the reflectance and emissivity spectra of these deposits at the resolution of ASTER, the spectral signatures of these potential terrestrial analogs can be applied to TIR data of Mars in order to detect similar deposits. The ASTER TIR images of the Lower, Midway, and Upper Geyser basin were resolution degraded from 90 m/pixel to the THEMIS 100 m/pixel resolution. This 10 m change was not spatially significant, but shows that thermal

anomalies of the larger individual active and extinct hot springs can still be accurately identified. The ASTER TIR images were also resolution degraded to the TES 3 km/pixel resolution. This change was spatially significant, and the thermal anomalies of the hot springs were could not be accurately identified.

To this date, the only aqueous mineral identified on Mars is hematite. Poor spatial resolution may be a reason why hydrothermal deposits and other sedimentary or aqueous minerals, including carbonates and evaporites, have not yet been located on Mars; improved spatial resolution could lead to the detection of these minerals. Another possibility is that the aqueous mineral deposits could be dust-covered and/or eroded, thereby suppressing or erasing their spectral signatures. Furthermore, there may be a low abundance of aqueous minerals on Mars, but this possibility cannot be favored until more extensive research with newly developed instruments is completed.

Although the thermal areas of Yellowstone contain hematite, such as the Chocolate Pots region of the Gibbon Geyser Basin, hematite is not present in such mass quantities as the hematite region on Mars. In fact the Martian hematite region is larger than any terrestrial hematite deposit known to have originated through hydrothermal activity. This may indicate a significant difference regarding the formation and types of hydrothermal minerals that may be found on Mars. Alternatively, the greater hematite abundance on Mars may be attributed to different scale factors than the Earth. In general, features on Mars are roughly ten times larger compared to Earth, due to lower gravity, crustal stability from lack of plate tectonics, and lower erosion rates than the Earth.

Instrument	Key Parameters	Questions to Address
Pancam	12 bands (0.4- 1.0 $\mu\text{m}$ ) for stereoscopic imaging w. 0.3 mrad IFOV; 9.2 deg x 18.4 deg FOV	Hematite rich dunes on etched substrate? Etched unit exposures show evidence of volcanic emplacement processes?
Mini-TES	Emission spectra (5 - 29 $\mu\text{m}$ , 10 $\text{cm}^{-1}$ res) w. 8 or 20 mrad FOV	Platy hematite in dunes? Mafic mineralogy? Palagonite-like coatings on etched substrate materials?
APXS (Alpha Particle X-ray spectrometer)	$^{244}\text{Cm}$ alpha particle sources and x-ray detectors, 4 cm FOV	Mafic composition? Palagonite-like coatings? Hematite-rich dunes?
Mössbauer Spectrometer	$^{57}\text{Fe}$ spectrometer in backscatter mode; FOV $\sim 1.5 \text{ cm}^2$ .	Hematite present in dunes? Other Fe-bearing alteration phases? Mafic minerals present? Evidence of palagonite-like coatings?
MI: Microscopic Imager	30 $\mu\text{m}$ /pixel monochromatic imager (1024x1024) w. 6mm field depth	Platy hematite? Coated grains? Volcanic origins?
RAT: Rock Abrasion Tool	Tool capable of preparing 5 mm deep x 4.5 cm wide surface on rx	Remove coatings/observe fresh igneous minerals?

**Table 12** Planned instruments for the MER 2003 Mars mission (Seelos, 2002).

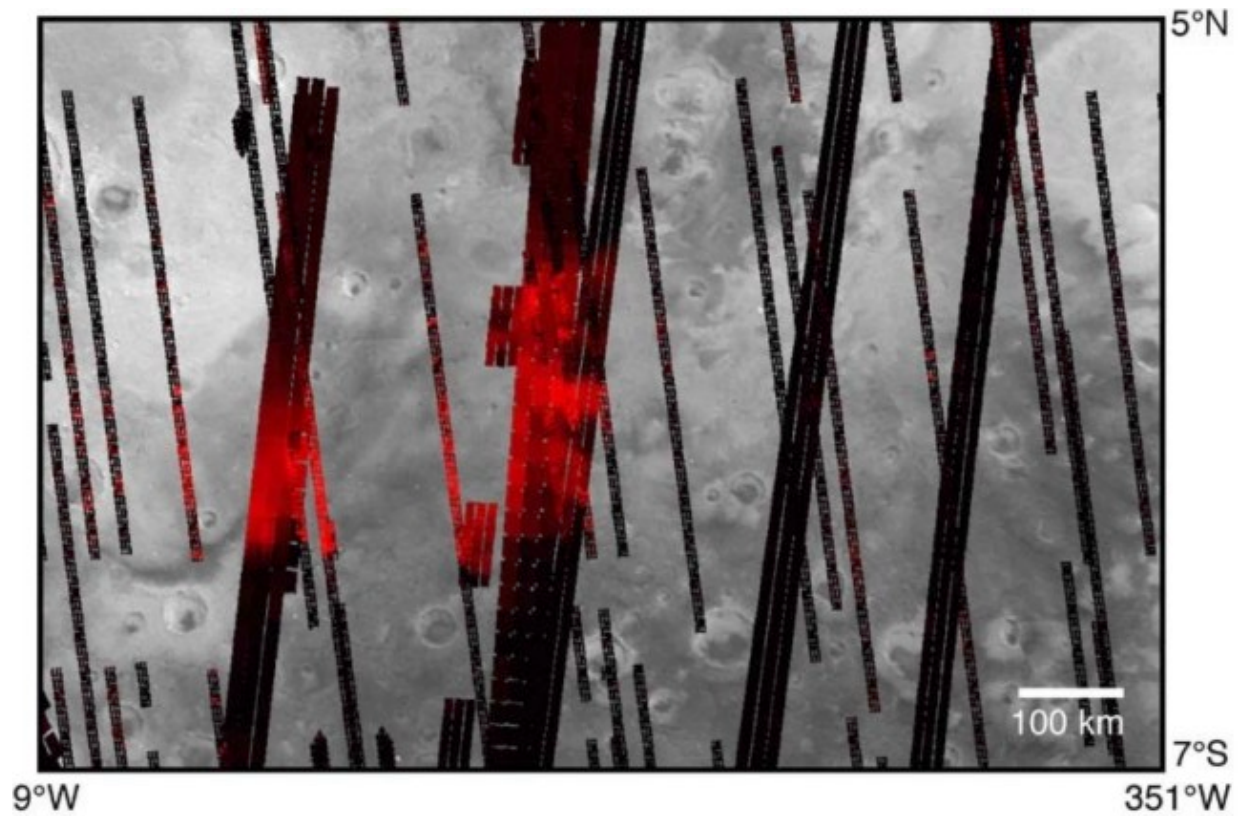


**Figure 19** Concentration of hematite in the Sinus Meridiani region of Mars, as measured by the TES instrument. Hematite concentration is shown in red. Black areas indicate no detected hematite. The context image is a Viking orbiter photomosaic (modified from Christensen et al., 2000b).

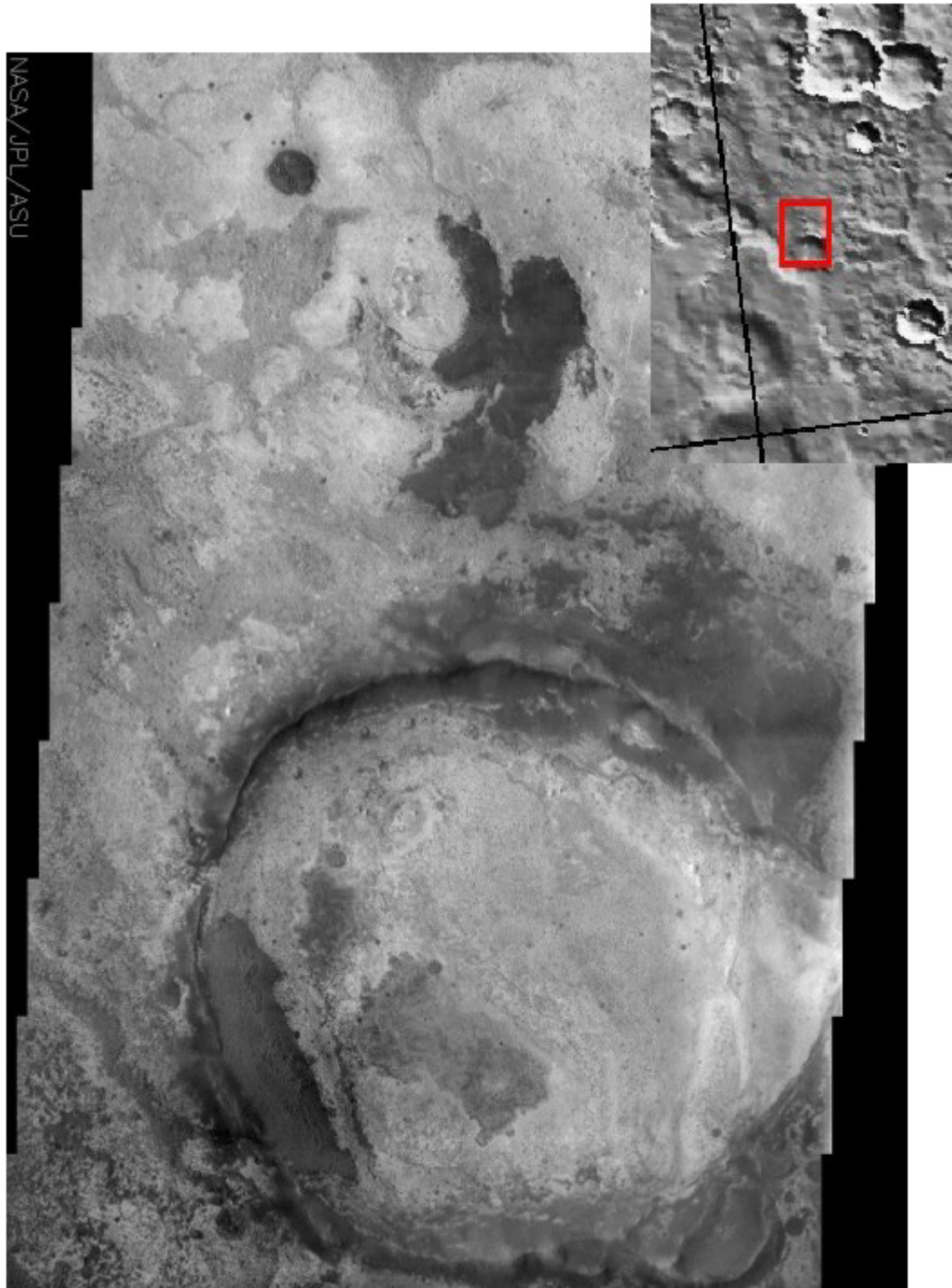


**Figure 20** THEMIS VNIR image of Terra Meridiani, Mars. Context image is shown. Location: 1.471 N, 359.468 W (<http://themis.la.asu.edu>).

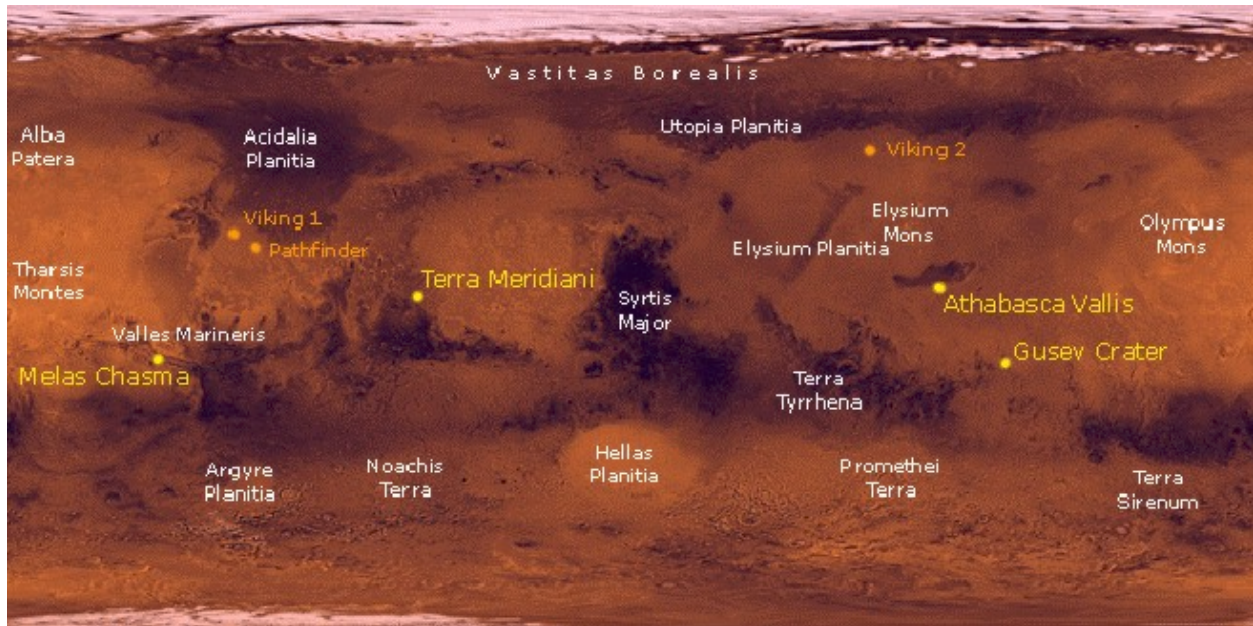


**Figure 21** Location map of the proposed landing sites for 2003 MER. Proposed sites are in yellow. Previous landing sites are located in orange. Other Martian features are in white.

Terra Meridiani (Hematite Site): 2.07S, 6.07W

Gusev Crater: 14.82S, 184.85W

Isidis Planitia (not labeled): 4.31 N, 271.97 W

Backup site: Athabasca Vallis: 8.92 N, 205.21 W

Note: Melas Chasma (8.88 S, 77.48 W) and Eos Chasma (13.34 S, 41.39 W) no longer considered potential sites. (The Planetary Society, 2001).

## Summary MER Landing Site Ranking Criteria

<u>Major Questions/Criteria:</u>	<u>Landing Sites:</u>					
	<i>Hematite</i>	<i>Gusev</i>	<i>Isidis</i>	<i>Melas</i>	<i>Eos</i>	<i>Athabasca</i>
<i>Science Criteria</i>						
Evidence for Water Activity	●	●	●	●	●	●
Address Climate/Geologic History	●	●	●	●	●	●
Preserve Biotic/Prebiotic Materials	●	●	●	●	●	●
Definitive Testing of Hypothesis(es)	●	●	●	●	●	●
Accessible Diversity Within the Site	●	●	●	●	●	●
Site Diversity (for MER's)	●	●	●	●	●	●
Site Diversity (from VL and MPF)	●	●	●	●	●	●
Materials for Athena Analyses	●	●	●	●	●	●
Rock Abundance (pro and con)	●	●	●	●	●	●
Trafficability	●	●	●	●	●	●
Amount of Dust Obscuration	●	●	●	●	●	●
Mission Lifetime	●	●	●	●	●	●
Relief at Scale of Rover Traverse	●	●	●	●	●	●
Potential Useful Earth Analogs	●	●	●	●	●	●
<i>Safety Criteria</i>						
1 km Slope	●	●	●	●	●	●
100 m Slope	●	●	●	●	●	●
10 m Slope	●	●	●	●	●	●
Relief (Craters, Hills)	●	●	●	●	●	●
Rock Abundance/Trafficability	●	●	●	●	●	●
Potentially Hazardous Rocks	●	●	●	●	●	●
Horizontal Winds (Shear/Turbulence)	●	●	●	●	●	●
Horizontal Winds (Sustained Mean)	●	●	●	●	●	●
Vertical Winds	●	●	●	●	●	●
Temperature at Site	●	●	●	●	●	●
Dust	●	●	●	●	●	●
Load Bearing Surface	●	●	●	●	●	●
Elevation	●	●	●	●	●	●
Radex Reflectivity	●	●	●	●	●	●
<i>Public Engagement</i>						
Aesthetics (Views/Relief)	●	●	●	●	●	●
Differs from VL or MPF Sites	●	●	●	●	●	●
Habitability for Life (Past or Present)	●	●	●	●	●	●
Explainable to Public (Good Story)	●	●	●	●	●	●

**Figure 22** Evaluation criteria for the top landing sites for the MER 2003 Mars mission (Grant, 2002). Green = favorable; Yellow = neutral; Red = unfavorable.

## **Section 7: Conclusions**

The Yellowstone volcanic system is the prime terrestrial analogue for Martian studies, as it has characteristics thought to be present on Mars if the planet ever developed hydrothermal systems. Potential similarities include hot spot volcanism, alkaline to neutral hot spring waters, hydrothermal minerals, including siliceous sinter and iron bearing hydrothermal minerals.

A primary goal of this study was to distinguish between active and extinct hot spring areas. These areas were best identified using field-based VNIR spectroscopy, hyperspectral SWIR spectroscopy, including band ratioing, and multispectral TIR emissivities and temperatures. Multispectral VNIR and SWIR spectroscopy could not easily distinguish active and extinct sites because of broad band passes and larger spatial resolutions. Therefore, based upon the work at Yellowstone as an analog to detect hot springs on Mars, rover-based VNIR spectroscopy, hyperspectral SWIR spectroscopy, multispectral TIR emissivities and temperatures would be most useful; multispectral VNIR and SWIR spectroscopy would probably not be as effective. Also, rover-based SWIR and TIR spectroscopy would be advantageous on Mars, although these instruments were not implemented in this study. Classification techniques such as the supervised classification, unsupervised classification, and spectral angle mapper can only be used in conjunction with the more accurate techniques such as band ratioing and spectroscopy. These classification techniques were able to identify the extent of thermal alteration, but could not distinguish between active and extinct hot spring areas.

Although results indicate that remote sensing analysis alone would have been sufficient in analyzing the springs, field studies greatly improved and confirmed the results of this project.

Ground truth procedures are a fundamental constituent of any remote sensing work. The ground-based studies, including photographs and VNIR spectroscopy, single-handedly detected differences in active and extinct springs. Initially, from the airborne and spaceborne remote sensing images alone, only individual hot spring areas could be detected, but it could not be determined whether those areas were active or extinct. Only after extensive image processing, including reflectance calibration and emissivity extraction, differences in the active and extinct springs were then distinguished.

From the airborne AVIRIS and spaceborne ASTER remote sensing images, the extent of thermal alteration at the selected geyser basins was successfully determined. Several key areas were chosen to accomplish field checks and the remote sensing data was analyzed for those areas. The remote sensing data was also analyzed for nearby thermal altered regions.

Yellowstone's main geyser basins comprise a large hydrothermal area, larger than any martian rover can traverse in one mission. Therefore, the procedures implemented in this study will be the same as the procedures implemented in the search for hot springs on Mars. The MER team has pinpointed small, but key landing ellipses. These areas will be field checked with the MER rovers; the THEMIS remote sensing data is being/will be analyzed for these key regions as well as other regions that the rovers cannot field check.

Comprehensive analogue studies such as the one performed here, indicate that the potential hot spring deposits on Mars can be detected and analyzed using the currently available data and remote techniques. As the field-based techniques presented in this study supplemented and validated the ASTER and AVIRIS remote sensing data, MER field studies will be equally essential in validating the results of the Mars Global Surveyor TES and Mars Odyssey THEMIS remote sensing data. ASTER proved successful in discriminating differences in Yellowstone's

active and fossil hydrothermal systems. Therefore THEMIS, a similar instrument to ASTER both spatially and spectrally, should also be able to detect these differences on Mars. MER's mini-  
TES instrument is capable of identifying the basic mineralogy of hydrothermal areas through spectral features caused by silicas, carbonates, and iron oxides, and therefore it can serve as validation for TES and THEMIS results.

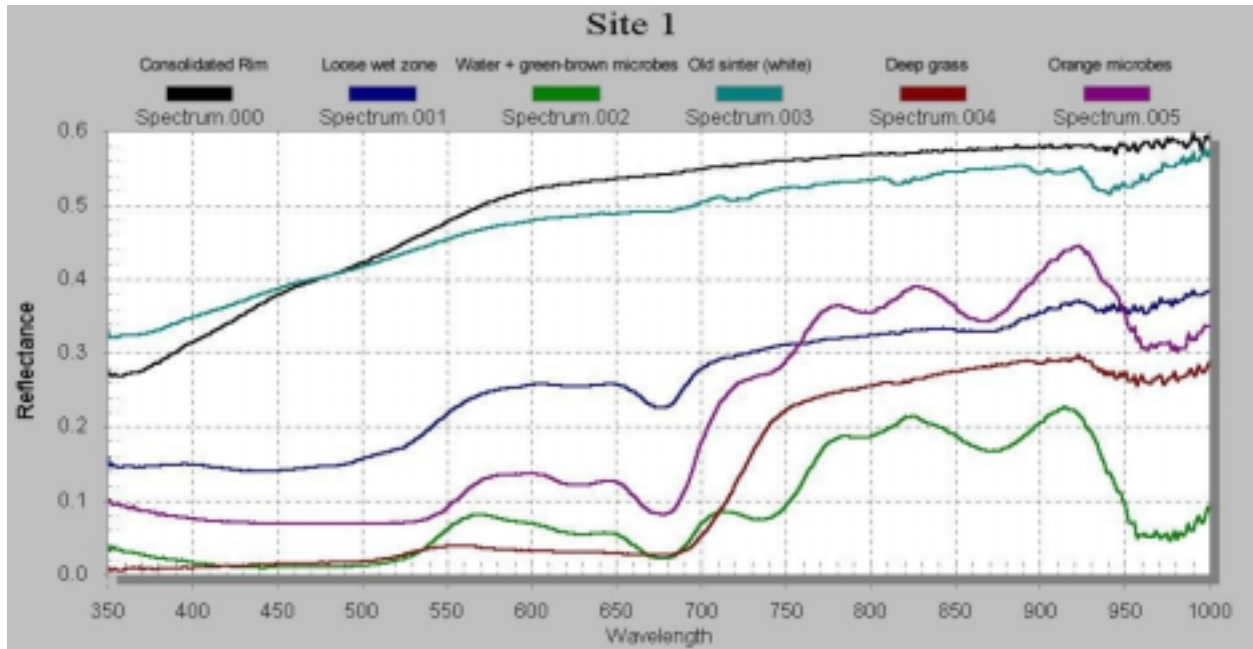
Hyperspectral instruments similar to AVIRIS are being considered for future Mars missions. The NASA Mars Reconnaissance Orbiter (MRO) is scheduled to launch in 2005. MRO will be equipped with a visible stereo imaging camera (HiRISE) having resolution  $< 1$  m and providing images at 6 times higher resolution than existing images. Also included is a hyperspectral VNIR - SWIR spectrometer (CRISM) from  $0.4 - 4.0 \mu\text{m}$  to study surface composition. Primary objectives include the search for evidence of past or present water. Martian hyperspectral data sets will be extremely important for detailed mineralogical studies of potential hydrothermal systems and would greatly benefit our current knowledge of the red planet.

## **APPENDICES**

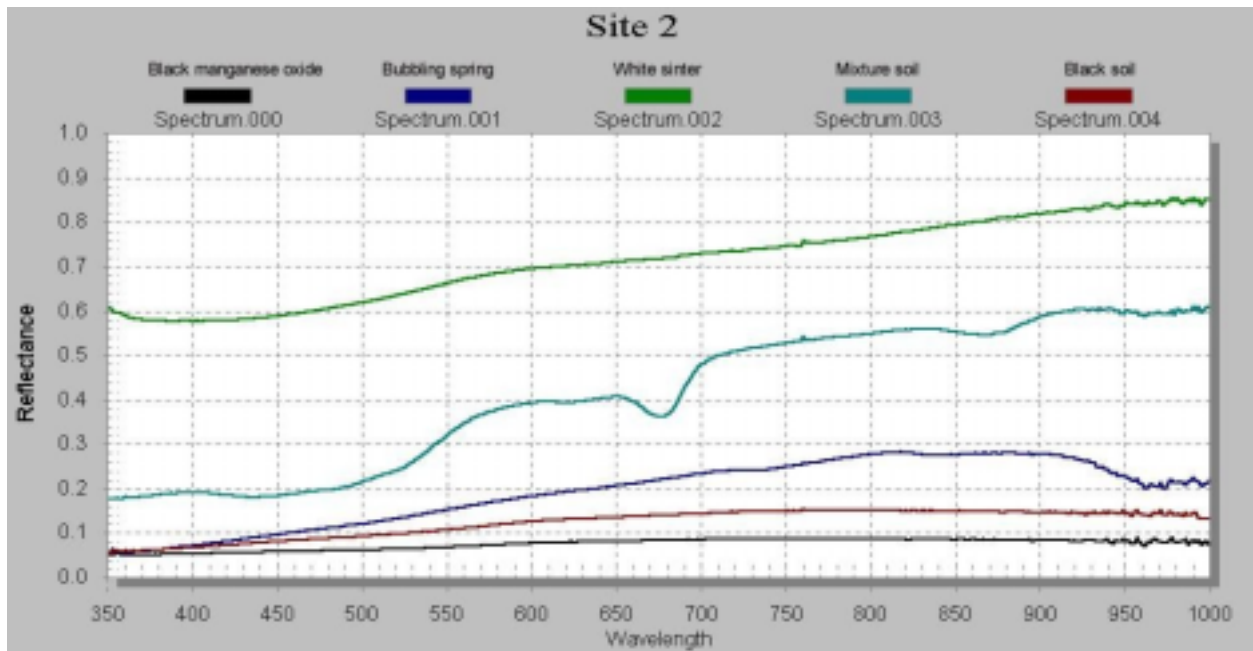
## **Appendix A**

### **Field VNIR Spectra (including GPS coordinates and field radiometric temperatures)**

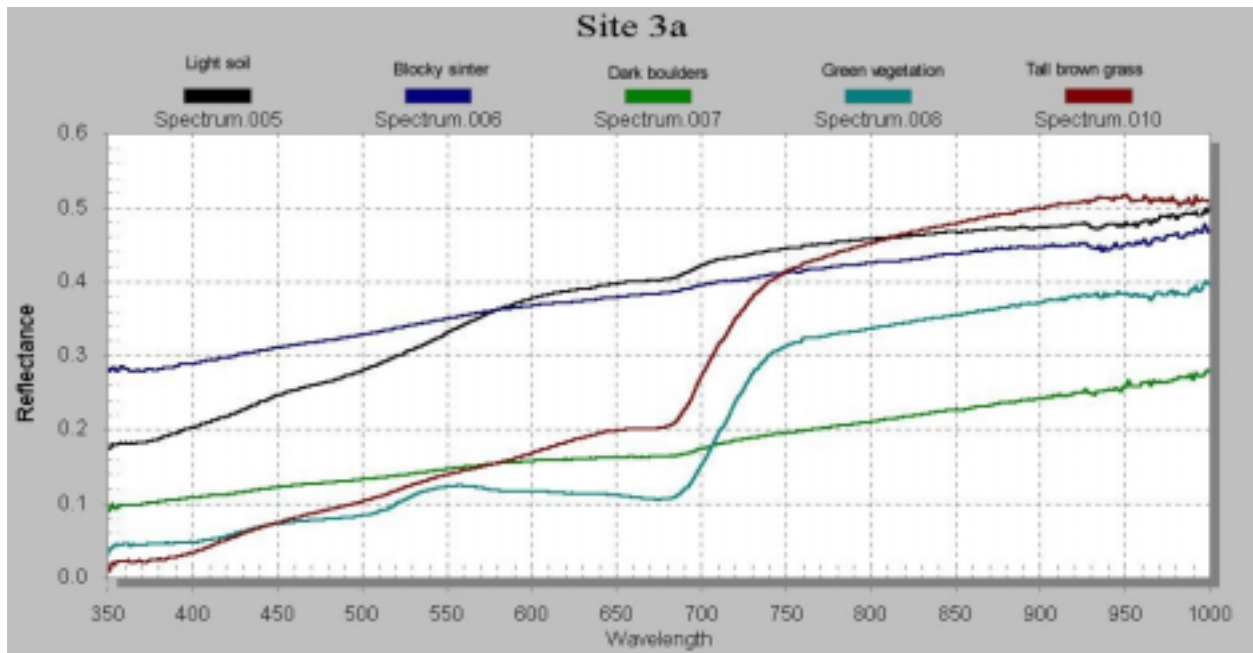
**Note: All field VNIR wavelengths are in nanometers (nm).**



Site 1		
Spectrum	GPS lat (N)/lon (W) (DMS)	Field radiometer (°C)
000 – Consolidated rim	44° 31' 59.10" 110° 47' 49.34"	63.8 – 72.4
001 – Loose wet zone	44° 31' 59.07" 110° 47' 49.36"	-
002 – Water + green-brown microbes	44° 31' 59.07" 110° 47' 49.30"	-
003 – Old sinter (white)	44° 31' 59.23" 110° 47' 49.38"	36.3
004 – Deep grass	44° 31' 58.94" 110° 47' 49.38"	23.1
005 – Orange microbes	44° 31' 58.94" 110° 47' 49.34"	28.5

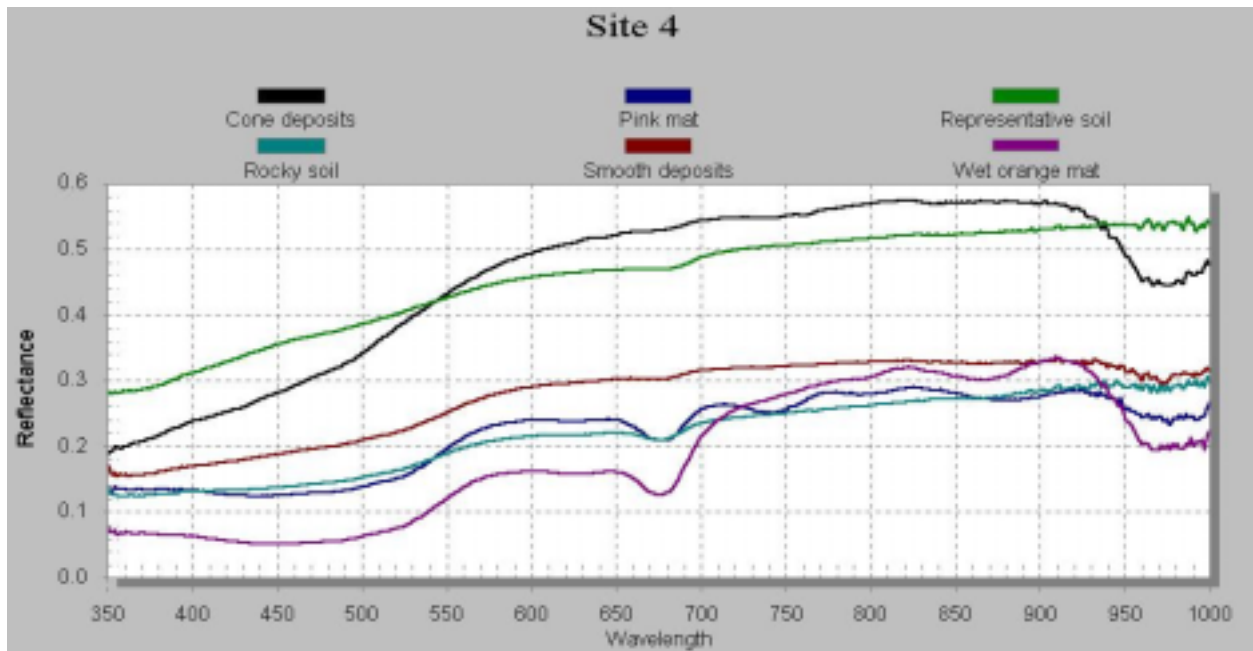


<b>Site 2</b>		
<b>Spectrum</b>	<b>GPS lat (N)/lon (W) (DMS)</b>	<b>Field radiometer (°C)</b>
000 – Black manganese oxide	44° 32' 38.04" 110° 46' 49.72"	82.7
001 – Bubbling spring	44° 32' 38.45" 110° 46' 49.13"	79.4
002 – White sinter	44° 32' 37.42" 110° 46' 47.96"	35.4
003 – Mixed soil	44° 32' 37.71" 110° 46' 48.40"	27.5
004 – Black soil	44° 32' 38.12" 110° 46' 48.41"	41.7



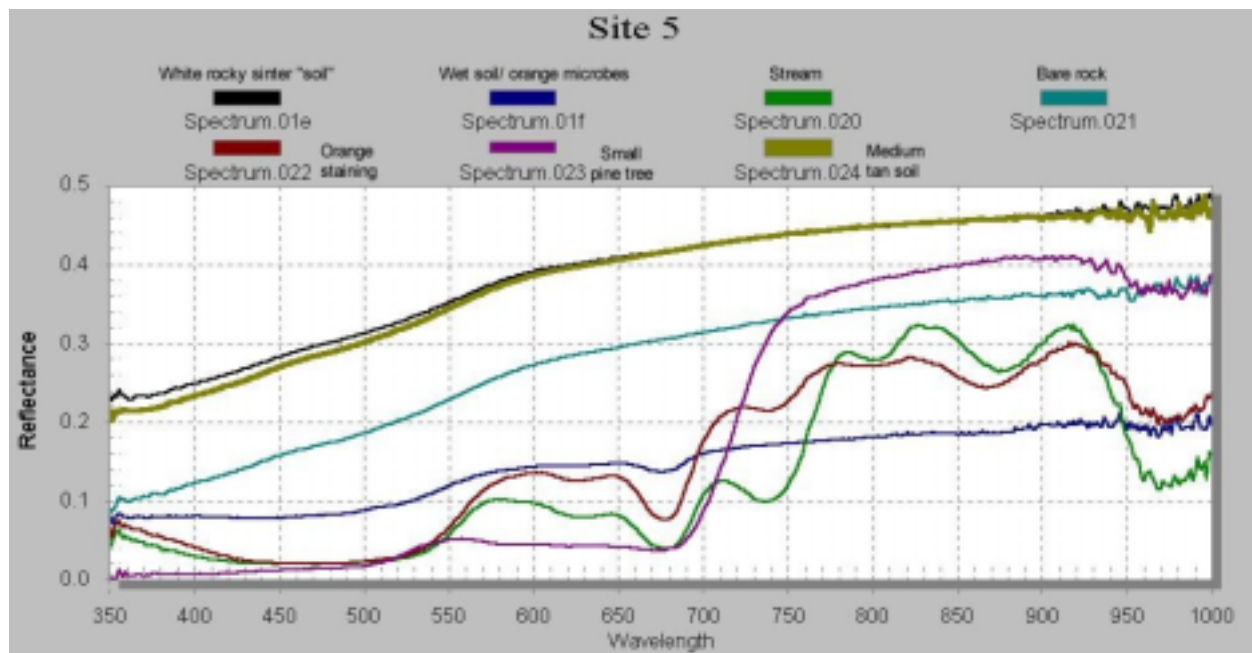
Site 3a	
Spectrum	GPS lat (N)/lon (W) (DMS)
005 – Light soil	Center of The Ruin: 44° 27' 29.92" 110° 49' 57.86"
006 – Blocky sinter	
007 – Dark boulders	
008 – Green vegetation	
010 – Tall brown grass	

Field radiometric measurement for Site 3a: 73.9 °C



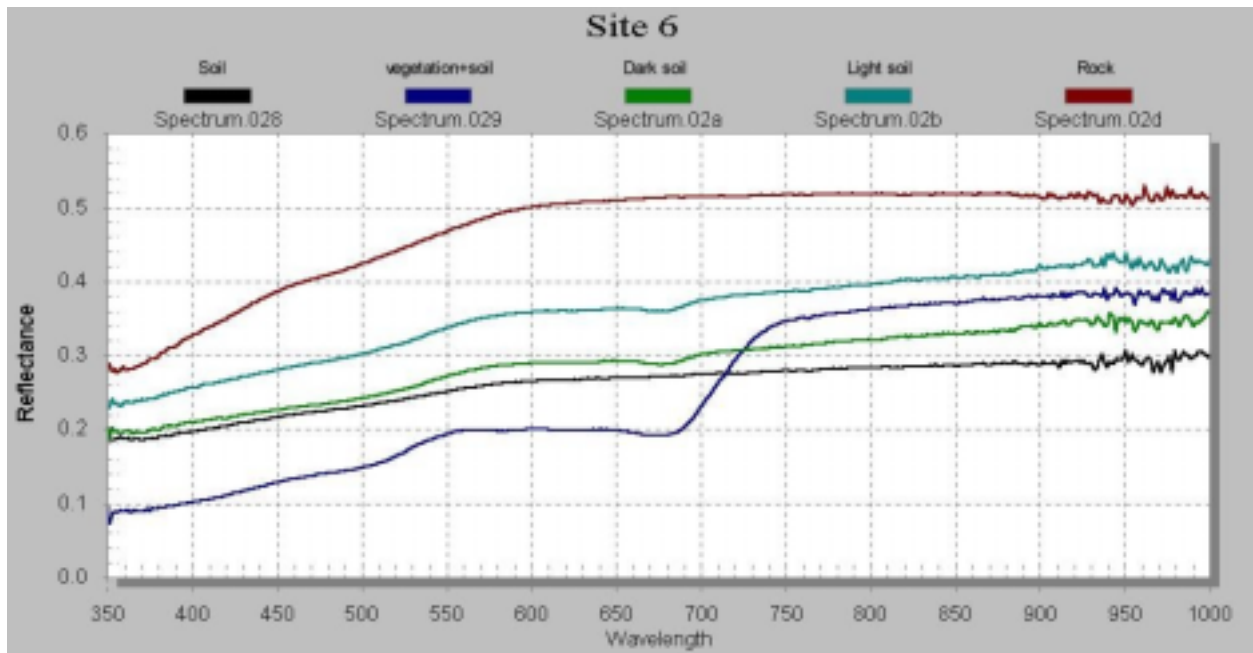
<b>Site 4</b>	
<b>Spectrum</b>	<b>GPS lat (N)/lon (W) (DMS)</b>
Cone deposits	44° 33' 22.95" 110° 49' 55.66"
Pink mat	44° 33' 23.09" 110° 49' 55.97"
Representative soil	44° 33' 22.90" 110° 49' 55.94"
Rocky soil	44° 33' 23.03" 110° 49' 55.75"
Smooth deposits	44° 33' 22.68" 110° 49' 56.29"
Wet orange mat	44° 33' 23.00" 110° 49' 55.79"

Field radiometric measurement for Site 4: Temperature varying in the 88 °C range.

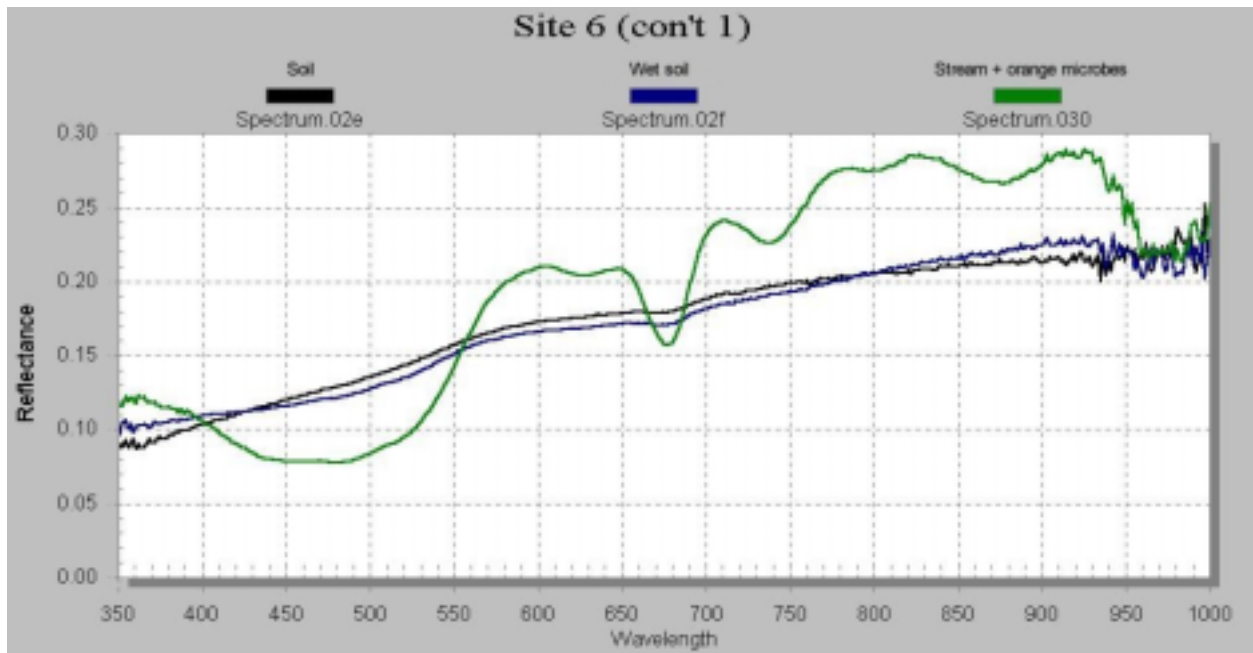


Site 5	
Spectrum	GPS lat (N)/lon (W) (DMS)
01e – White rocky sinter "soil"	44° 31' 8.68" 110° 49' 35.54"
01f – Wet soil/orange microbes	44° 31' 8.70" 110° 49' 35.51"
020 - Stream	Same as Spectrum 01f
021 – Bare rock	44° 31' 8.61" 110° 49' 35.63"
022 – Orange staining	44° 31' 8.51" 110° 49' 35.92"
023 – Small pine tree	44° 31' 8.41" 110° 49' 35.81"
024 – Medium tan soil	-

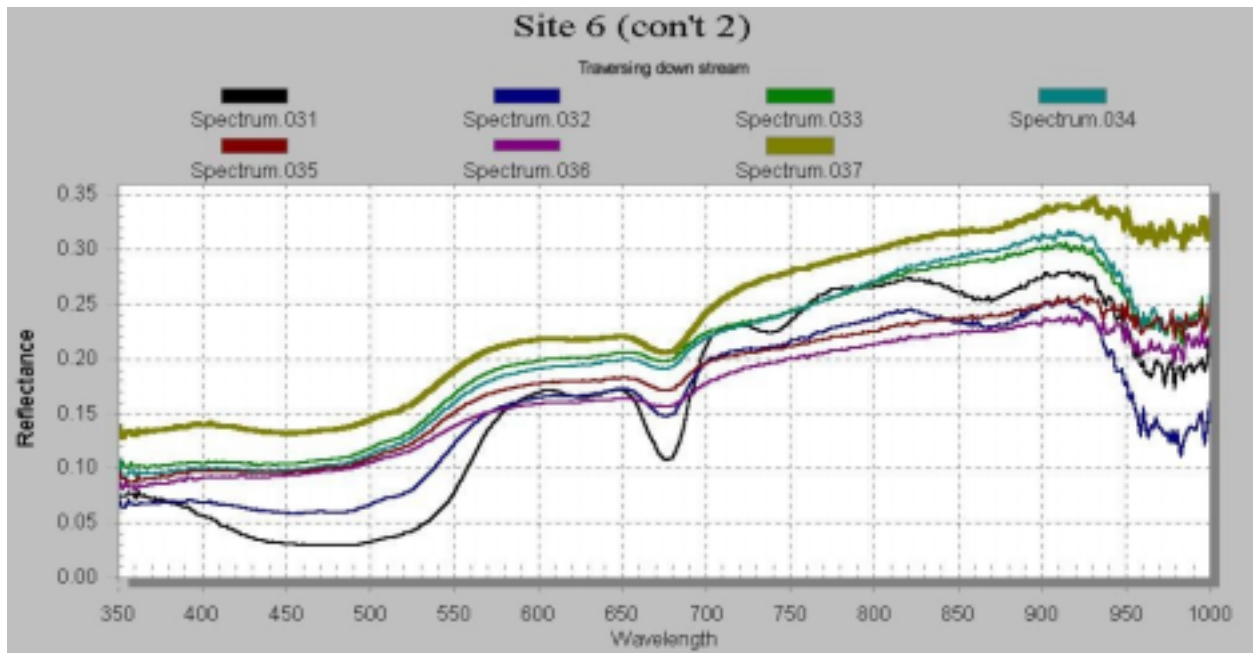
Field radiometric measurement for Site 5: Temperature of stream 55.6 °C (Spectrum 020);  
 Temperature of main geyser (Rabbit Creek Geyser) 83.5 °C.



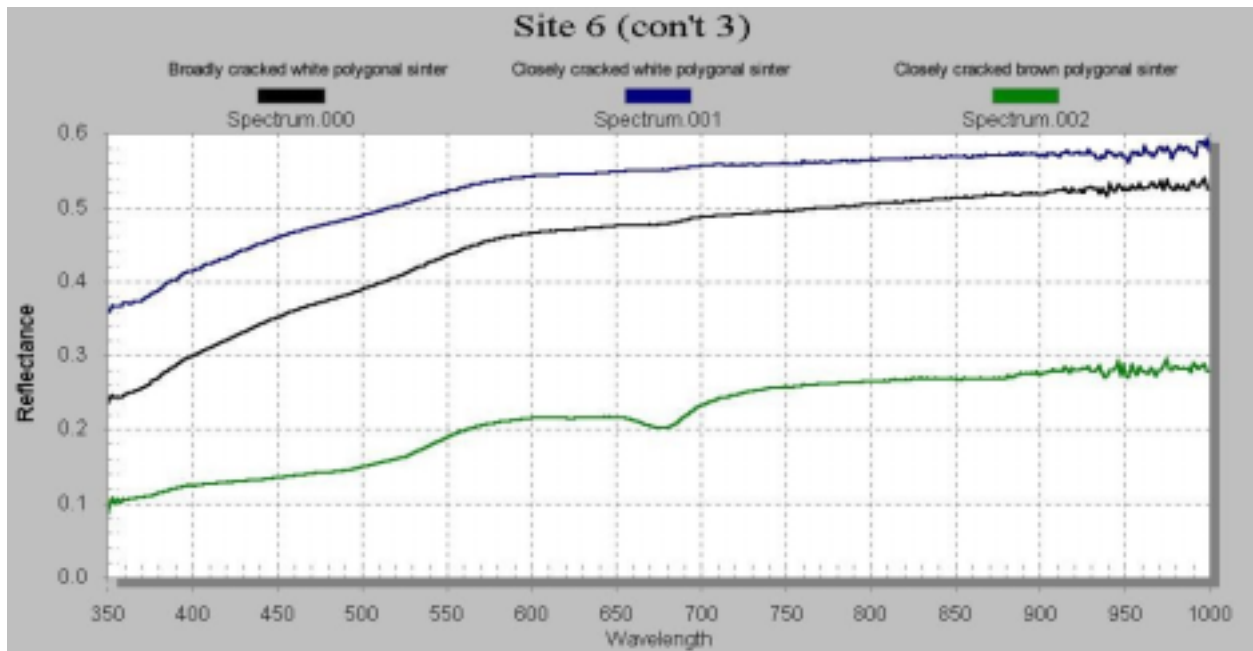
<b>Site 6</b>	
<b>Spectrum</b>	<b>GPS lat (N)/lon (W) (DMS)</b>
028 - Soil	44° 34' 18.47" 110° 49' 29.83"
029 – Vegetation + soil	44° 34' 18.32" 110° 49' 30.07"
02a – Dark soil	44° 34' 18.23" 110° 49' 30.09"
02b – Light soil	-
02d - Rock	44° 34' 17.85" 110° 49' 30.32"



Site 6 (con't 1)	
Spectrum	GPS lat (N)/lon (W) (DMS)
02e - Soil	-
02f - Wet soil	44° 34' 17.53" 110° 49' 29.94"
030 - Stream + orange microbes	-

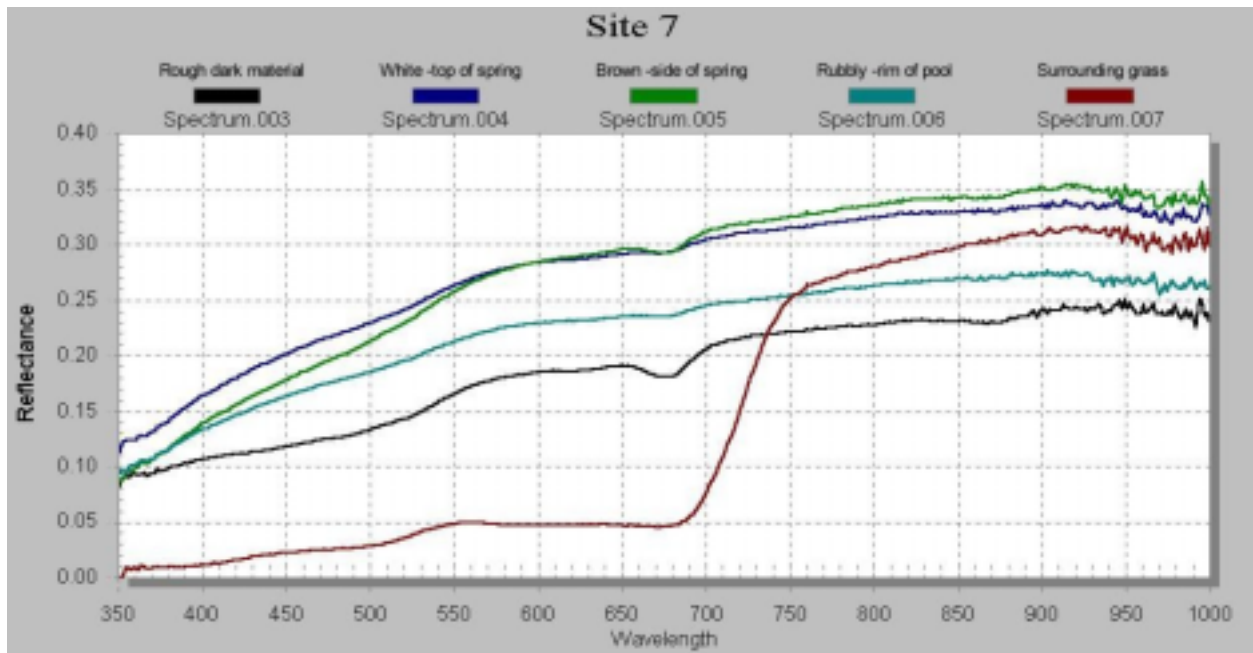


Site 6 (con't 2)	
Spectrum	GPS lat (N)/lon (W) (DMS)
031 – Traversing down stream	-
032 – "	-
033 – "	-
034 – "	-
035 – "	-
036 – "	-
037 – "	-

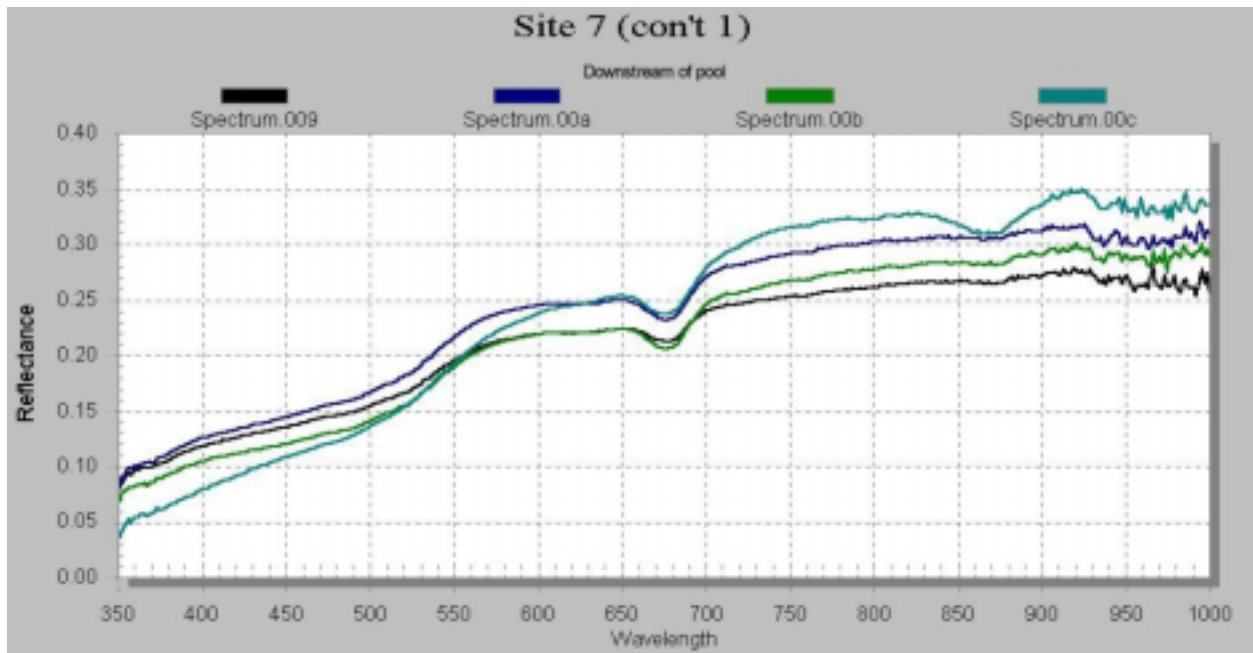


Site 6 (con't 3)	
Spectrum	GPS lat (N)/lon (W) (DMS)
000 – Broadly cracked white polygonal sinter	44° 34' 16.46" 110° 49' 34.24"
001 – Closely cracked white polygonal sinter	44° 34' 16.49" 110° 49' 34.10"
002 – Closely cracked brown polygonal sinter	44° 34' 16.38" 110° 49' 33.92"

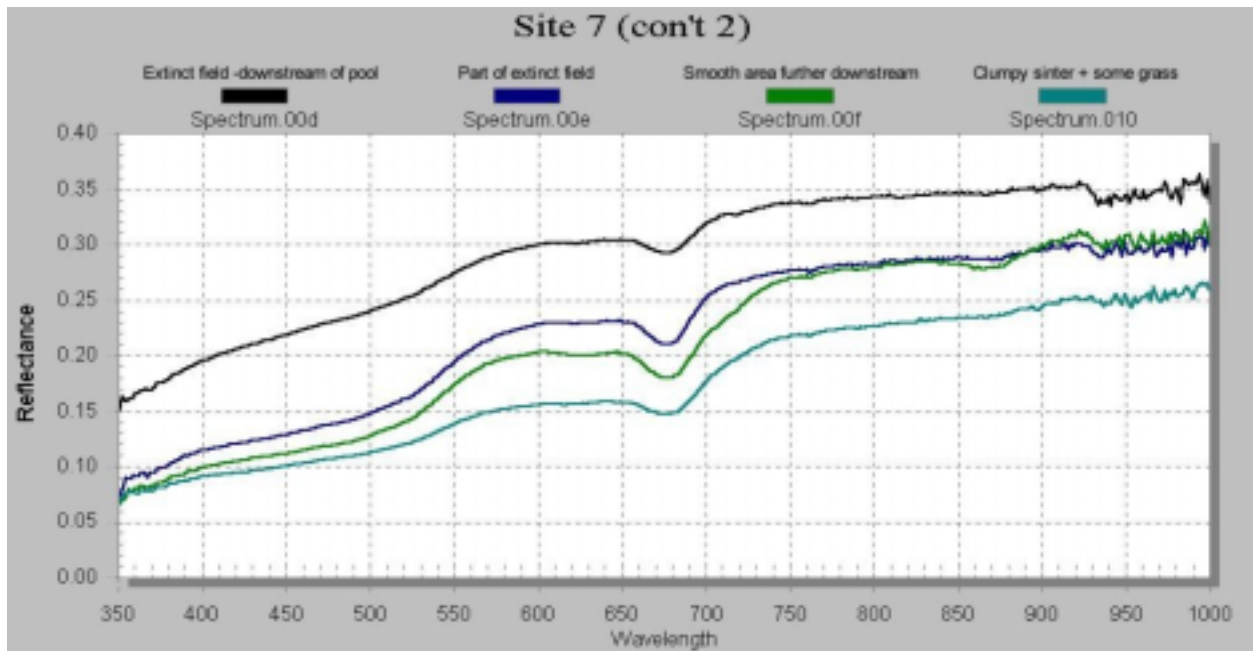
Field radiometric measurement for Site 6: Average temperature of pools 60 °C.



Site 7	
Spectrum	GPS lat (N)/lon (W) (DMS)
003 – Rough dark material	44° 33' 58.95" 110° 49' 4.30"
004 – White – top of spring	
005 – Brown – side of spring	
006 – Rubbly – rim of pool	
007 – Surrounding grass	

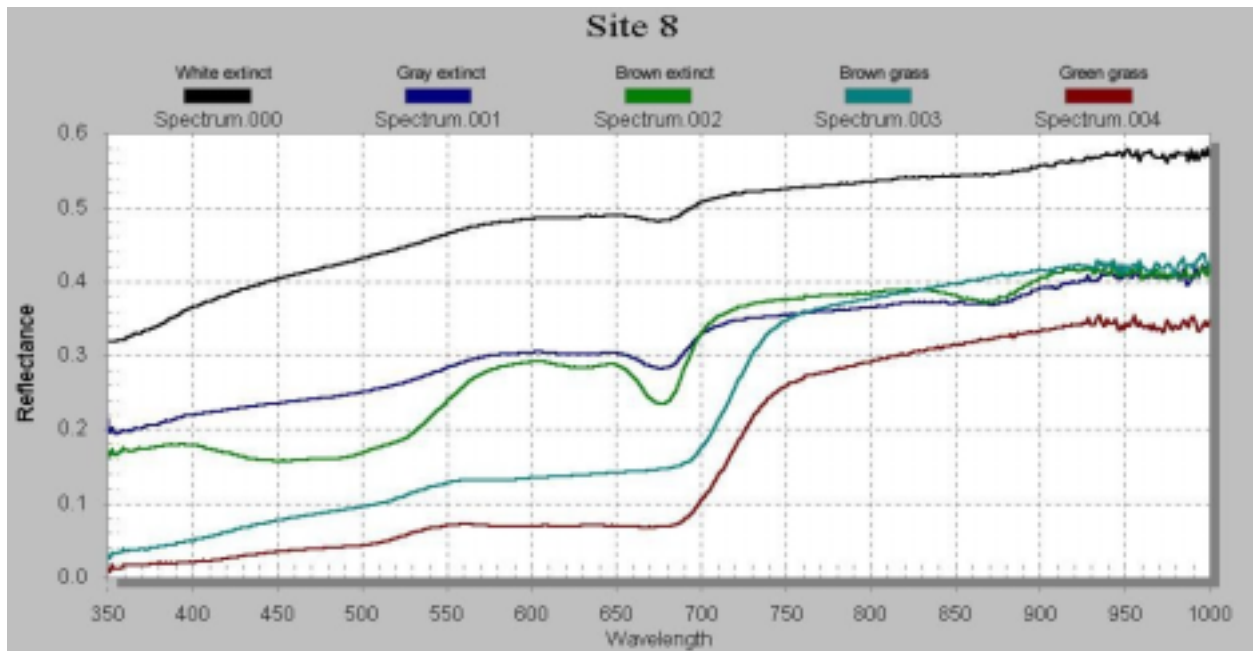


Site 7 (con't 1)	
Spectrum	GPS lat (N)/lon (W) (DMS)
009 – Downstream of pool	44° 27' 59.03"
00a – "	110° 49' 4.26"
00b – "	
00c – "	44° 27' 59.05" 110° 49' 4.18"



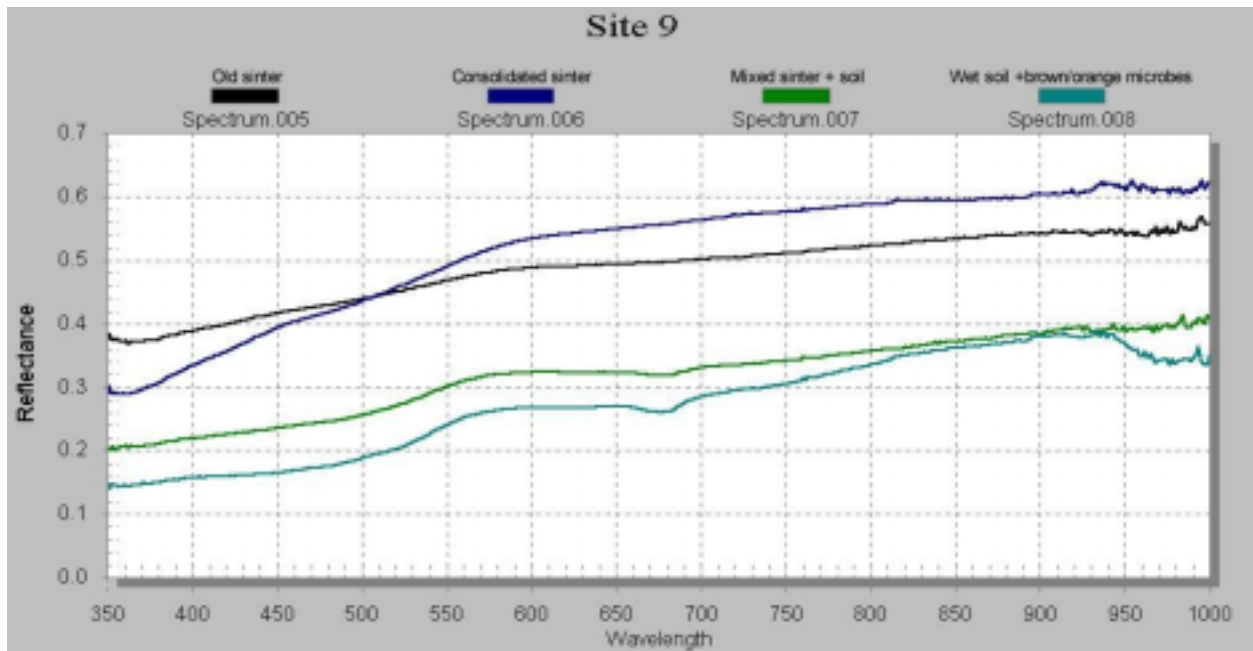
<b>Site 7 (con't 2)</b>	
<b>Spectrum</b>	<b>GPS lat (N)/lon (W) (DMS)</b>
00d – Extinct field – downstream of pool	44° 33' 59.07" 110° 49' 4.09"
00e – Part of extinct field	44° 33' 59.21" 110° 49' 4.05"
00f – Smooth area further downstream	44° 33' 59.32" 110° 49' 4.06"
010 – Clumpy sinter + some grass	44° 33' 59.32" 110° 49' 4.13"

Field radiometric measurement for Site 7: Temperature of extinct sinter 31 °C

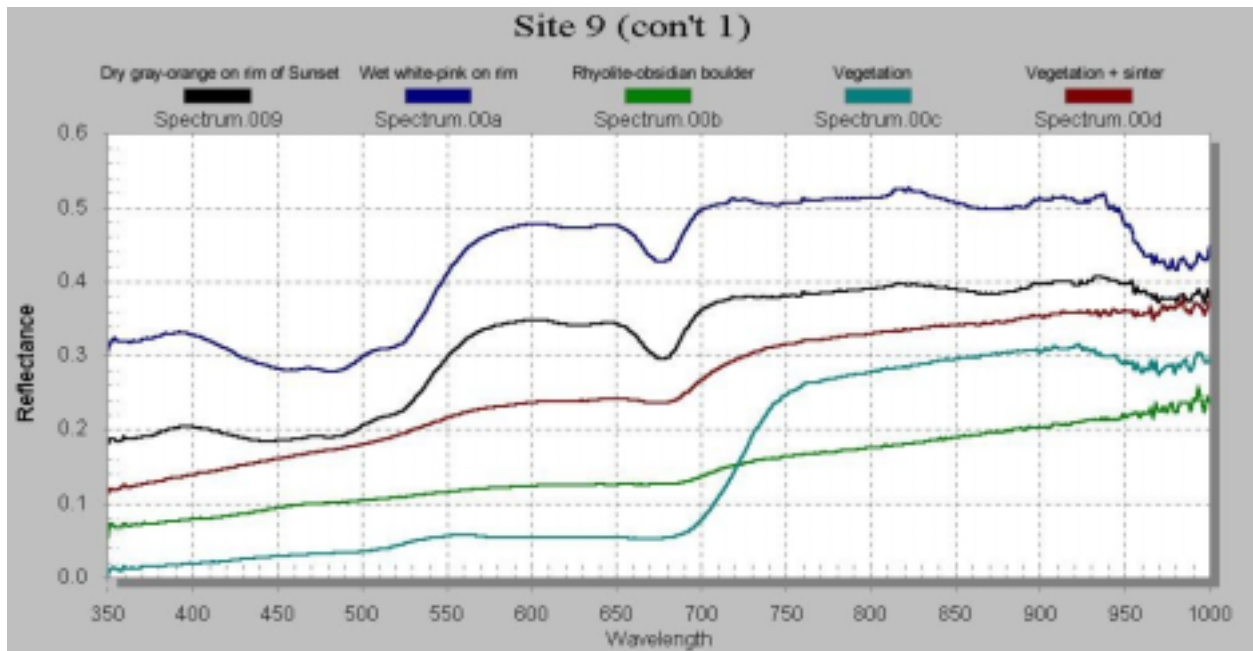


Site 8	
Spectrum	GPS lat (N)/lon (W) (DMS)
000 – White extinct	44° 32' 34.00" 110° 49' 27.30"
001 – Gray extinct	44° 32' 33.85" 110° 49' 27.13"
002 – Brown extinct	44° 32' 33.68" 110° 49' 27.42"
003 – Brown grass	44° 32' 33.80" 110° 49' 27.50"
004 – Green grass	44° 32' 34.41" 110° 49' 27.10"

Field radiometric measurement for Site 8: There is no temperature measurement for Site 8.

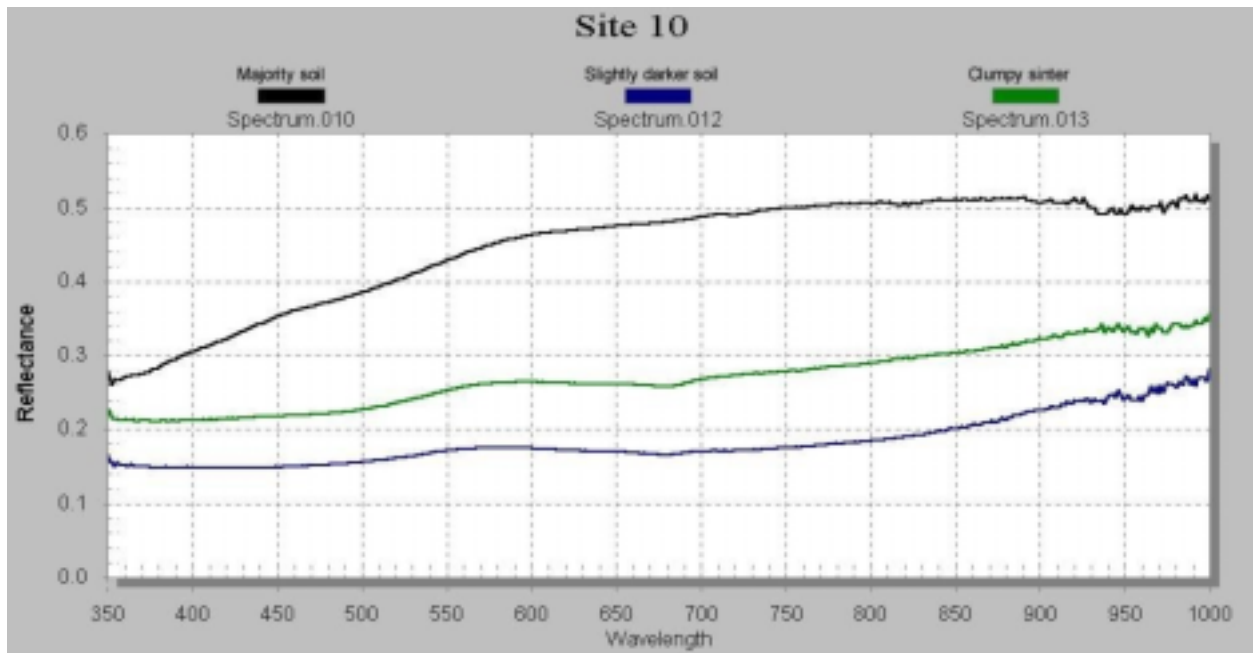


<b>Site 9</b>	
<b>Spectrum</b>	<b>GPS lat (N)/lon (W) (DMS)</b>
005 – Old sinter	44° 27' 46.76" 110° 49' 21.00"
006 – Consolidated sinter	44° 27' 46.25" 110° 49' 19.99"
007 – Mixed sinter + soil	44° 27' 46.30" 110° 49' 18.08"
008 – Wet soil + brown/orange microbes	Approx. same as Spectrum 007

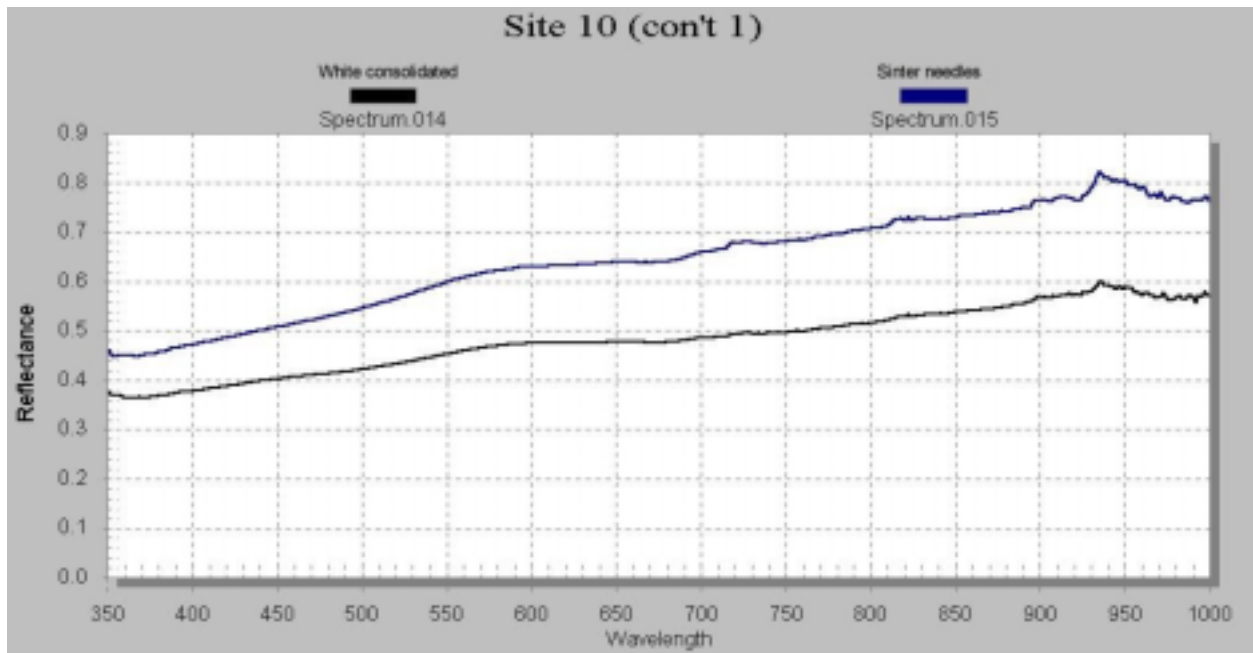


Site 9 (con't 1)	
Spectrum	GPS lat (N)/lon (W) (DMS)
009 – Dry gray orange on rim of Sunset	44° 27' 46.28" 110° 49' 17.80"
00a – Wet white-pink on rim	44° 27' 46.05" 110° 49' 17.78"
00b – Rhyolite-obsidian boulder	44° 27' 45.44" 110° 49' 23.55"
00c – Vegetation	Same as Spectrum 00b
00d – Vegetation + sinter	Same as Spectrum 00b

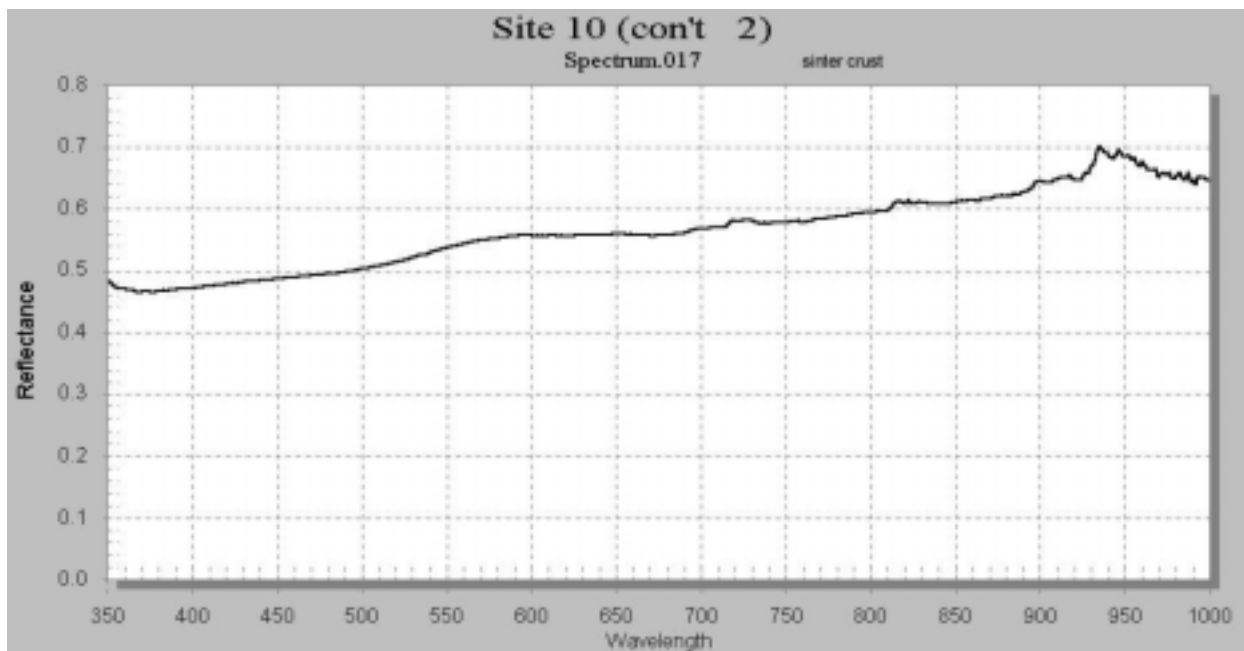
Field radiometric measurement of Site 9: Temperature of Sunset Lake ranges from 37-71 °C.



<b>Site 10</b>	
<b>Spectrum</b>	<b>GPS lat (N)/lon (W) (DMS)</b>
010 – Majority soil	44° 29' 5.02" 110° 49' 20.41"
012 – Slightly darker soil	44° 29' 4.89" 110° 49' 20.36"
013 – Clumpy sinter	44° 29' 4.65" 110° 49' 20.20"

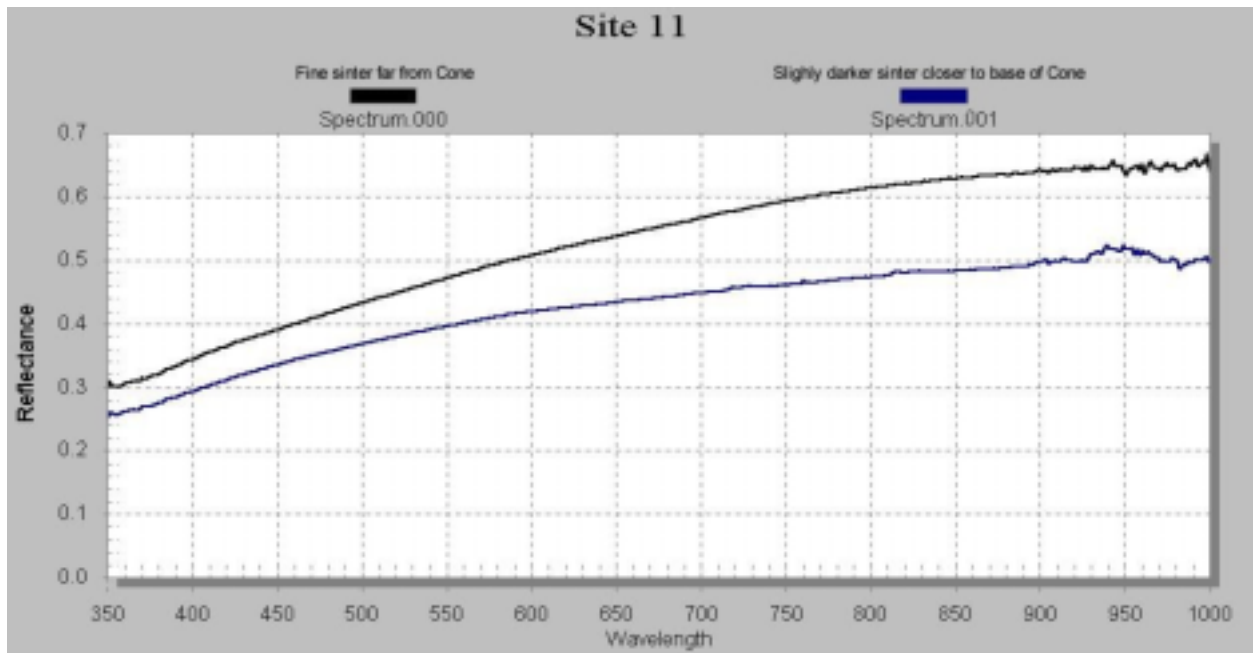


Site 10 (con't 1)	
Spectrum	GPS lat (N)/lon (W) (DMS)
014 – White consolidated	44° 29' 4.53" 110° 49' 20.15"
015 – Sinter needles	44° 29' 4.42" 110° 49' 20.15"

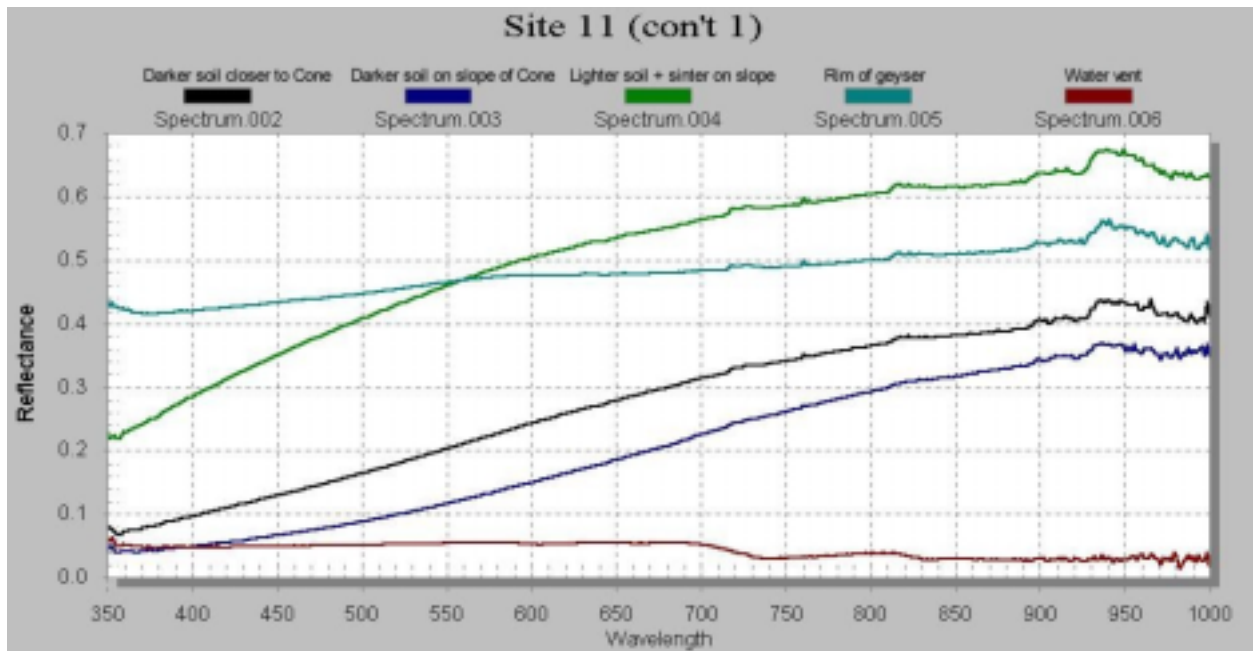


Site 10 (con't 2)	
Spectrum	GPS lat (N)/lon (W) (DMS)
017 – Sinter crust	44° 29' 4.33" 110° 49' 19.92"

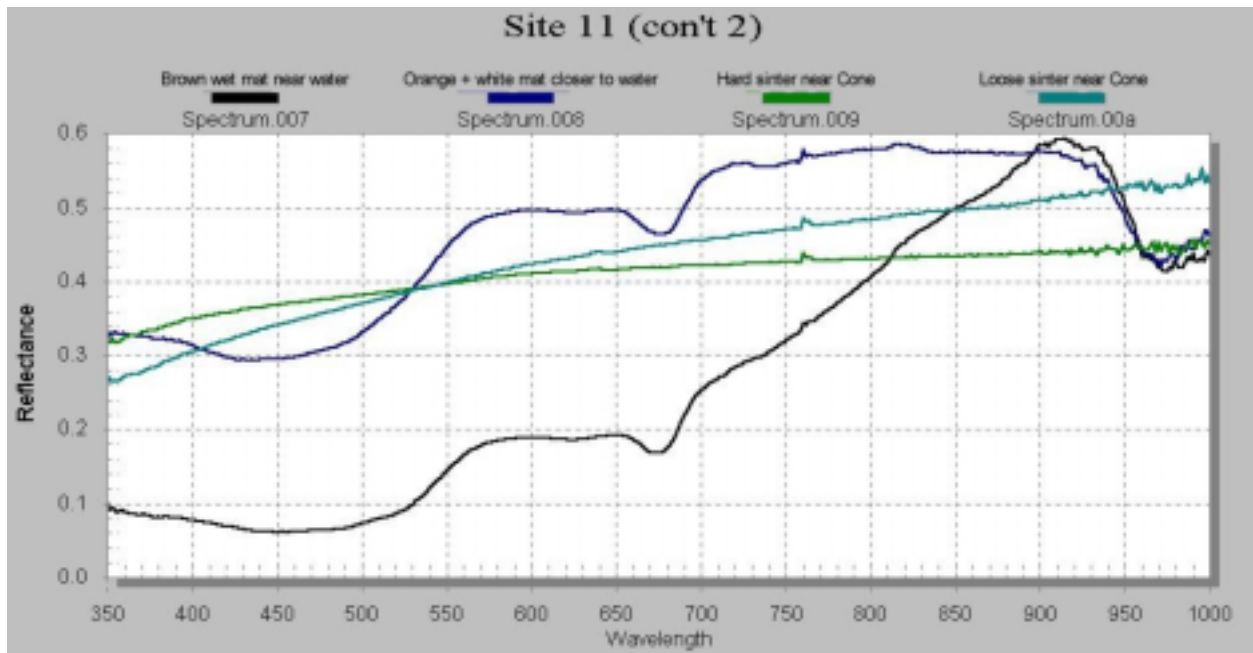
Field radiometric measurement of Site 10: Runoff channels of Sapphire Pool 73.5 °C



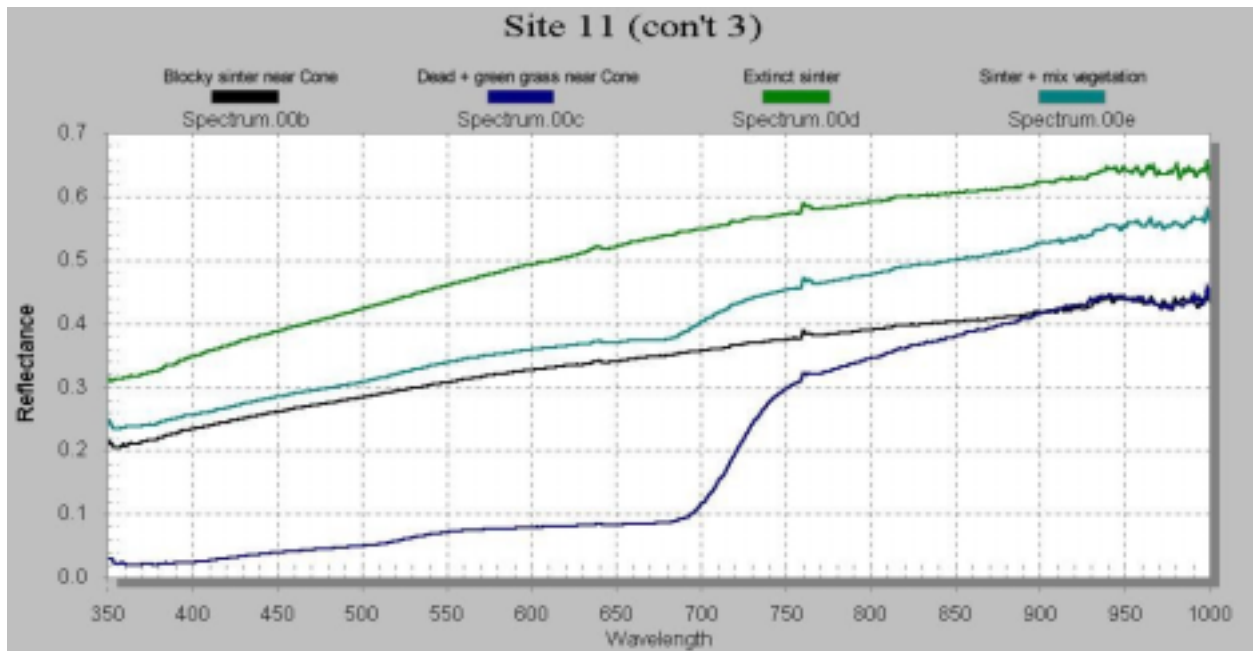
Site 11: Bend Cone Geyser	
Spectrum	GPS lat (N)/lon (W) (DMS)
000 – Fine sinter further from Bend Cone	44° 27' 37.67" 110° 49' 18.60"
001 – Slightly darker sinter closer to base of cone	44° 27' 37.41" 110° 49' 18.54"



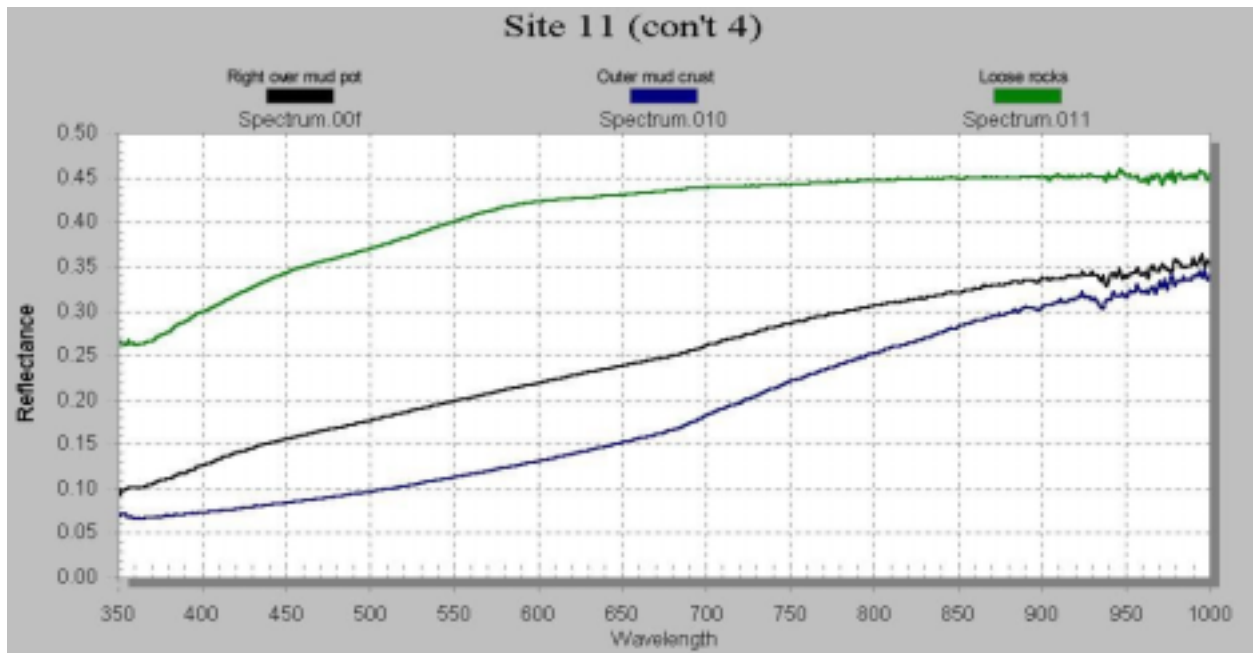
<b>Site 11 (con't 1): Bend Cone Geyser (con't)</b>	
<b>Spectrum</b>	<b>GPS lat (N)/lon (W) (DMS)</b>
002 – Darker soil closer to cone	44° 27' 37.27" 110° 49' 18.51"
003 – Darker soil on slope of cone	44° 27' 37.21" 110° 49' 18.75"
004 – Lighter soil + sinter on slope	44° 27' 37.14" 110° 49' 18.85"
005 – Rim of geyser	44° 27' 37.22"
006 – Water vent	110° 49' 18.88"



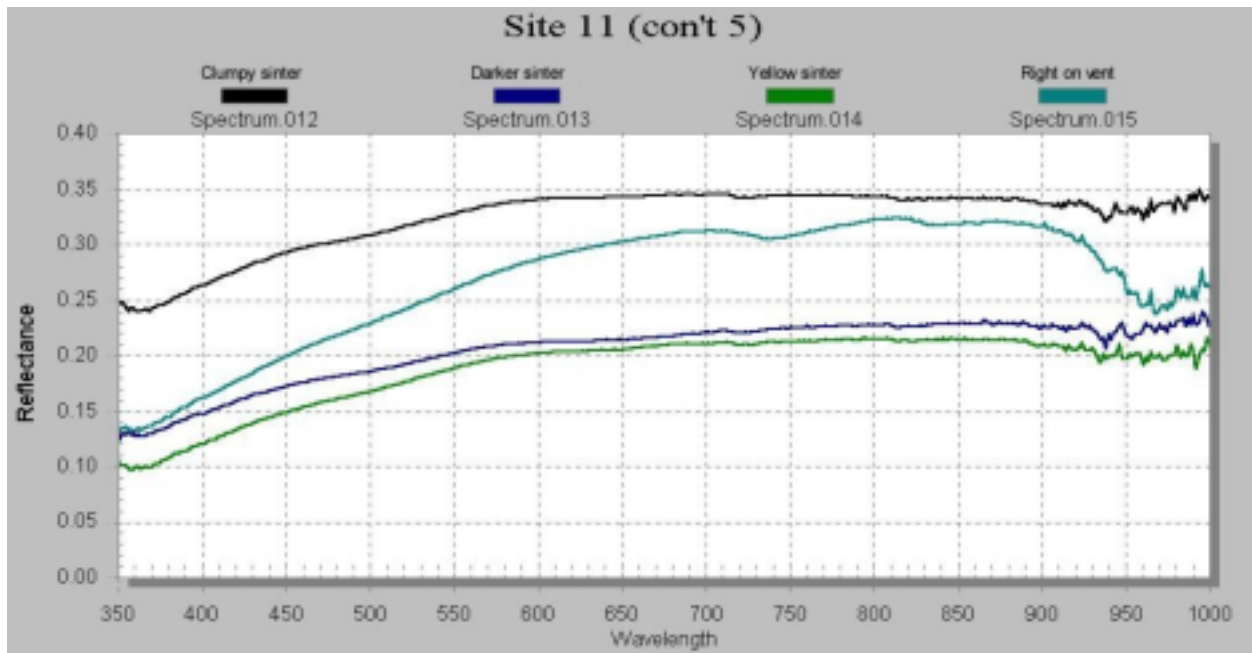
<b>Site 11 (con't 2): Bend Cone Geyser (con't)</b>	
<b>Spectrum</b>	<b>GPS lat (N)/lon (W) (DMS)</b>
007 – Brown wet mat near water	44° 27' 37.20" 110° 49' 18.96"
008 – Orange + white mat near water	44° 27' 37.23" 110° 49' 18.95"
009 – Hard sinter near cone	44° 27' 37.58" 110° 49' 18.65"
00a – Loose sinter near cone	44° 27' 37.53" 110° 49' 19.90"



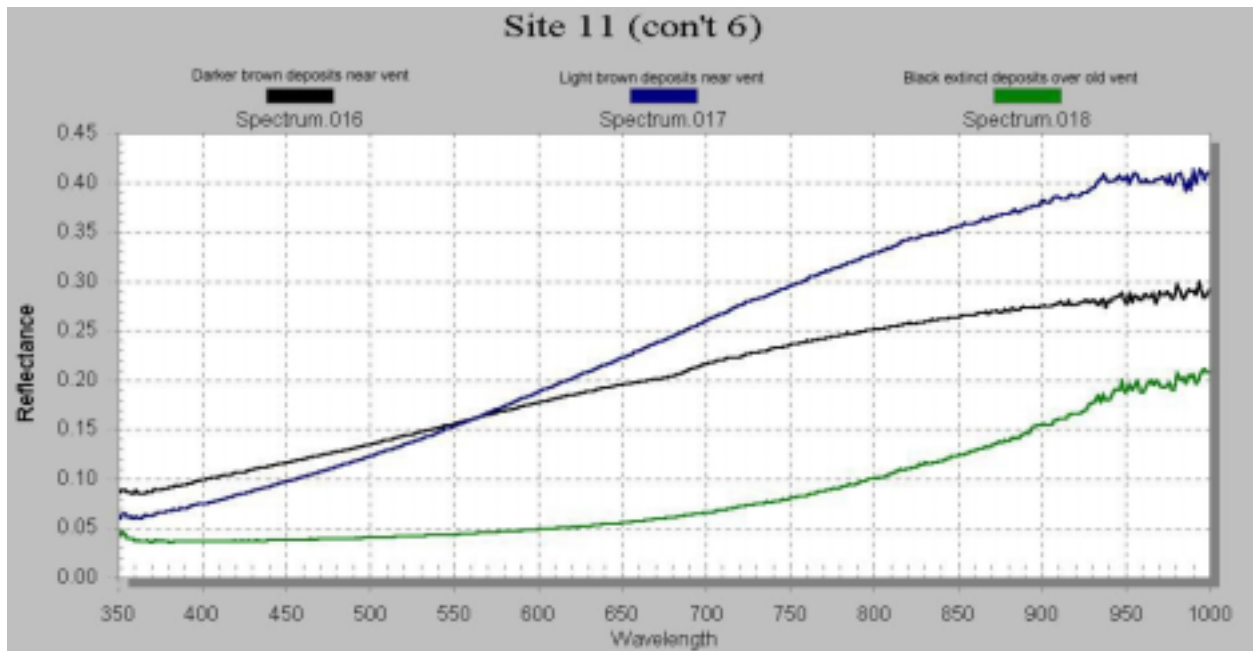
<b>Site 11 (con't 3): Bend Cone Geyser (con't)</b>	
<b>Spectrum</b>	<b>GPS lat (N)/lon (W) (DMS)</b>
00b – Blocky sinter near cone	44° 27' 37.15" 110° 49' 20.19"
00c – Dead + green grass near cone	44° 27' 37.00" 110° 49' 20.48"
00d – Extinct sinter	44° 27' 37.25" 110° 49' 21.04"
00e – Sinter + mix vegetation	44° 27' 37.36" 110° 49' 21.28"



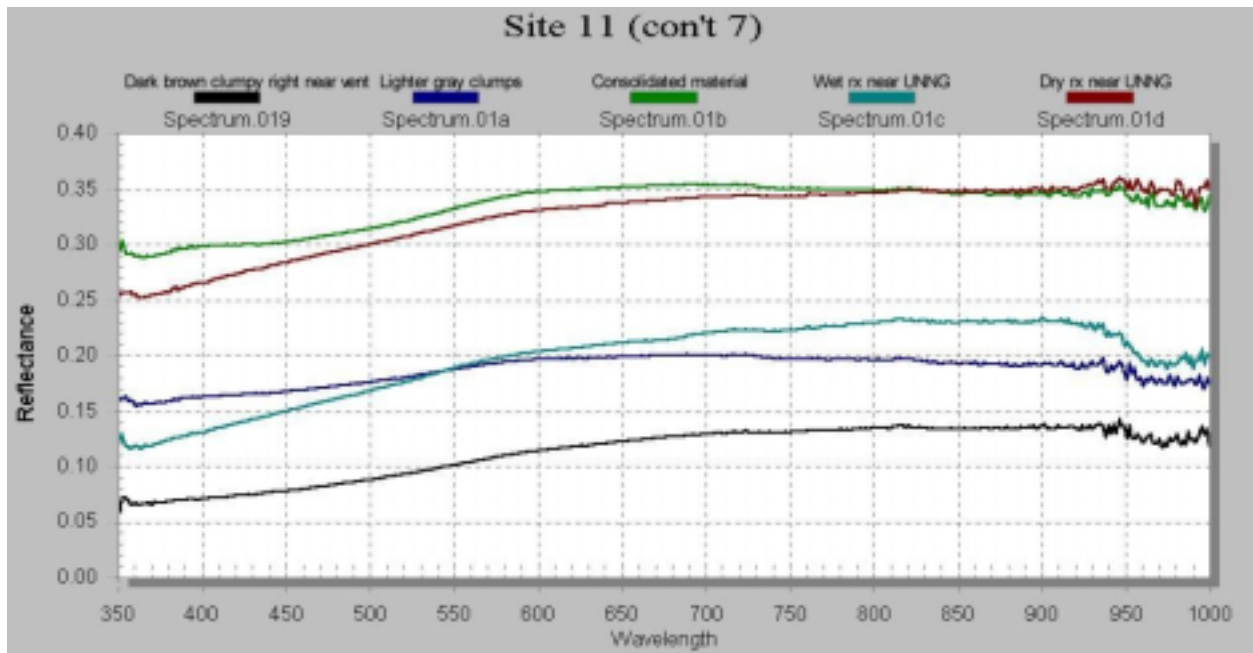
Site 11 (con't 4): Midas Spring	
Spectrum	GPS lat (N)/lon (W) (DMS)
00f – Right over mudpot	44° 27' 37.56"
010 – Outer mud crust	110° 49' 21.27"
011 – Loose rocks	44° 27' 38.71" 110° 49' 23.20"



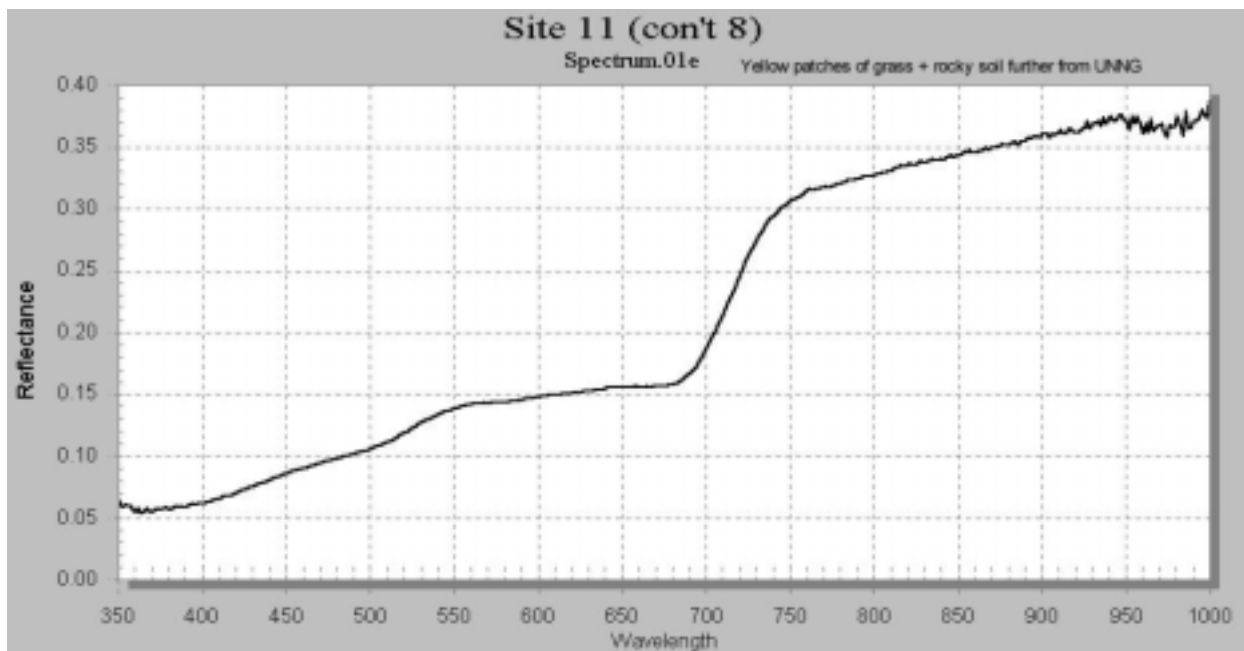
<b>Site 11 (con't 5): Midas Spring (con't)</b>	
<b>Spectrum</b>	<b>GPS lat (N)/lon (W) (DMS)</b>
012 – Clumpy sinter	44° 27' 38.71" 110° 49' 23.20"
013 – Darker sinter	
014 – Yellow sinter	
015 – Right on vent	



<b>Site 11 (con't 6): Near Midas Spring</b>	
<b>Spectrum</b>	<b>GPS lat (N)/lon (W) (DMS)</b>
016 – Darker brown deposits near vent	44° 27' 39.36" 110° 49' 23.13"
017 – Light brown deposits near vent	
018 – Black extinct deposits over old vent	

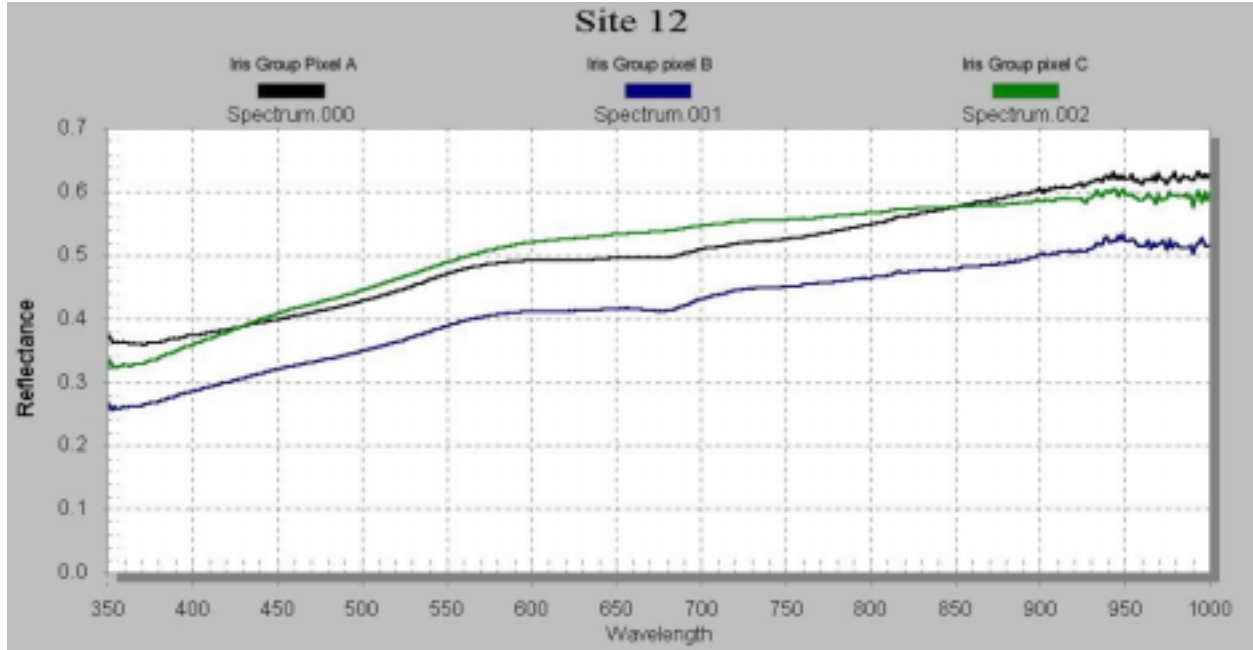


<b>Site 11 (con't 7): Unnamed geyser (UNNG)</b>	
<b>Spectrum</b>	<b>GPS lat (N)/lon (W) (DMS)</b>
019 – Dark brown clumpy right near vent	44° 27' 39.72" 110° 49' 23.53"
01a – Lighter gray clumps	
01b – Consolidated material	
01c – Wet rocks near UNNG	
01d – Dry rocks near UNNG	

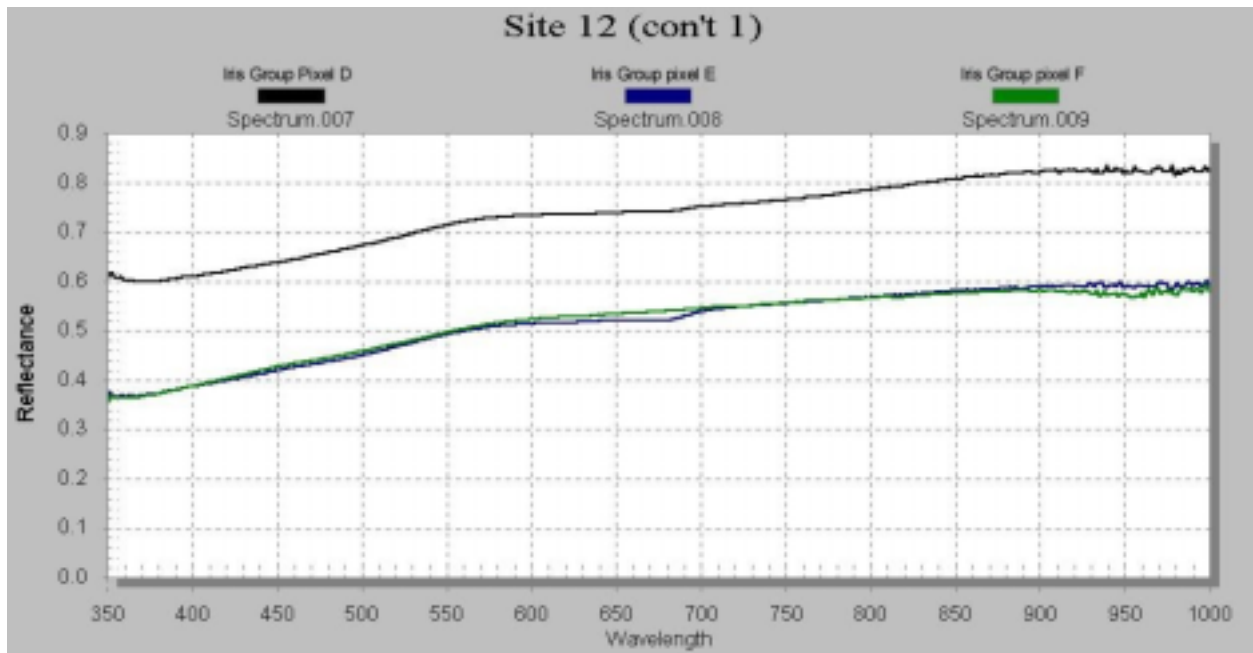


Site 11 (con't 8): UNNG (con't)	
Spectrum	GPS lat/lon (degrees)
01e – Yellow patches of grass + rocky soil further from UNNG	-

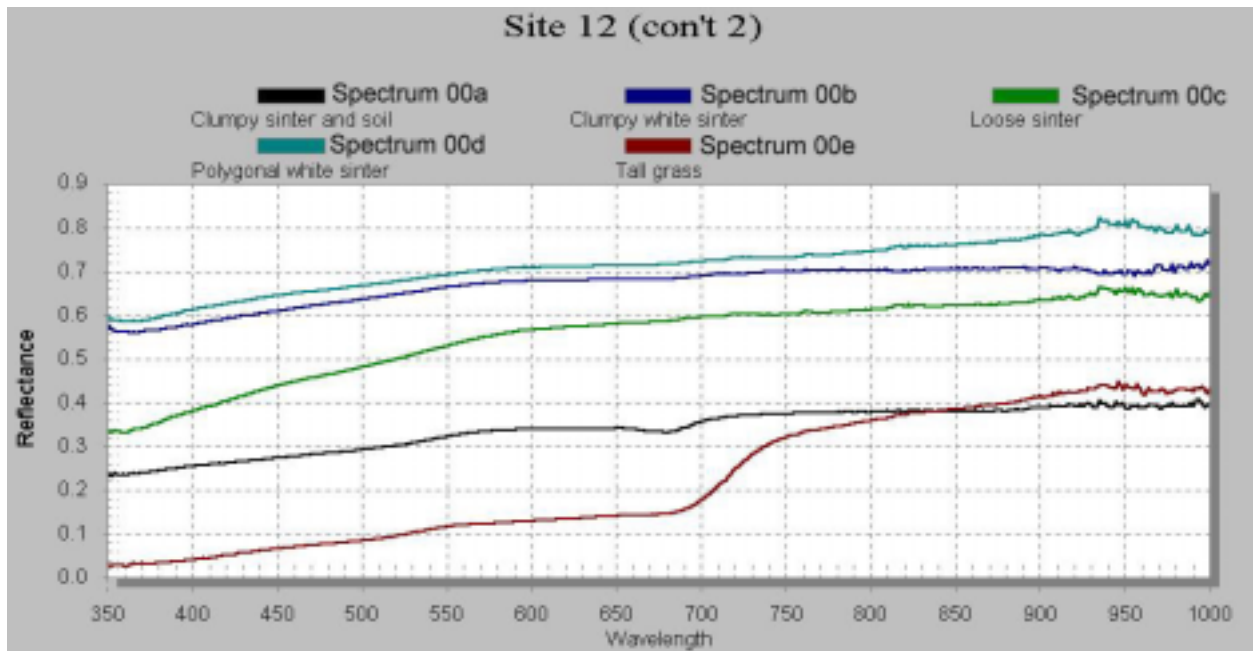
Field radiometric measurements of Site 11: Temperature of Bend Cone Geysers: 87.3 – 88.2 °C; mudpot near Midas Spring 40.6 °C; UNNG 89.3 °C



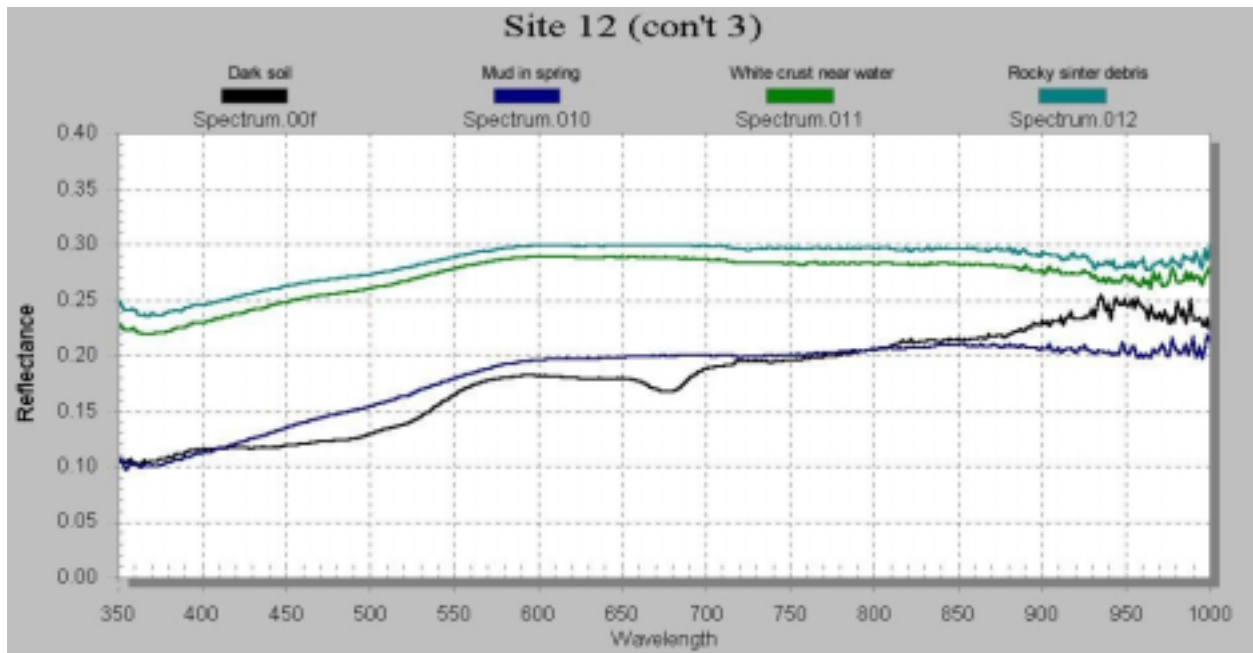
Site 12	
Spectrum	GPS lat (N)/lon (W) (DMS)
000 – Iris Group Pixel A (sinter)	44° 31' 13.47" 110° 49' 49.11"
001 – Iris Group Pixel B (sinter)	44° 31' 13.91" 110° 49' 49.41"
002 – Iris Group Pixel C (sinter)	44° 31' 13.69" 110° 49' 49.98"



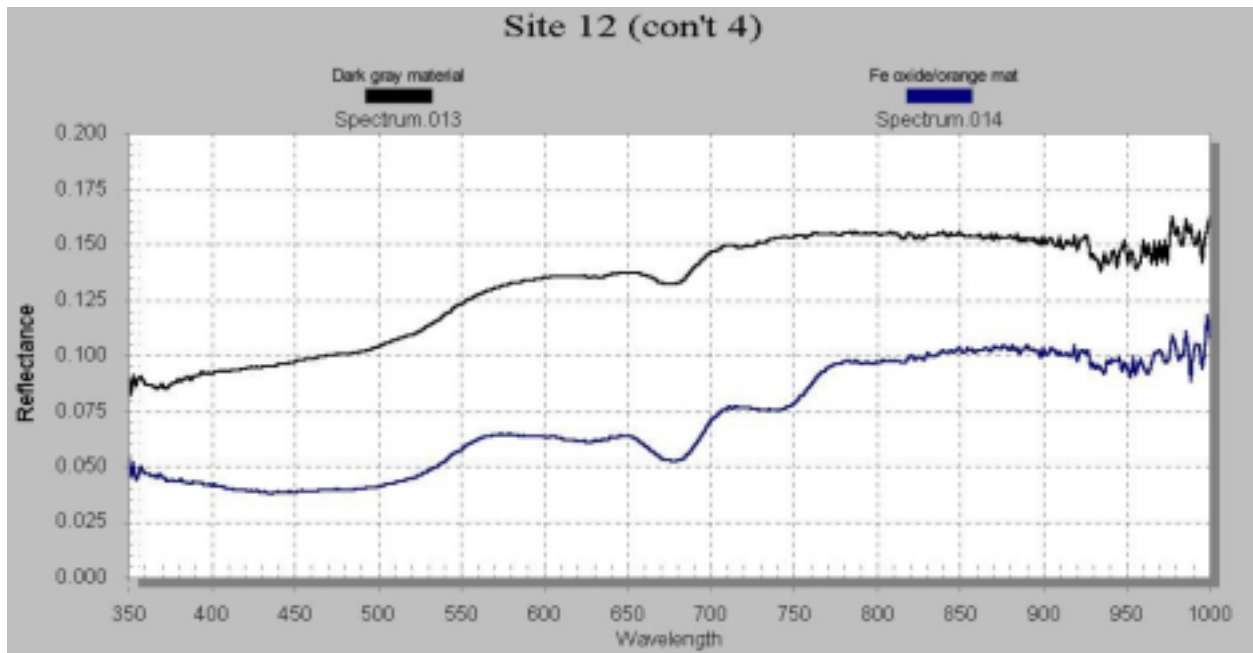
Site 12 (con't 1)	
Spectrum	GPS lat (N)/lon (W) (DMS)
007 – Iris Group Pixel D (sinter)	44° 31' 13.24" 110° 49' 49.70"
008 – Iris Group Pixel E (sinter)	44° 31' 13.69" 110° 49' 49.98"
009 – Iris Group Pixel F (sinter)	44° 31' 13.47" 110° 49' 50.47"



Site 12 (con't 2)	
Spectrum	GPS lat (N)/lon (W) (DMS)
00a – Clumpy sinter and soil	44° 31' 13.49" 110° 49' 50.71"
00b Clumpy white sinter	44° 31' 13.35" 110° 49' 50.74"
00c – Loose sinter	44° 31' 13.49" 110° 49' 50.81"
00d – Polygonal white sinter	44° 31' 13.23" 110° 49' 50.86"
00e – Tall grass	44° 31' 13.14" 110° 49' 50.82"

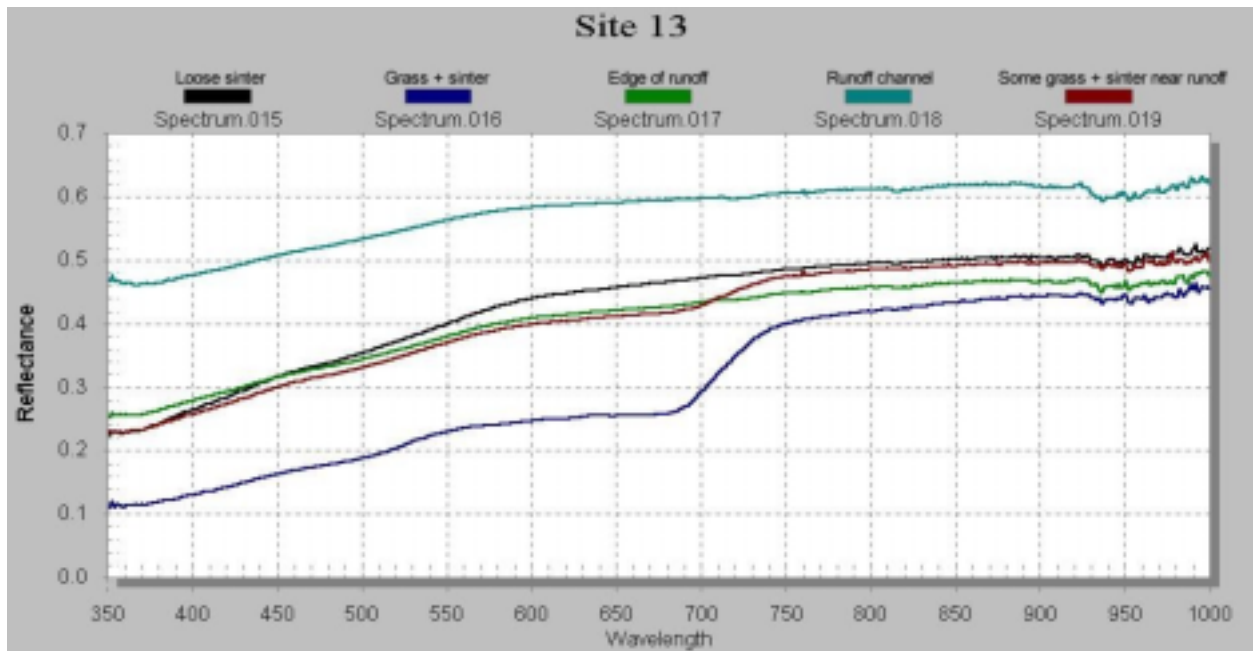


Site 12 (con't 3)	
Spectrum	GPS lat/lon (degrees)
00f – Dark soil	-
010 – Mud in spring	-
011 – White crust near water	-
012 – Rocky sinter debris	-

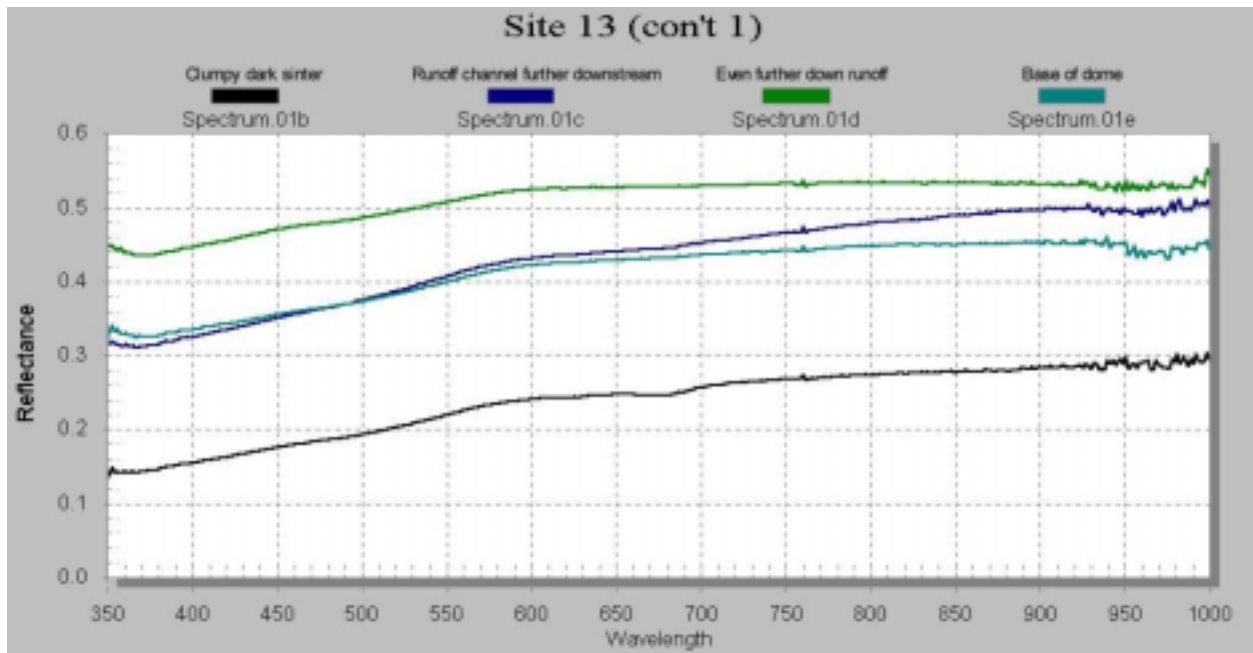


Site 12 (con't 4)	
Spectrum	GPS lat/lon (degrees)
013 – Dark gray material	-
014 – Fe oxide/orange mat	-

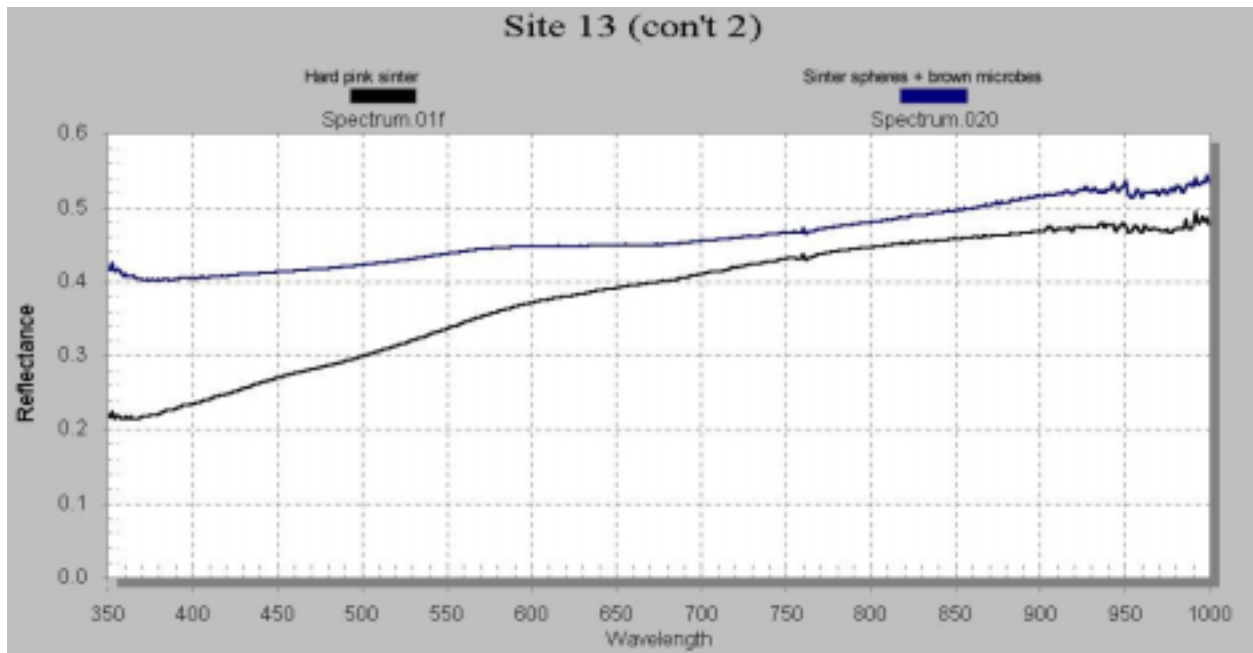
Field radiometric measurement for Site 12: There is no temperature measurement for Site 12.



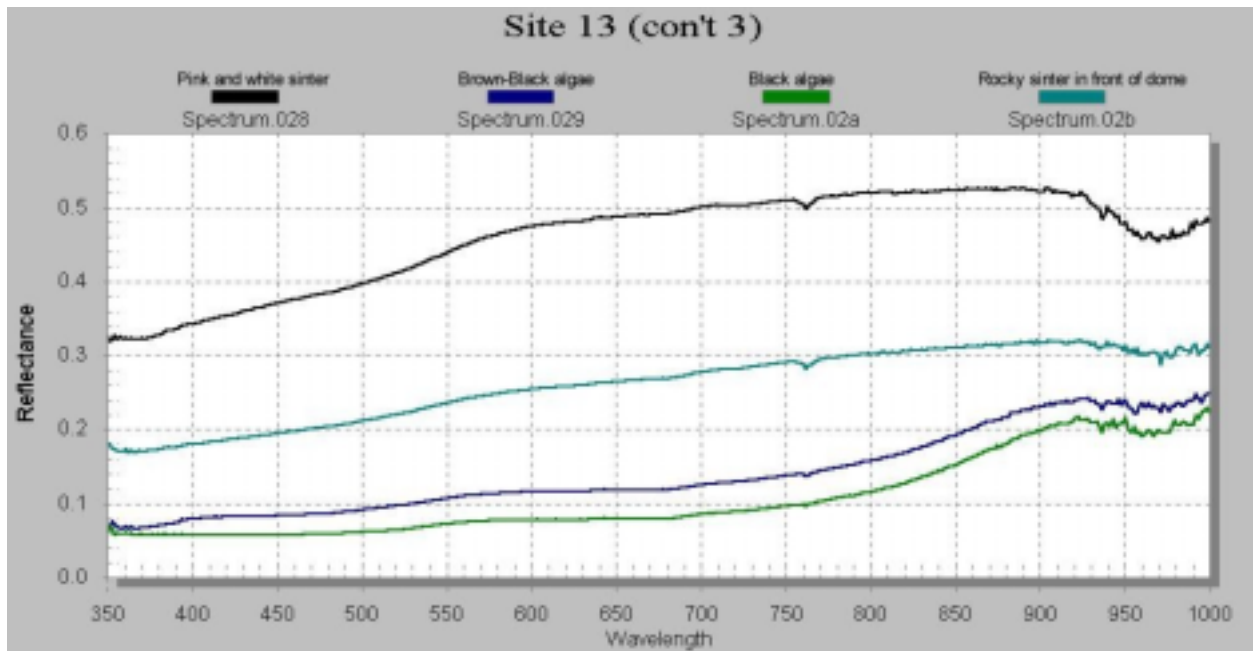
Site 13	
Spectrum	GPS lat (N)/lon (W) (DMS)
015 – Loose sinter	44° 32' 21.02" 110° 49' 11.03"
016 – Grass + sinter	44° 32' 21.06" 110° 49' 11.03"
017 – Edge of runoff	44° 32' 21.18" 110° 49' 11.10"
018 – Runoff channel	44° 32' 21.19" 110° 49' 11.12"
019 – Some grass + sinter near runoff	44° 32' 21.20" 110° 49' 11.31"



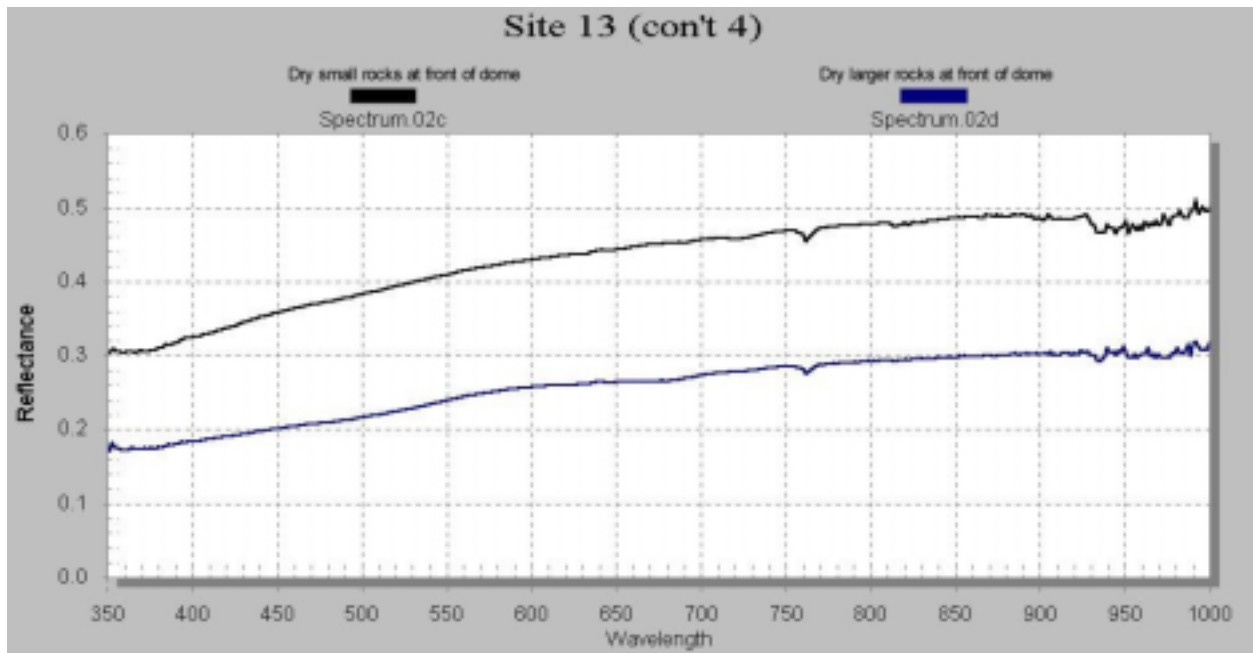
Site 13 (con't 1)	
Spectrum	GPS lat (N)/lon (W) (DMS)
01b – Clumpy dark sinter	44° 32' 21.13" 110° 49' 11.39"
01c – Runoff channel further downstream	44° 32' 21.19" 110° 49' 11.42"
01d – Even further down runoff	44° 32' 21.06" 110° 49' 11.65"
01e – Base of dome	44° 32' 21.67" 110° 49' 10.50"



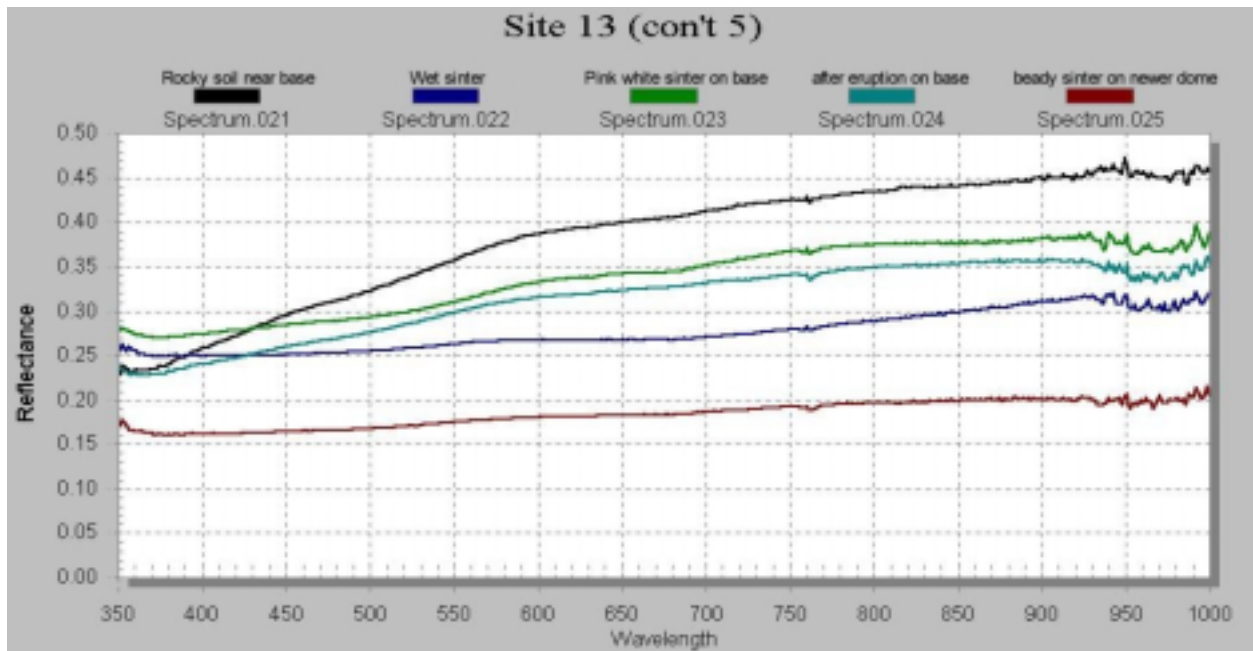
Site 13 (con't 2)	
Spectrum	GPS lat (N)/lon (W) (DMS)
01f – Hard pink sinter	44° 32' 21.70" 110° 49' 10.53"
020 – Sinter spheres + brown microbes	44° 32' 21.68" 110° 49' 10.45"



Site 13 (con't 3)	
Spectrum	GPS lat (N)/lon (W) (DMS)
028 – Pink and white sinter	44° 32' 21.89" 110° 49' 9.69"
029 – Brown-black algae	44° 32' 21.69" 110° 49' 9.61"
02a – Black algae	44° 32' 21.80" 110° 49' 9.67"
02b – Rocky sinter in front of dome	44° 32' 21.81" 110° 49' 9.60"



<b>Site 13 (con't 4)</b>	
<b>Spectrum</b>	<b>GPS lat (N)/lon (W) (DMS)</b>
02c – Dry small rocks in front of dome	44° 32' 21.75" 110° 49' 9.49"
02d – Dry larger rocks at front of dome	44° 32' 21.77" 110° 49' 9.43"



Site 13 (con't 5)	
Spectrum	GPS lat (N)/lon (W) (DMS)
021 – Rocky soil near base	44° 32' 21.75" 110° 49' 10.68"
022 – Wet sinter	44° 32' 21.81" 110° 49' 10.35"
023 – Pink white sinter on dome	44° 32' 21.81" 110° 49' 10.19"
024 – After eruption on base	44° 32' 21.87" 110° 49' 10.04"
025 – Beady sinter on newer dome	44° 32' 21.79" 110° 49' 10.13"

Field radiometric measurement for Site 13: There is no temperature measurement for Site 13.

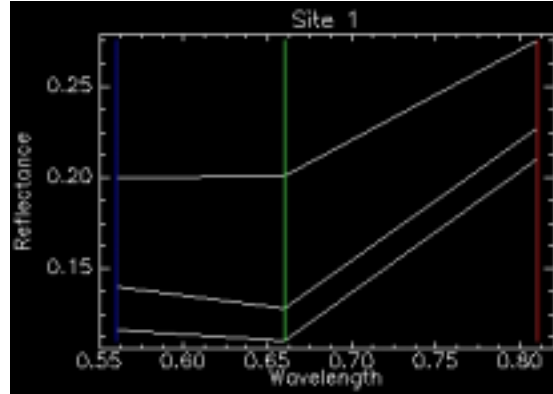
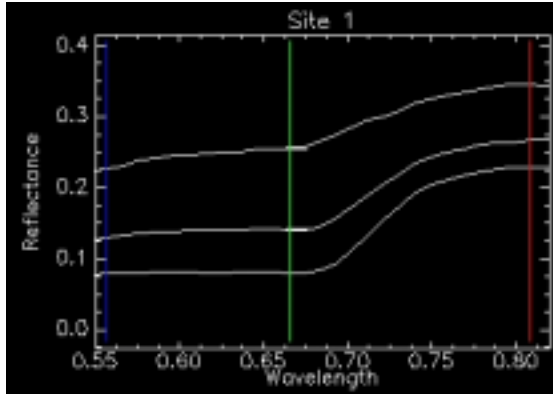
**Site 14: There are no field VNIR spectra for Site 14**

<b>Site 14</b>	
<b>Field radiometer (°C)</b>	<b>GPS lat (N)/lon (W) (DMS)</b>
41	44° 27' 57.47" 110° 50' 57.32"
41	44° 27' 57.37" 110° 50' 57.25"
64	44° 27' 57.32" 110° 50' 57.18"
56	44° 27' 57.28" 110° 50' 57.09"
66	44° 27' 57.15" 110° 50' 57.10"
43	44° 27' 57.91" 110° 50' 57.39"

## **Appendix B**

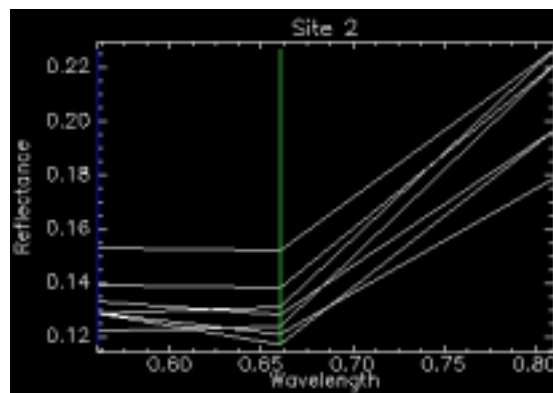
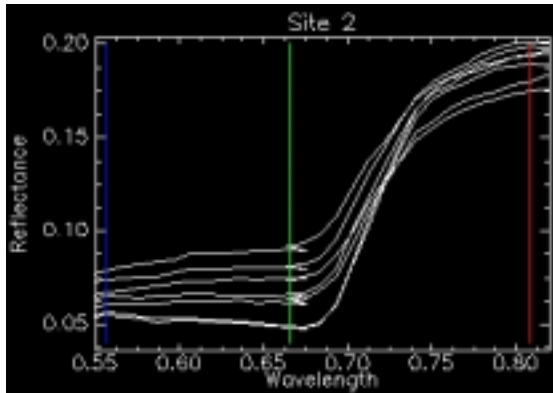
### **ASTER and AVIRIS VNIR Reflectance Spectra**

**Note: All AVIRIS and ASTER VNIR wavelengths are in micrometers ( $\mu\text{m}$ ).**



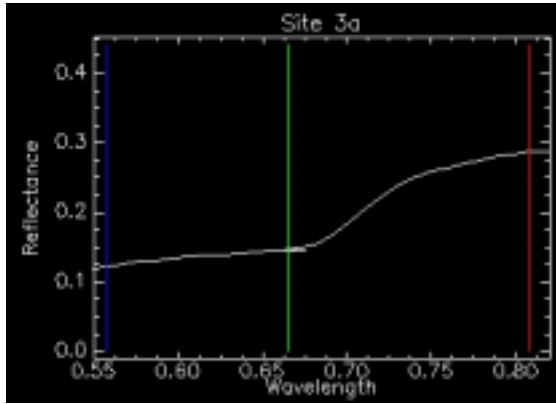
AVIRIS VNIR reflectance spectra (Site 1).

ASTER VNIR reflectance spectra (Site 1).

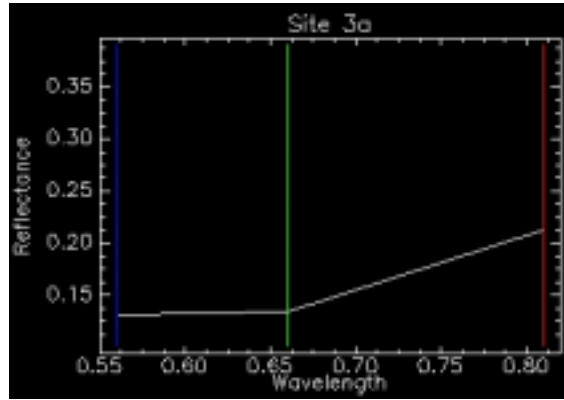


AVIRIS VNIR reflectance spectra (Site 2).

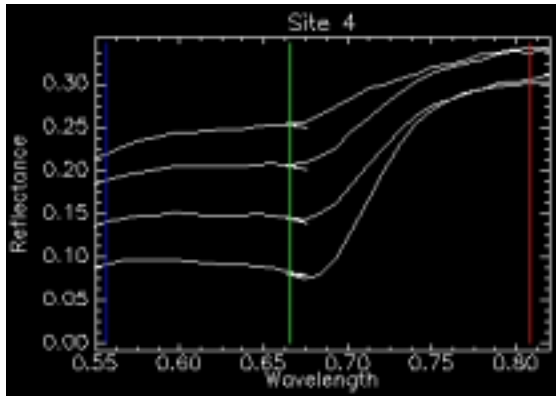
ASTER VNIR reflectance spectra (Site 2).



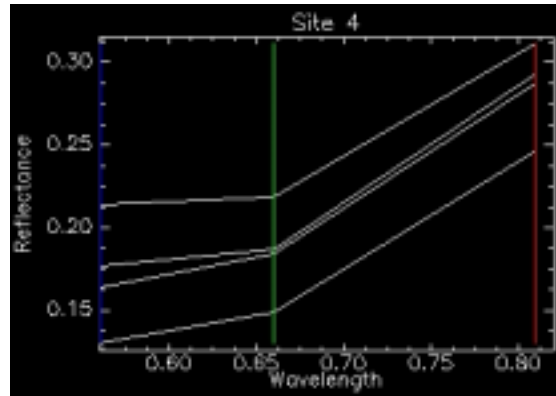
AVIRIS VNIR reflectance spectra (Site 3a).



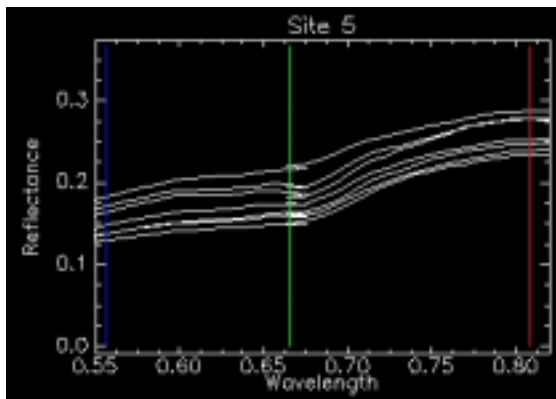
ASTER VNIR reflectance spectra (Site 3a).



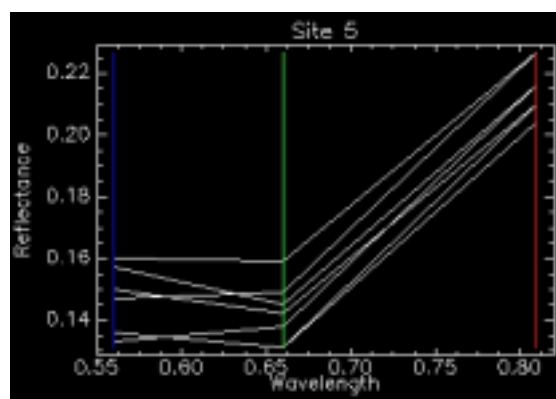
AVIRIS VNIR reflectance spectra (Site 4).



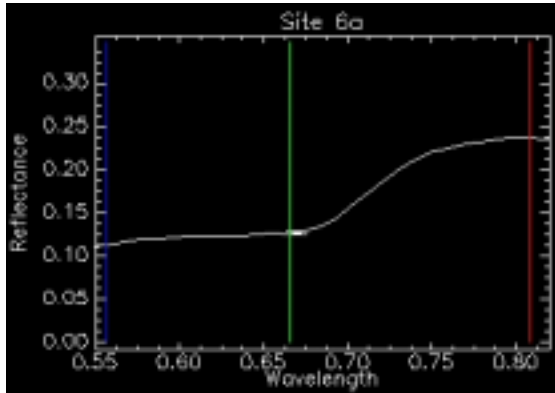
ASTER VNIR reflectance spectra (Site 4).



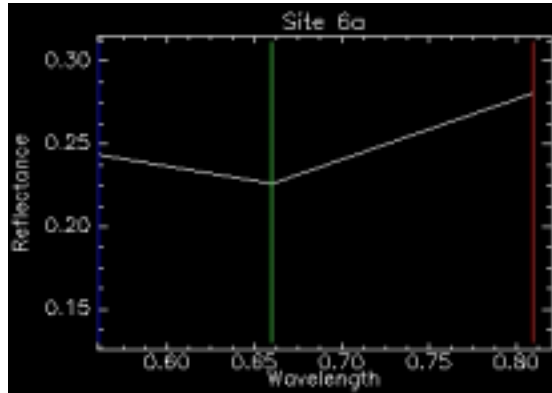
AVIRIS VNIR reflectance spectra (Site 5).



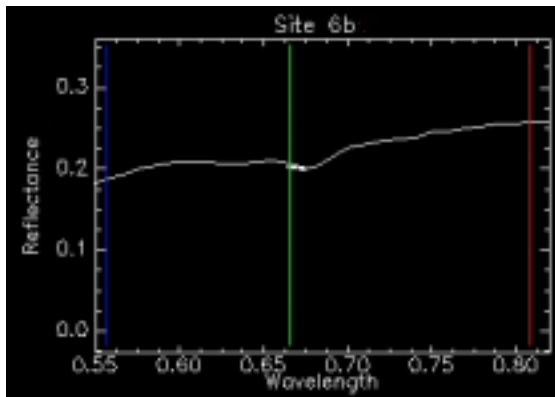
ASTER VNIR reflectance spectra (Site 5).



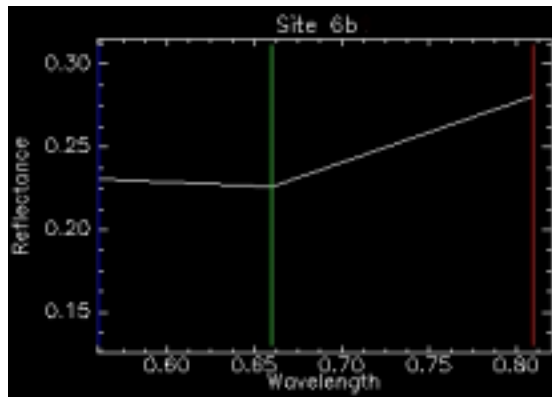
AVIRIS VNIR reflectance spectra (Site 6a).



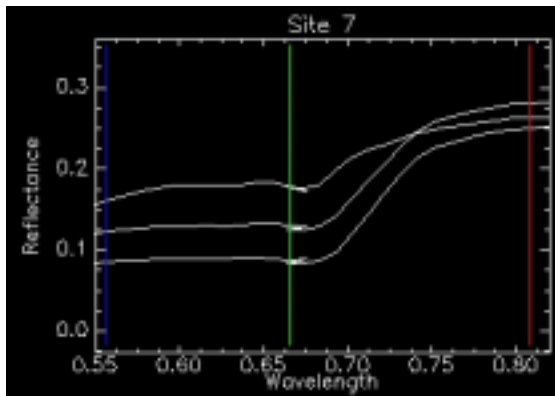
ASTER VNIR reflectance spectra (Site 6a).



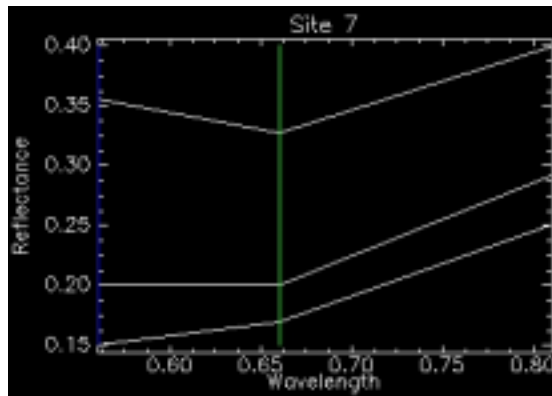
AVIRIS VNIR reflectance spectra (Site 6b).



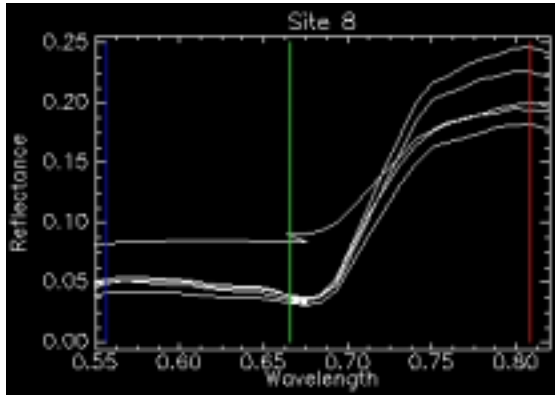
ASTER VNIR reflectance spectra (Site 6b).



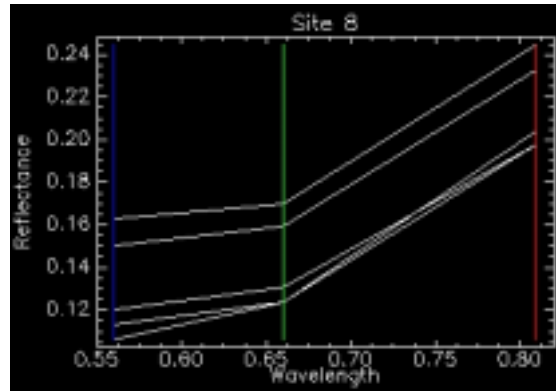
AVIRIS VNIR reflectance spectra (Site 7).



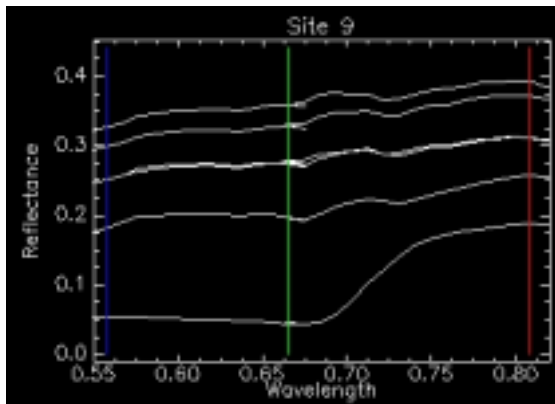
ASTER VNIR reflectance spectra (Site 7).



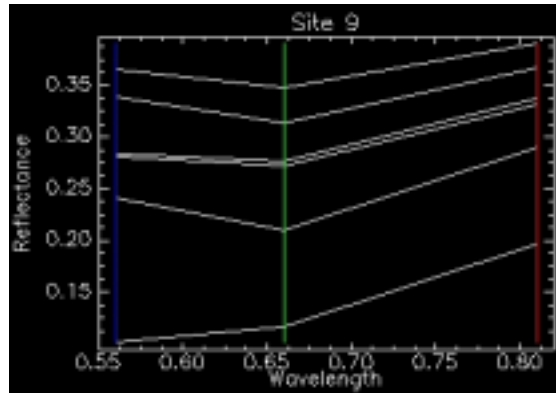
AVIRIS VNIR reflectance spectra (Site 8).



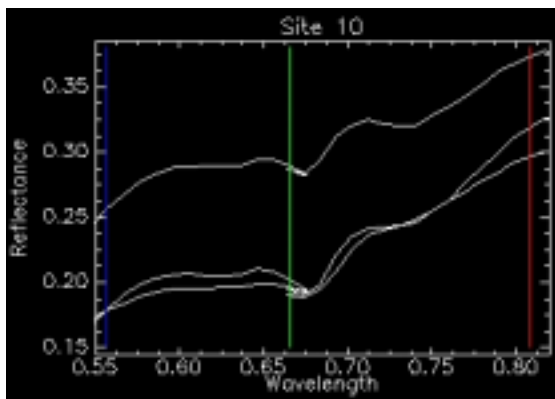
ASTER VNIR reflectance spectra (Site 8).



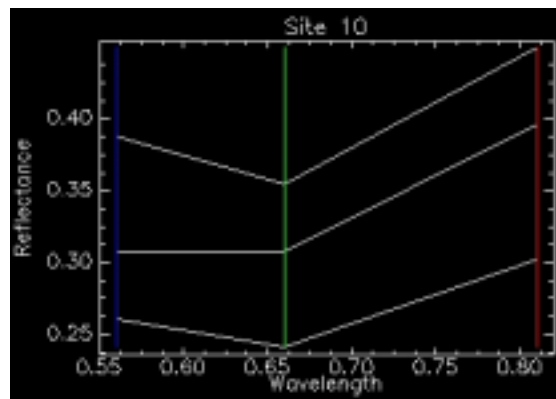
AVIRIS VNIR reflectance spectra (Site 9).



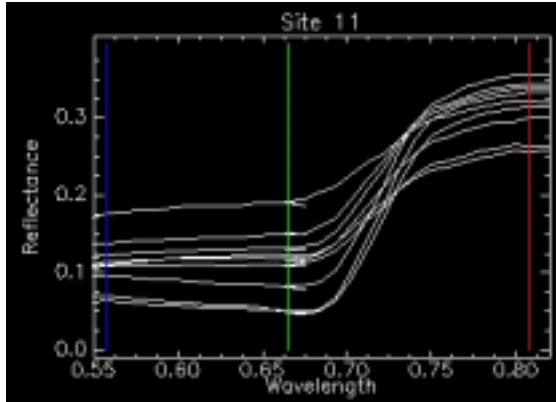
ASTER VNIR reflectance spectra (Site 9).



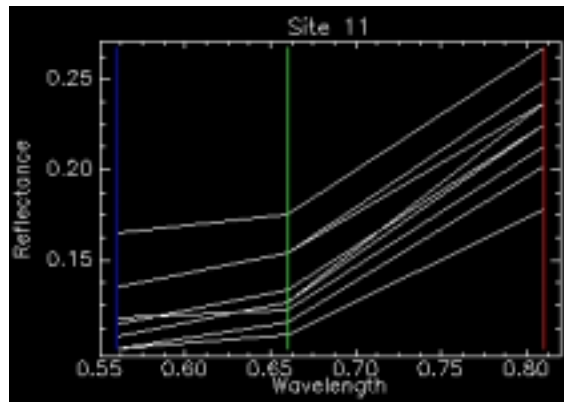
AVIRIS VNIR reflectance spectra (Site 10).



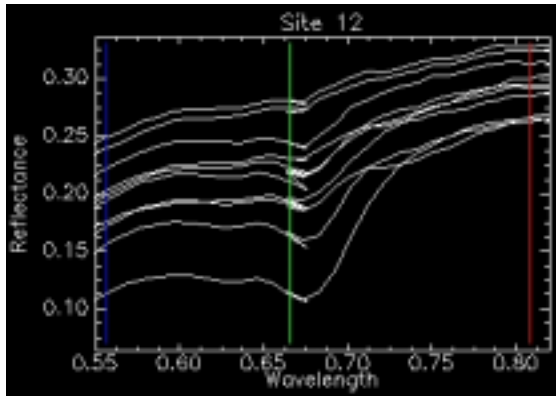
ASTER VNIR reflectance spectra (Site 10).



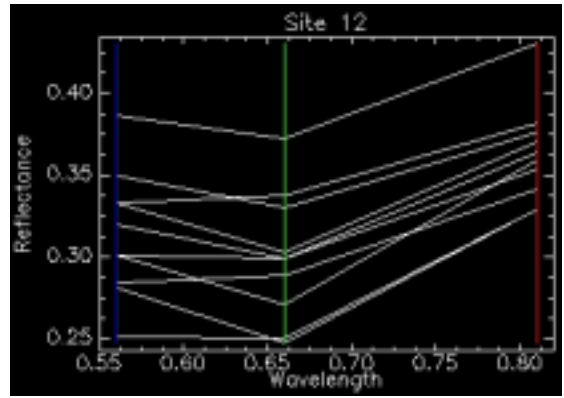
AVIRIS VNIR reflectance spectra (Site 11).



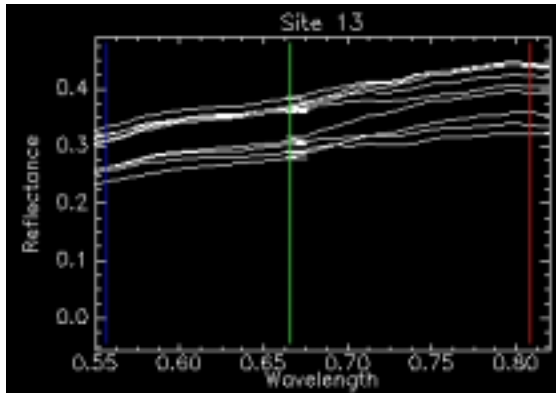
ASTER VNIR reflectance spectra (Site 11).



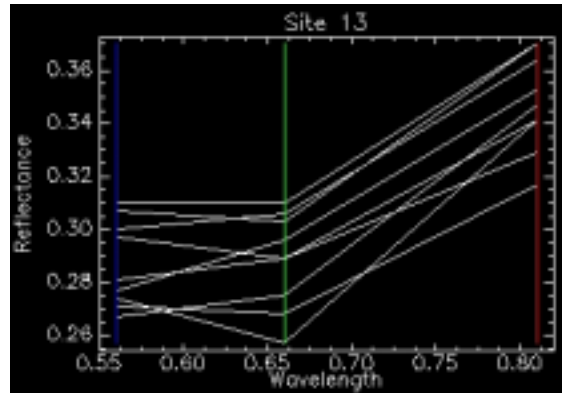
AVIRIS VNIR reflectance spectra (Site 12).



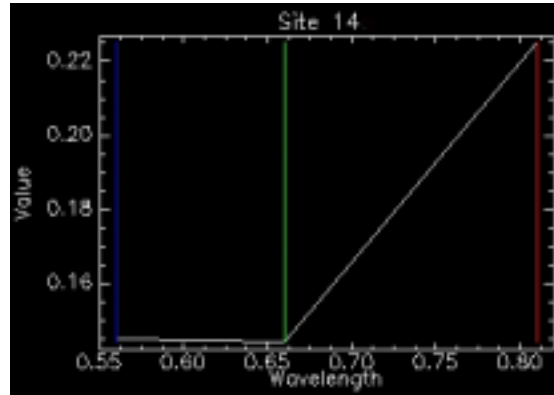
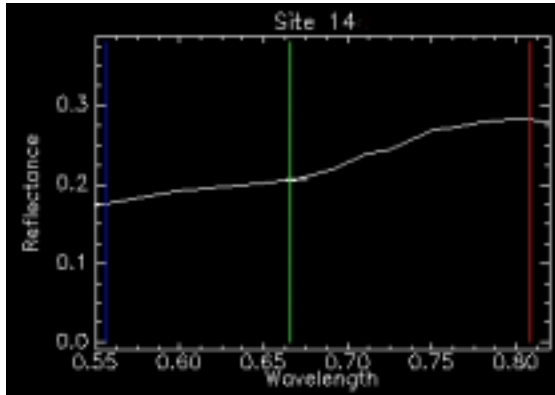
ASTER VNIR reflectance spectra (Site 12).



AVIRIS VNIR reflectance spectra (Site 13).



ASTER VNIR reflectance spectra (Site 13).

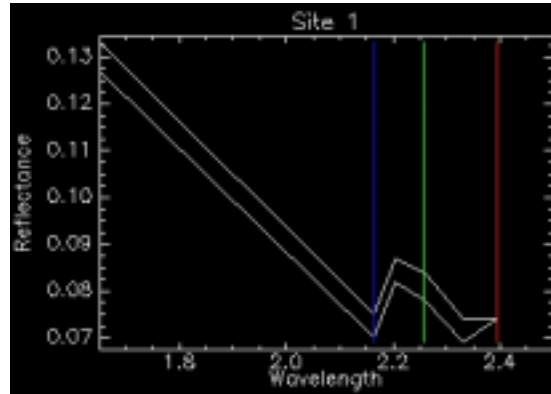
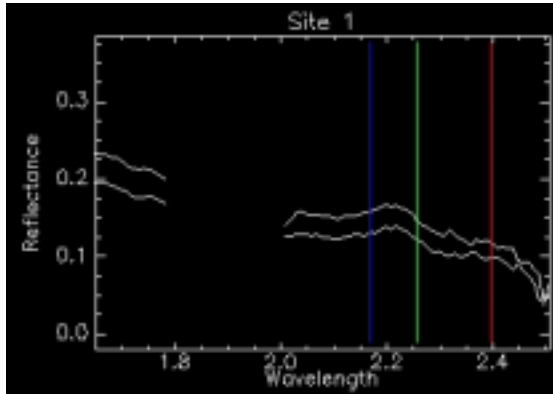


AVIRIS VNIR reflectance spectra (Site 14). ASTER VNIR reflectance spectra (Site 14).

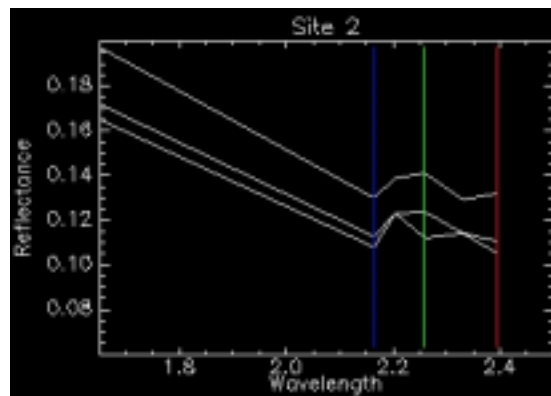
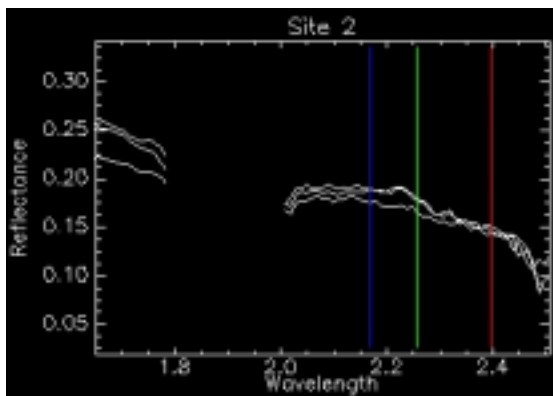
## **Appendix C**

### **ASTER and AVIRIS SWIR Reflectance Spectra**

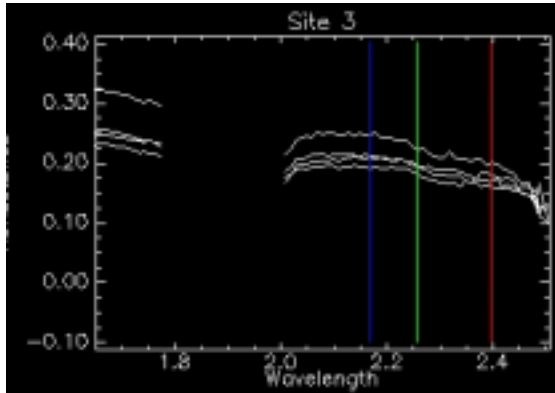
**Note: All AVIRIS and ASTER SWIR wavelengths are in micrometers ( $\mu\text{m}$ ).**



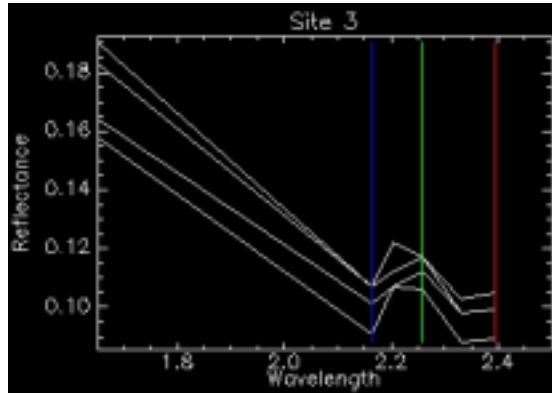
AVIRIS SWIR reflectance spectra (Site 1). ASTER SWIR reflectance spectra (Site 1).



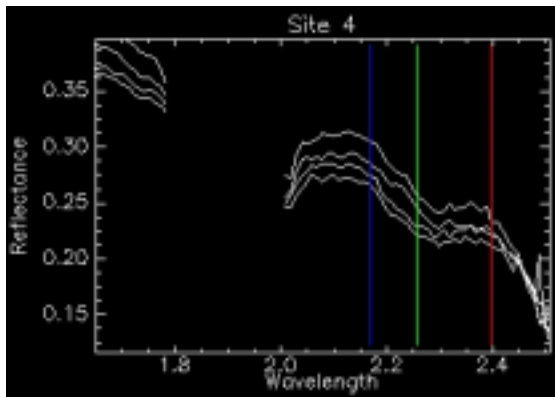
AVIRIS SWIR reflectance spectra (Site 2). ASTER SWIR reflectance spectra (Site 2).



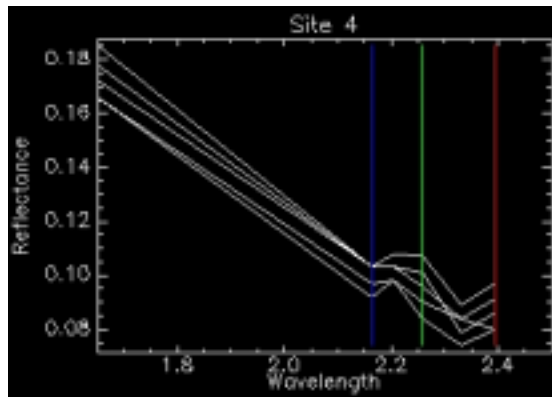
AVIRIS SWIR reflectance spectra (Site 3).



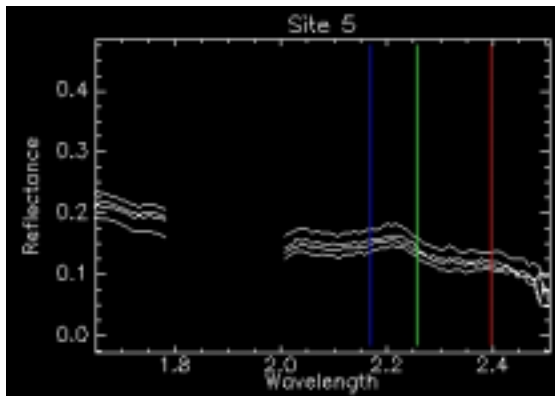
ASTER SWIR reflectance spectra (Site 3).



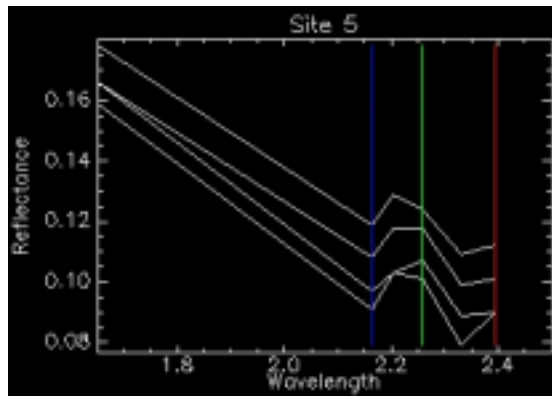
AVIRIS SWIR reflectance spectra (Site 4).



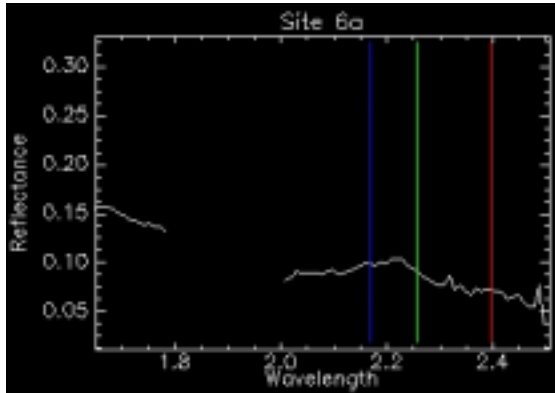
ASTER SWIR reflectance spectra (Site 4).



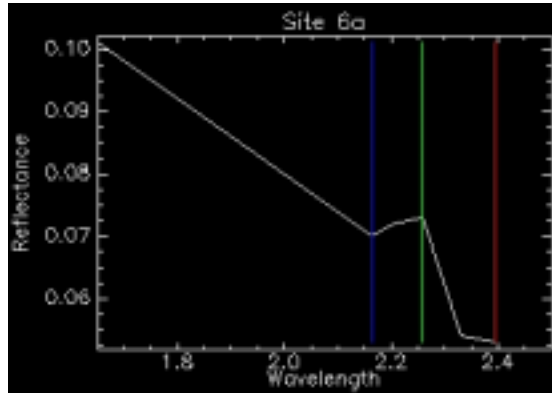
AVIRIS SWIR reflectance spectra (Site 5).



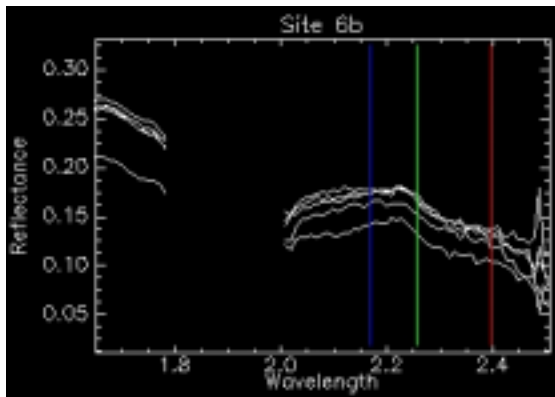
ASTER SWIR reflectance spectra (Site 5).



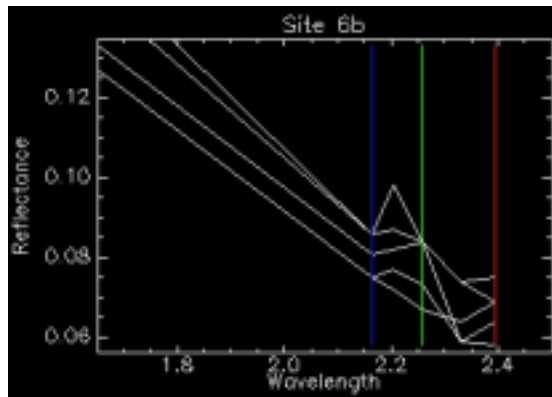
AVIRIS SWIR reflectance spectra (Site 6a).



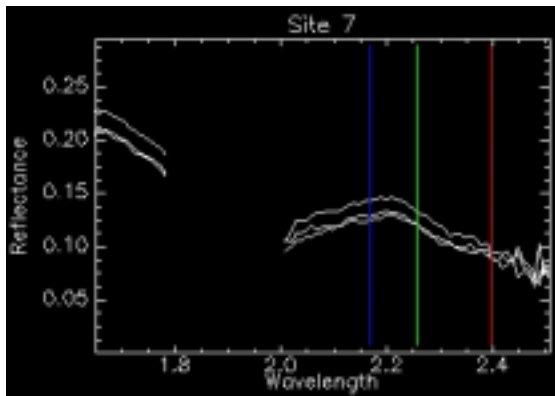
ASTER SWIR reflectance spectra (Site 6a).



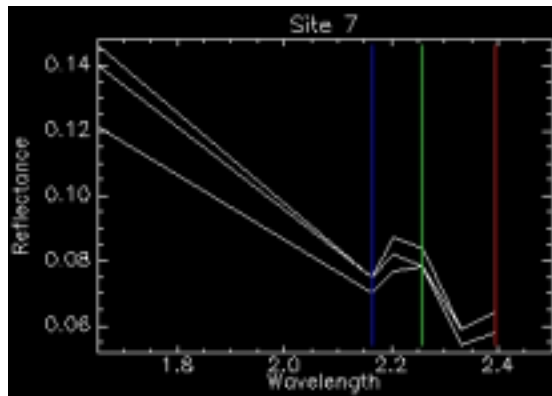
AVIRIS SWIR reflectance spectra (Site 6b).



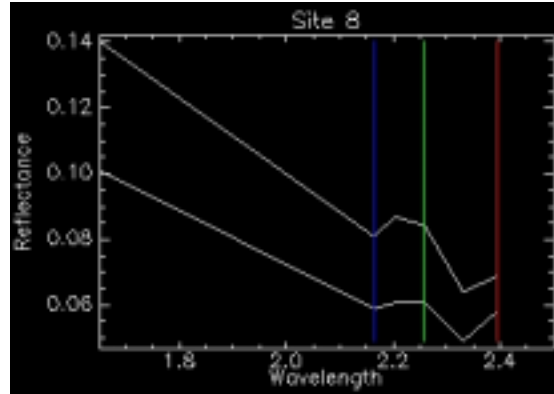
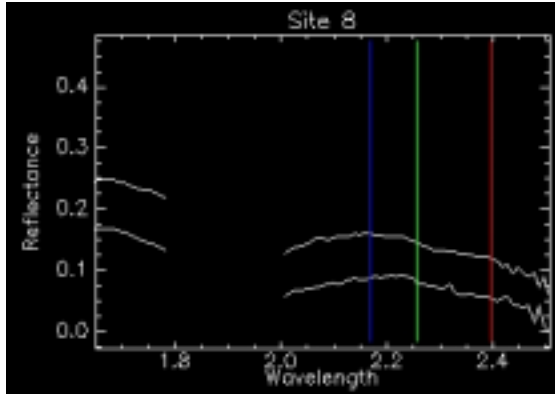
ASTER SWIR reflectance spectra (Site 6b).



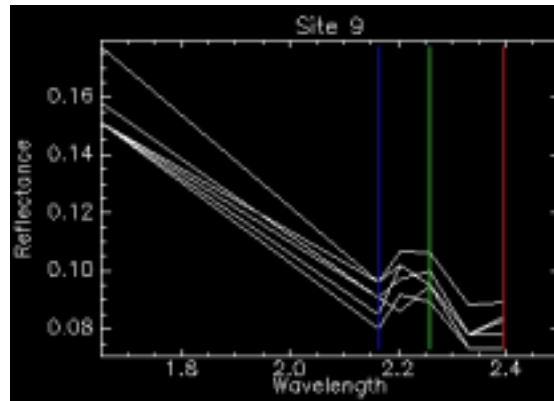
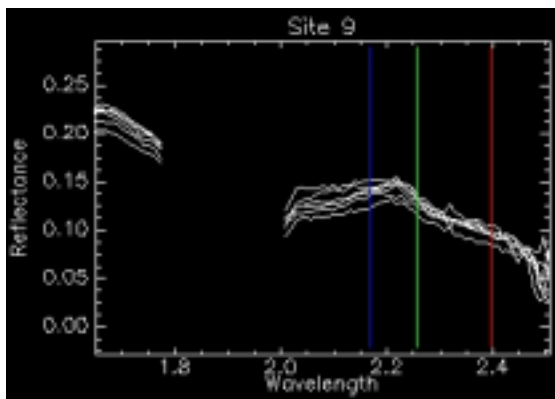
AVIRIS SWIR reflectance spectra (Site 7).



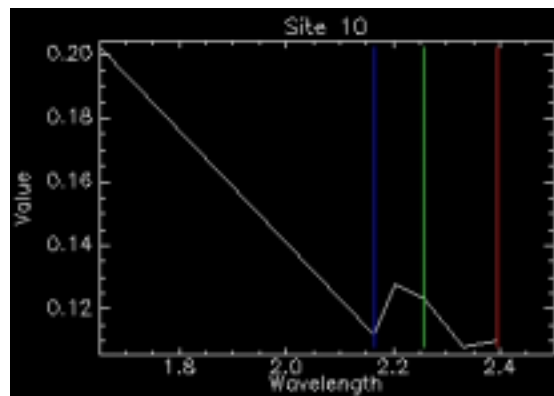
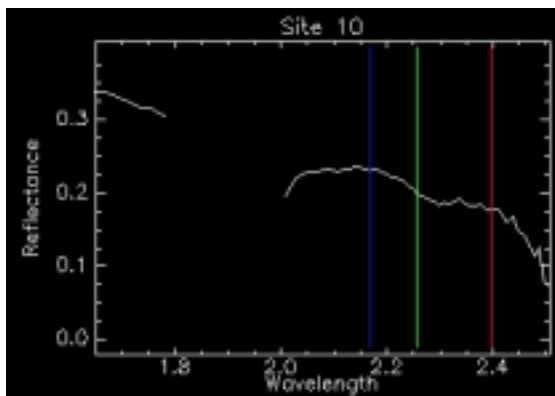
ASTER SWIR reflectance spectra (Site 7).



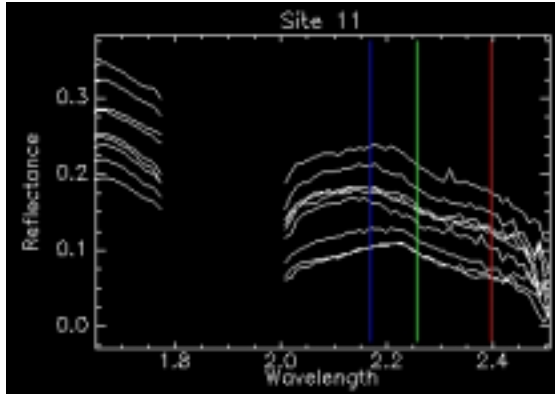
AVIRIS SWIR reflectance spectra (Site 8). ASTER SWIR reflectance spectra (Site 8).



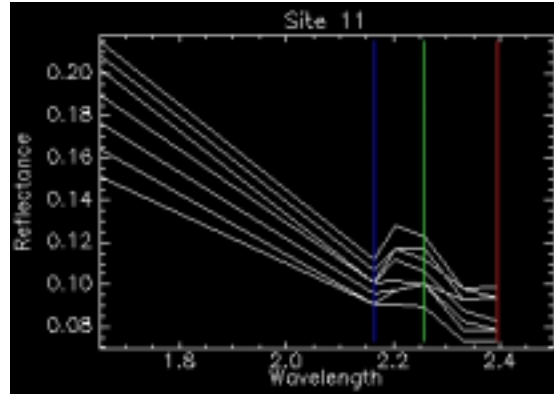
AVIRIS SWIR reflectance spectra (Site 9). ASTER SWIR reflectance spectra (Site 9).



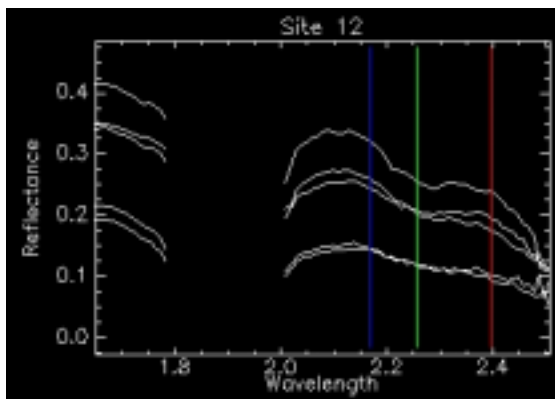
AVIRIS SWIR reflectance spectra (Site 10). ASTER SWIR reflectance spectra (Site 10).



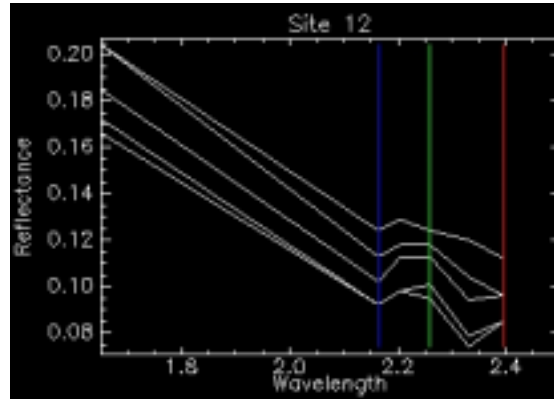
AVIRIS SWIR reflectance spectra (Site 11).



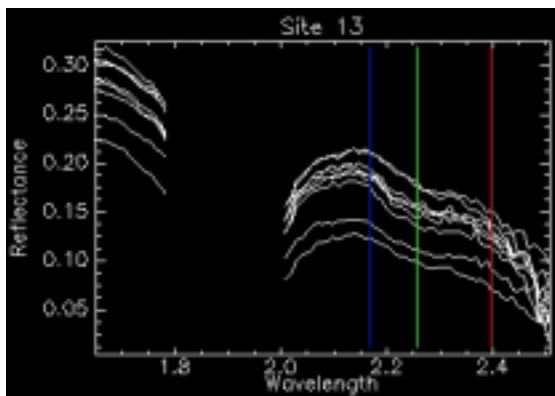
ASTER SWIR reflectance spectra (Site 11).



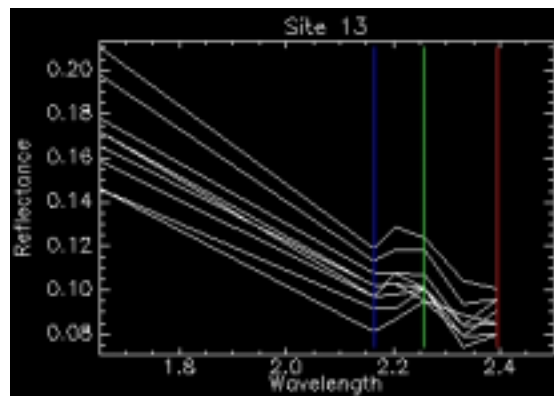
AVIRIS SWIR reflectance spectra (Site 12).



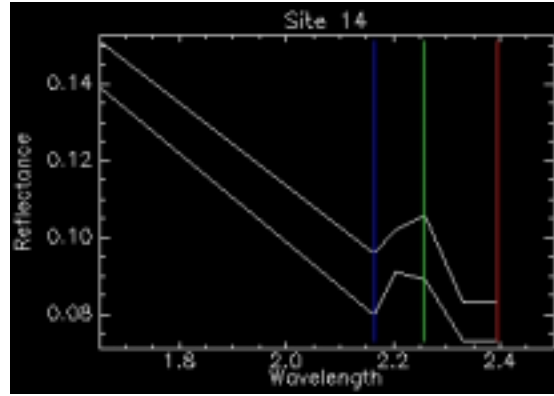
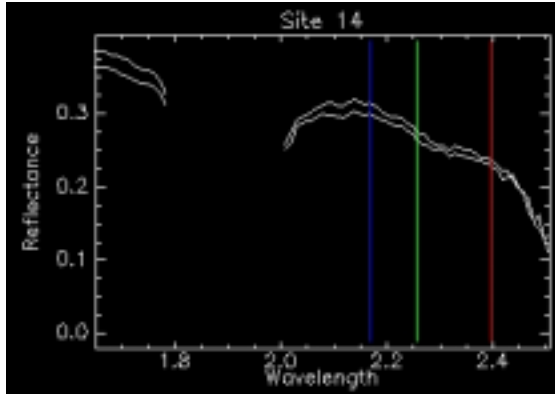
ASTER SWIR reflectance spectra (Site 12).



AVIRIS SWIR reflectance spectra (Site 13).



ASTER SWIR reflectance spectra (Site 13).

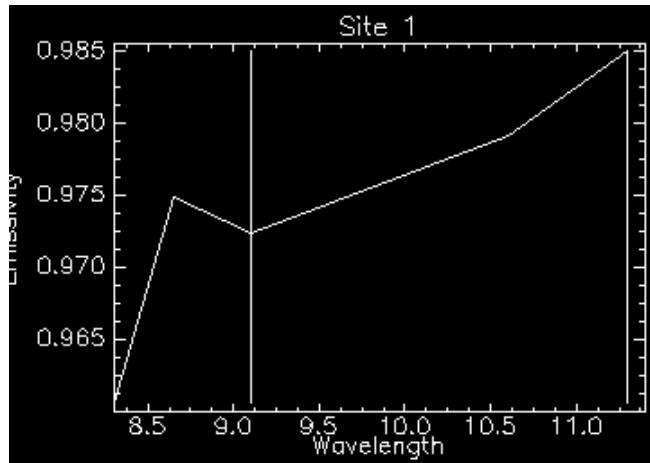


AVIRIS SWIR reflectance spectra (Site 14). ASTER SWIR reflectance spectra (Site 14).

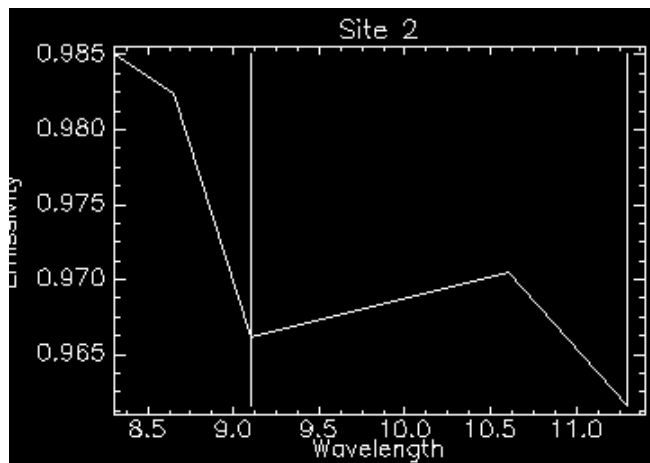
## **Appendix D**

### **ASTER TIR Emissivity Spectra**

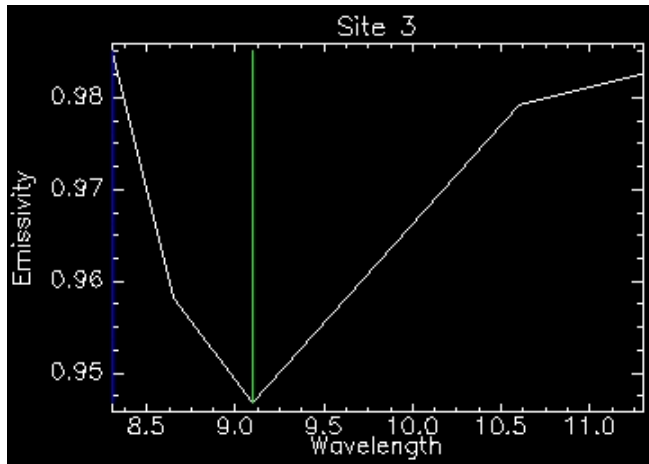
**Note: All ASTER TIR emissivity wavelengths are in micrometers ( $\mu\text{m}$ ).**



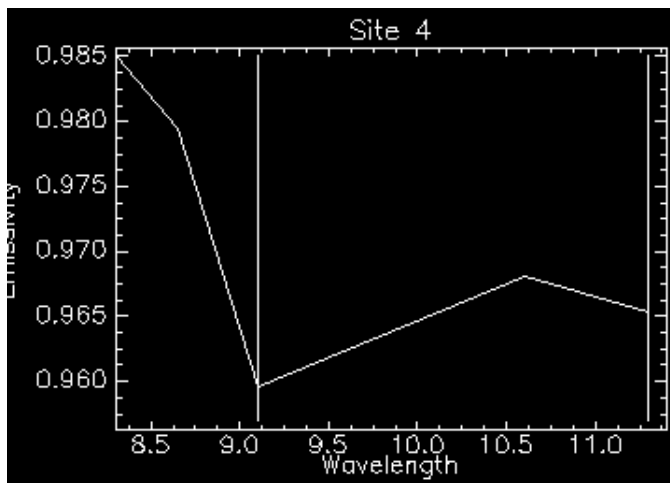
Emissivity spectra of Site 1.



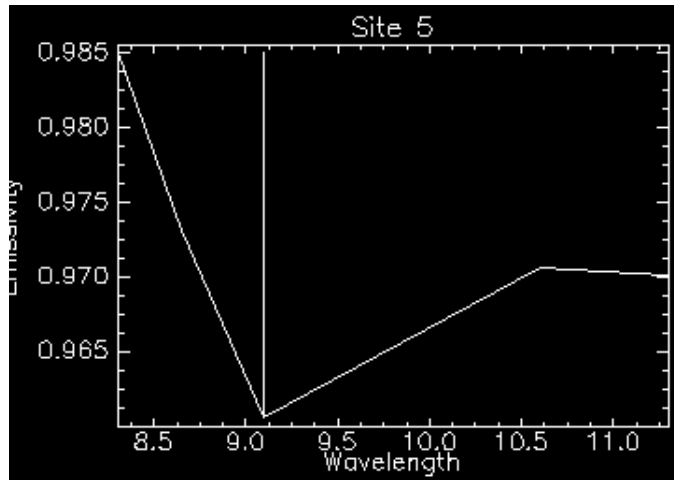
Emissivity spectra of Site 2.



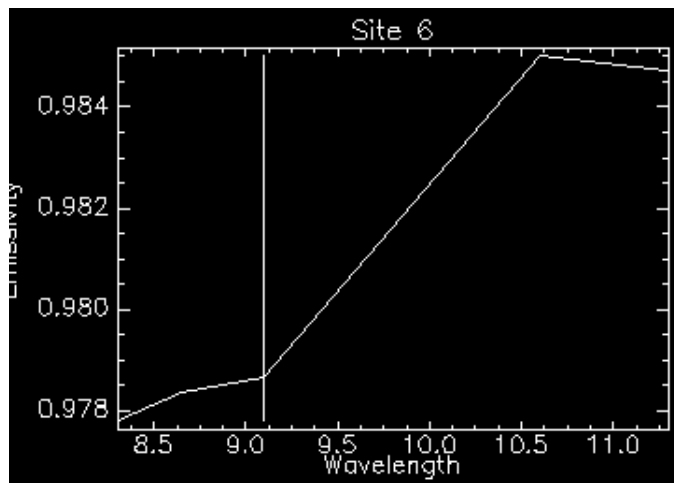
Emissivity spectra of Site 3.



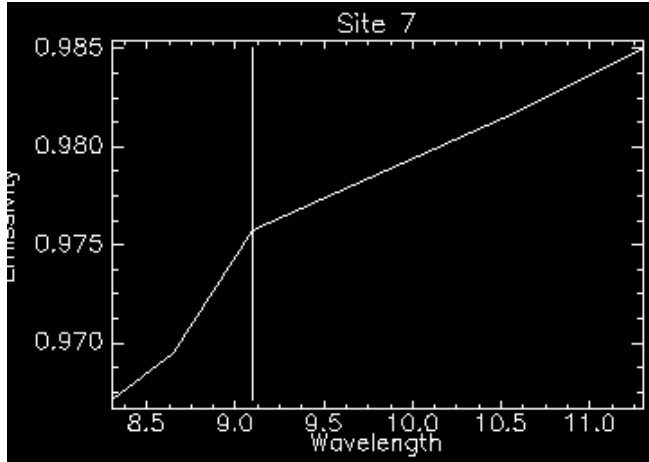
Emissivity spectra of Site 4.



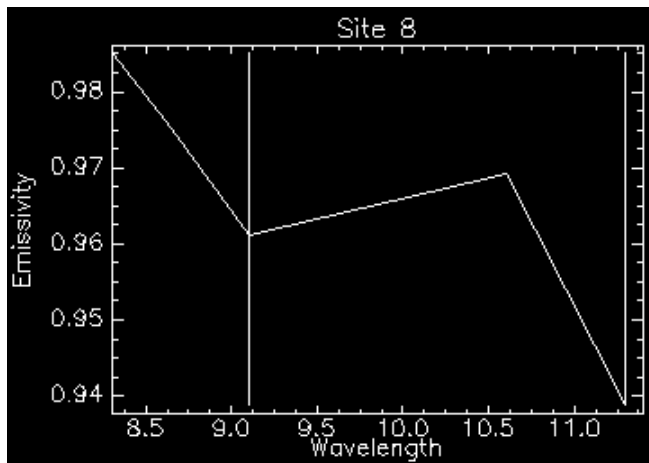
Emissivity spectra of Site 5.



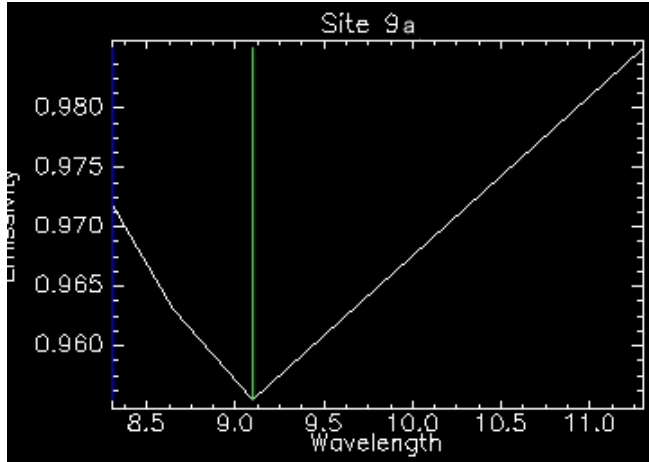
Emissivity spectra of Site 6.



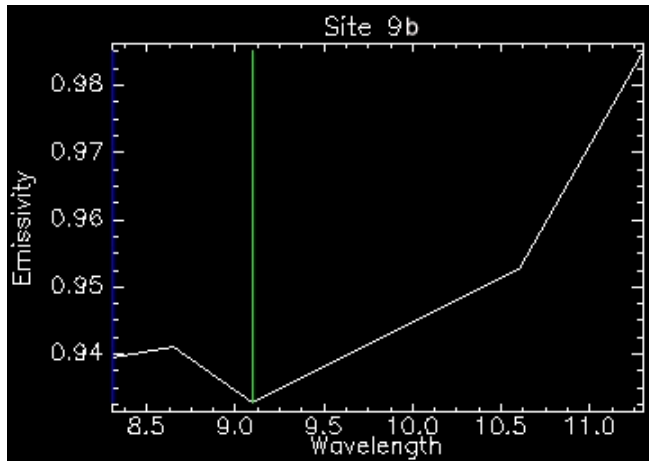
Emissivity spectra of Site 7.



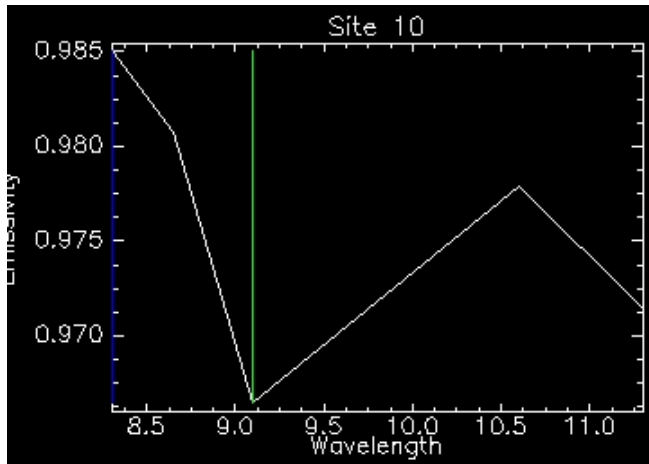
Emissivity spectra of Site 8.



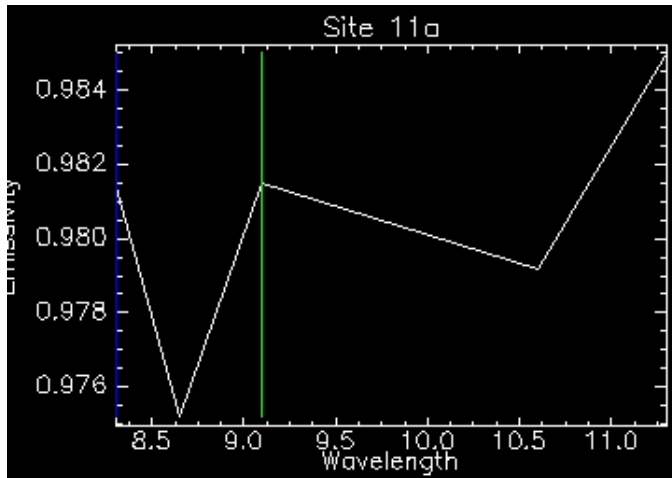
Emissivity spectra of Site 9a (active).



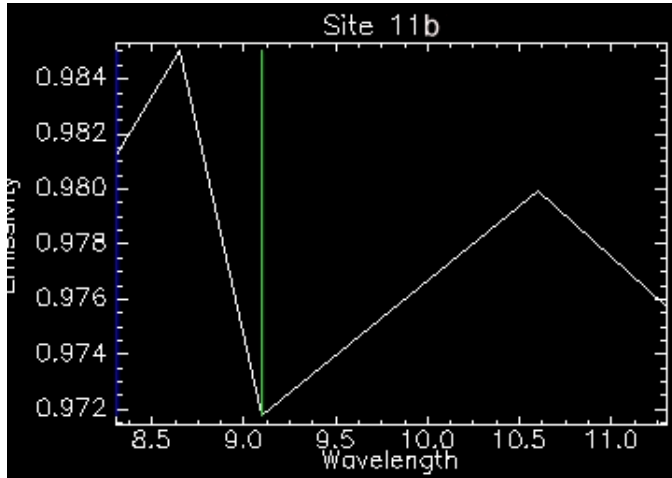
Emissivity spectra of Site 9b.



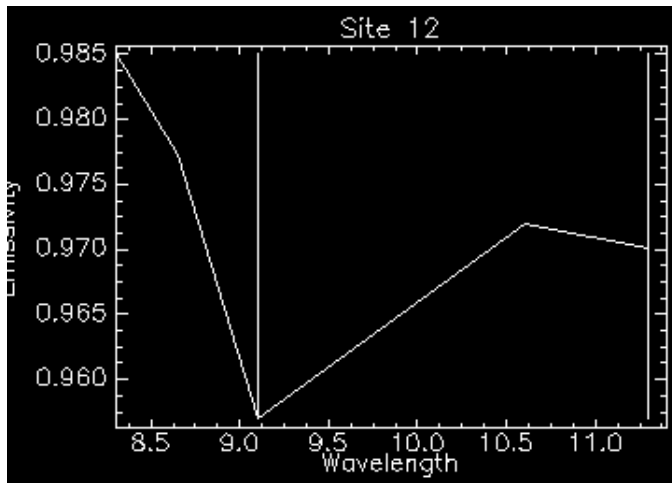
Emissivity spectra of Site 10.



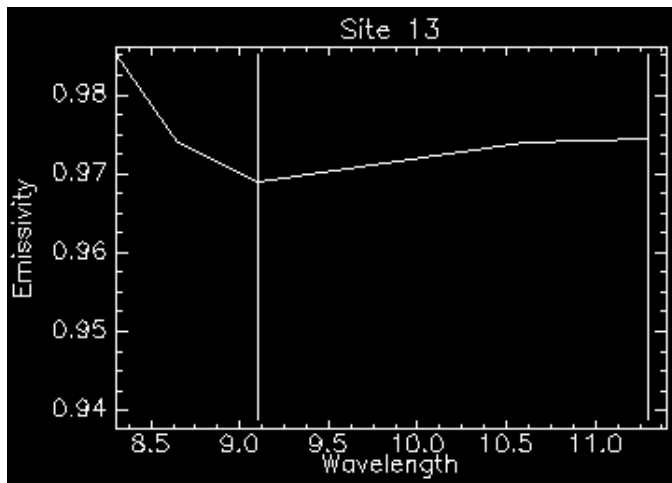
Emissivity spectra of Site 11a.



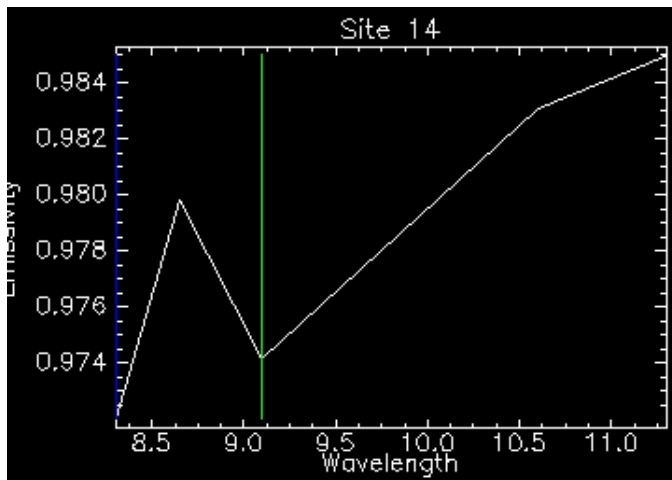
Emissivity spectra of Site 11b.



Emissivity spectra of Site 12.



Emissivity spectra of Site 13.



Emissivity spectra of Site 14.

## **Appendix E**

### **List of Commonly Used Acronyms**

ASTER = Advanced Spaceborne Thermal Emission and Reflection Radiometer

AVIRIS = Airborne Visible/IR Image Spectrometer

LGB = Lower Geyser Basin

MER = Mars Exploration Rover

MGB = Midway Geyser Basin

MGS = Mars Global Surveyor

SWIR = Short-wave infrared

TES = Thermal Emission Spectrometer

THEMIS = Thermal Emission Imaging System

TIMS = Thermal Infrared Multispectral Scanner

TIR = Thermal Infrared

UGB = Upper Geyser Basin

VIS = Visible

VNIR = Visible to near-infrared

## **BIBLIOGRAPHY**

## References

- Abrams, M.J., L. Ashley, L. Rowan, A. Goetz, and A. Kahle, 1977. Mapping of Hydrothermal Alteration in the Cuprite Mining District, Nevada, Using Aircraft Scanner Images for the Spectral Region 0.46 to 2.36 $\mu$ m. *Geology* 5, 713-718.
- Abrams, M.J., 2000. The Advanced Spaceborne Thermal Emission And Reflectance Radiometer (ASTER): Data products for the high spatial resolution imager on NASA's Terra platform, *Int. J. Rem. Sens.*, 21, 847-859.
- Bargar, K.E. and R.O. Fournier, 1988. Effects of Glacial Ice on Subsurface Temperatures of Subsurface Temperatures of Hydrothermal Systems in Yellowstone National Park, Wyoming: Fluid-Inclusion Evidence. *Geology*, 16, 1077-1080.
- Bishop, J.L., 2001. Mineralogy considerations for the 2003 MER Site Selection and the Importance for Astrobiology (abstract), First Landing Site Workshop for 2003 Mars Exploration Rovers, NASA Ames Research Center, Mountain View, CA, no. 9011.
- Boynton, W.V., W.C. Feldman, S.W. Squyres, T. Prettyman, J. Brückner, L.G. Evans, R.C. Reedy, R. Starr, J.R. Arnold, D.M. Drake, P.A. J. Englert, A.E. Metzger, Igor Mitrofanov, J.I. Trombka, C. d'Uston, H. Wänke, O. Gasnault, D.K. Hamara, D.M. Janes, R. L. Marcialis, S. Maurice, I. Mikheeva, G.J. Taylor, R. Tokar and C. Shinohara, 2002. Distribution of Hydrogen in the Near-Surface of Mars: Evidence for Sub-surface Ice Deposits. *Science*, 297, 81-85.
- Brock, T.D., 1994. Life at High Temperatures. Yellowstone Association for Natural Science, History & Education, Inc., Wyoming, 31 pp.
- Bryan, T.S., 1995. The Geysers of Yellowstone, Third Edition. University Press of Colorado, Colorado, 462 pp.
- Bryan, T.S., 2000. The Geyser Fields of the World. Yellowstone Interpretive Training Presentation, 12 pp.
- Bulmer, M.H. and T. Gregg, 1998. Apollinaris Patera: An Assessment Based on the 2001 Landing Site Evaluation Criteria. Mars Surveyor 2001 Landing Site Workshop, NASA Ames-Research Center, Moffett Field, CA, 1-6.
- Chesterman, C., 1979. National Audubon Society Field Guide to North American Rocks and Minerals. Alfred A. Knopf, Inc., New York, 850 pp.
- Christensen, P.R. B.M. Jakosky, H.H. Kieffer, M.C. Malin, H.Y. McSween, K. Nealson, G. Mehall, S. Silverman, S. Ferry, 1999. The Thermal Emission Imaging System (THEMIS) Instrument for the 2002 Orbiter (abstract). *Lunar Planet. Sci.* XXX, no. 1470.
- Christensen, P.R., J.L. Bandfield, M.D. Smith, V.E. Hamilton, and R.N. Clark, 2000 (a). Identification of a Basaltic Component on the Martian Surface from Thermal Emission Spectrometer Data. *J. Geophys. Res.*, v. 105, E4, 9609-9621.
- Christensen, P.R., R.L. Clark, H.H. Kieffer, M.C. Malin, J.C. Pearl, J.L. Banfield, K.S. Edgett, V.E. Hamilton, T. Hoefen, M.D. Lane, R.V. Morris, R. Pearson, T. Rousch, S.W. Ruff, and M.D. Smith, 2000 (b). Detection of Crystalline Hematite Mineralization on Mars by the

- Thermal Emission Spectrometer: Evidence for Near-surface Water. *J. Geophys. Res.*, v. 105, E4, 9623-9642.
- Christiansen, R.L. 1982. Late Cenozoic volcanism of the Island Park area, eastern Idaho. *Cenozoic Geology of Idaho: Idaho Bureau of Mines and Geol. Bull.* 26, edited by B. Bonnicksen and R.M. Breckenridge, 345-368.
- Christiansen, R.L., 1984. Yellowstone Magmatic Evolution: Its Bearing on Understanding Large-Volume Explosive Volcanism. In *Studies in Geophysics: Explosive Volcanism: Inception, Evolution, and Hazards*. Natl. Acad. Press, Washington, D.C., 84-95.
- Clark, R.N., G.A. Swayze, A. Gallagher, A., N. Gorelick, Kruse, F., 1991. Mapping with Imaging Spectrometer Data Using the Complete Band Shape Least-Squares Algorithm Simultaneously Fit to Multiple Spectral Features from Multiple Materials. *AVIRIS Airborne Geosci. Workshop Proc.* 1991, 1-2.
- Clark, R.N., 1993. Mapping Minerals with Imaging Spectroscopy. *USGS Office of Mineral Services Bull.* 2039, 141-150.
- Dohm, J.M., V.R. Baker, R.C. Anderson, D.H. Scott, J.W. Jr. Rice, and T.M. Hare, 2000. Identifying Martian Hydrothermal Sites: Geological Investigation Utilizing Multiple Datasets (abstract). *Lunar Planet. Sci. XXXI (CD-ROM)*, no.1613.
- Embree, G.F. and R.D. Hoggan, 1999. Secondary Deformation Within the Huckleberry Ridge Tuff and Subadjacent Pliocene Units Near the Teton Dam: Road Log to the Regional Geology of the Eastern Margin of the Snake River Plain, Idaho. In *Guidebook to the Geology of Eastern Idaho*, edited by S.S. Hughes and G.D. Thackray, Idaho Museum of Natural History, Idaho, 181-202.
- Farmer, J.D., S. Cady, and D.J. DesMarais, 1995. Fossilization Processes in Thermal Springs. *Geological Society of America, Abstracts with Programs*, 27(6), 305.
- Farmer, J.D., 1996. Hydrothermal Processes on Mars: An Assessment of Present Evidence, in *Evolution of Hydrothermal Ecosystems on Earth (and Mars?)*. John Wiley and Sons, England, 273-299.
- Farmer, J.D., 1998. Site Selection for Mars Exopaleontology in 2001 (abstract). *Mars Surveyor 2001 Landing Site Workshop*, NASA Ames-Research Center, Moffett Field, CA.
- Farmer, J.D. and D.J. DesMarais, 1999. Exploring for a record of ancient Martian life. *J. Geophys. Res.*, 104, E11, 26977-26995.
- Farmer, J.D., 2000. Hydrothermal Systems: Doorways to Early Biosphere Evolution. *GSA Today*, v. 10, no. 7, 1-11.
- Fournier, R.O. and A.M. Pitt, 1985. The Yellowstone Magmatic-Hydrothermal System. *Trans. Geotherm. Counc. Int. Symp. Geotherm. Energy*, edited by C. Stone, Int., 319-327.
- Fournier, R.O., 1989. Geochemistry and Dynamics of the Yellowstone National Park Hydrothermal System, *Ann. Rev. Earth Planet. Sci.* 17, 13-53.
- Fournier, R.O., R. Christiansen, R.A. Hutchinson, and K. Pierce, 1994. A Field Trip Guide to Yellowstone National Park, Wyoming, Montana, and Idaho – Volcanic, Hydrothermal, and Glacial activity in the Region. *USGS Geol. Surv. Bull.* 2099, United States Government Printing Office, Washington, 10-22.
- Francis, P., 1993. *Volcanoes: A Planetary Perspective*. Oxford University Press, New York, 443 pp.

- Franke, M.A. 2000. Yellowstone in the afterglow: Lessons from the fires. National Park Service, Mammoth Hot Springs, Wyoming, YCRNR200003.
- Gillespie, A.R., A.B. Kahle, and F. D. Palluconi, 1984. Mapping alluvial fans in Death Valley, California, using multichannel thermal infrared images, *Geophys. Res. Let.*, 11, 1153-1156.
- Grant, J. and M. Golombek, 2002. Overview of the Landing Site Selection Process and Workshop Goals, 3<sup>rd</sup> 2003 Mars Exploration Rovers Landing Site Selection Workshop (Presentation).
- Green, R. O., M. L. Eastwood, C. M. Sarture, T. G. Chrien, M. Aronsson, B. J. Chippendale, J. A. Faust, B. E. Pavri, C. J. Chovit, M. Solis, M. R. Olah and Q. Williams, 1998. Imaging spectroscopy and the Airborne Visible/Infrared Imaging Spectrometer (AVIRIS). *Remote Sens. Environ.* 65, 3, 227-248.
- Guidry, S.A. and H. S. Chafetz, 1999. Preservation of Microbes in Geyserite and Siliceous Sinter: Yellowstone National Park, Wyoming (Abstract). *Lunar Planet. Sci. XXX* (CD-ROM), no. 1152.
- Gulick, V.C., 1998. Potential Mars Surveyor 2001 Landing Sites Near Apollinaris Patera (Abstract). Mars Surveyor 2001 Landing Site Workshop, NASA Ames-Research Center, Moffett Field, CA.
- Hellman, M.J. and M.S. Ramsey, 2001. Analysis of Hot Springs in Yellowstone National Park Using ASTER and AVIRIS Remote Sensing. *EOS Transactions, AGU*, 82:47, Fall Meet. Suppl., F1360.
- Hellman, M.J. and M.S. Ramsey, 2002. Analysis of Hot Springs and Associated Deposits in Yellowstone National Park Using ASTER and AVIRIS Remote Sensing. *J. Volc. Geotherm. Res.*, in review.
- Hook, S.J. and M. Rast, 1990. Mineralogic Mapping Using Airborne Visible Infrared Imaging Spectrometer (AVIRIS) Shortwave Infrared (SWIR) Data Acquired Over Cuprite, Nevada. *AVIRIS Airborne Geosci. Workshop Proc.* 1990, 199-207.
- Hook, S.J., A.R. Gabell, A.A. Green, P.S. Kealy, 1992. A Comparison of Techniques for Extracting Emissivity Information from Thermal Infrared Data for Geologic Studies. *Remote Sens. Environ.*, 42, 123-135.
- Hook, S.J., K.E. Karlstrom, C.F. Miller, and K.J.W. McCaffrey, 1994. Mapping the Piute Mountains, California, with Thermal Infrared Multispectral Scanner (TIMS) Images. *J. Geophys. Res.*, v. 99, 15,605-15, 622.
- Hunt, G.R., 1980. Electromagnetic radiation: The communication link in remote sensing, in *Remote Sensing in Geology*, edited by B.S. Siegel and A.R. Gillespie, John Wiley, New York, 5-45.
- Huntington, J.F., 1996. The Role of Remote Sensing in Finding Hydrothermal Mineral Deposits on Earth, in *Evolution of Hydrothermal Ecosystems on Earth (and Mars?)*. John Wiley and Sons, England, 214-234.
- Kahle, A.B., 1987. Surface emittance, temperature, and thermal inertia derived from thermal infrared multispectral scanner (TIMS) data for Death Valley, California. *Geophysics*, 52, 858-874.
- Kahle, A.B., F.D. Palluconi, S.J. Hook, V.J. Realmuto, and G. Bothwell, 1991. The Advanced Spaceborne Thermal Emission and Reflectance Radiometer (ASTER). *Int. J. Imaging Systems and Technology*, v. 3, 144-156.

- Kokaly, R.F., R.N. Clark, and K.E. Livo, 1998. Mapping the Biology and Mineralogy of Yellowstone National Park Using Imaging Spectroscopy. Summaries of the 7th Annual JPL Airborne Earth Science Workshop, JPL Publication 97-21, v. 1, 245-254.
- Kruse, F., 1999. Mapping Hot Spring Deposits with AVIRIS at Steamboat Springs, Nevada. AVIRIS Airborne Geosci. Workshop Proc. 1999, 1-7.
- Macenka, S.A. and Chrisp, M.P., 1987. Airborne Visible/Infrared Imaging Spectrometer (AVIRIS) Spectrometer Design and Performance. JPL Publication 87-38, 13-24.
- Marler, G.D., 1964. Studies of Geysers and Hot Springs along the Firehole River, Yellowstone National Park, Wyoming. Yellowstone Library and Museum Association, 1-49.
- Nash, G.D. and G.W. Johnson, 2002. Soil Mineralogy Anomaly Detection in Dixie Valley, Nevada Using Hyperspectral Data. Proc. of the Twenty-Seventh Workshop on Geothermal Reservoir Engineering, Stanford University, California, SGP-TR-171.
- Nelson, D.M., J.D. Farmer, R. Greeley, H.P. Klein, R.O. Kuzmin, 1999. Geology and Landing Sites of the Elysium Basin-Terra Cimmeria Region, Mars. Proc. Second Mars Landing Site Workshop, State University of Buffalo, Buffalo, NY, 71-73.
- Newsom, H., C. Barber, I. Thorsos, 2002. MER 2003 Landing Sites – Impact Crater Lake and Hydrothermal Deposits, 3<sup>rd</sup> 2003 Mars Exploration Rovers Landing Site Selection Workshop, no. 9008, 1-2.
- Porter, W.M. and H.T. Enmark, 1987. A System Overview of the Airborne Visible/Infrared Imaging Spectrometer (AVIRIS). JPL Publication 87-38, 3-12.
- Ramsey, M.S., P.R. Christensen, N. Lancaster, and D.A. Howard, 1999. Identification of sand sources and transport pathways at the Kelso Dunes, California using thermal infrared remote sensing, *Geol. Soc. Amer. Bull.*, 111, 646-662.
- Ramsey, M.S. and L.P. Flynn, 2002. Strategies, Insights, and the Recent Advances in Volcanic Monitoring and Mapping with data from the Earth Observing System. *J. Volc. Geotherm. Res.*, in review.
- Ramsey, M.S. and Dehn, J., 2002. Spaceborne observations of the 2000 Bezymianny, Kamchatka eruption: The integration of high-resolution ASTER data into near real-time monitoring using AVHRR. *J. Volc. Geotherm. Res.*, in review.
- Realmuto, V.J., 1990. Separating the Effects of Temperature and Emissivity: Emissivity Spectrum Normalization, Proc. of the Second Annual Thermal Infrared Multispectral Scanner (TIMS) Workshop. In: Abbott, E.A. (Ed.), Proc. Sec. Therm. Infrared Multispectral Scanner (TIMS) Workshop, Jet Propulsion Lab. Pub. 90-55, pp. 31-36.
- Ruiz-Armenta, J.R. and R.M. Prol-Ledesma, 1998. Techniques for Enhancing the Spectral Response of Hydrothermal Alteration Minerals in Thematic Mapper Images of Central Mexico. *Int. J. Remote Sens.*, 19, v. 10, 1981-2000.
- Sabins, F.F., 1999. Remote Sensing for Mineral Exploration. *Ore Geol. Reviews*, 14, 157-183.
- Salisbury, J.W., and D.M. D'Aria, 1992. Emissivity of terrestrial materials in the 8-14  $\mu\text{m}$  atmospheric window, *Remote Sens. Environ.*, 42, 83-106.
- Schreier, C., 1992, *A Field Guide to Yellowstone's Geysers, Hot Springs, and Fumaroles*, Homestead Publishing, Moose, Wyoming, 128 pp.
- Seelos, F.P. and R.E. Arvidson, 2002. Remote Sensing Properties of Exhumed Deposits in the Terra Meridiani Region of Mars, 3<sup>rd</sup> 2003 Mars Exploration Rovers Landing Site Selection Workshop (Presentation).
- Smith, R.B. and L.J. Siegel, 2000. *Windows Into the Earth: The Geologic Story of Yellowstone and the Grand National Teton Parks*. Oxford University Press, New York, 242 pp.

- Spruce, J.P., 2001. Low Altitude AVIRIS Data for Mapping Land Cover in Yellowstone National Park: Use of ISODATA Clustering Techniques. AVIRIS Airborne Geosci. Workshop Proc. 2001, 1-10.
- Sultan, M., Arvidson, R.E., Sturchio, N.C., and Guinness, E.A., 1987. Lithologic mapping in arid regions with Landsat Thematic Mapper data: Meatiq dome, Egypt. Geol. Soc. Amer. Bull. 99, 748-762.
- Thome, K., K. Arai, S. Hook, H. Kieffer, H. Lang, T. Matsunaga, A. Ono, F. Palluconi, H. Sakuma, P. Slater, T. Takashima, H. Tonooka, S. Tsuchida, R.M. Welch and E. Zalewski. 1998. ASTER Preflight and Inflight Calibration and the Validation of Level 2 Products. IEEE Trans. on Geosci. Rem. Sens., 36, 4, 1161-1172.
- Vane, G., W.M. Porter, J.H. Reimer, T.G. Chrien and R.O. Green, 1987. AVIRIS Performance During the 1987 Flight Season: An AVIRIS Project Assessment and Summary of the NASA-Sponsored Performance Evaluation. AVIRIS Airborne Geosci. Workshop Proc. 1987, 1-20.
- Vincent, R.K., P.K. Pleitner, and M.L. Wilson, 1984. Integration of Airborne Thematic Mapper and Thermal Infrared Multispectral Scanner Data for Lithologic and Hydrothermal Alteration Mapping. In Proc. of the International Symposium on Remote Sensing of the Environment, Third Thematic Conference, Remote Sens. for Exploration Geol., v. 1, 219-226.
- Vincent, R.K., 1997. Fundamentals of Geological and Environmental Remote Sensing. Prentice-Hall, Inc., New Jersey, 366 pp.
- Wade, M.L., D.G. Agresti, T.J. Wdowiak, L.P. Armendarez, and J.D. Farmer, 1999. A Mössbauer Investigation of Iron-rich Terrestrial Hydrothermal Vent Systems: Lessons for Mars Exploration. J. Geophys. Res., 104, E4, 8489-8507.
- Walter, M.R. and D.J. DesMarais, 1993. Preservation of Biological Information in Thermal Spring Deposits: Developing a Strategy for the Search for Fossil Life on Mars. Icarus, 101, 129-143.
- Wohletz, K. and G. Heiken, 1992. Volcanology and Geothermal Energy. University of California Press, California, 432 pp.
- Yamaguchi, Y., A. B. Kahle, H. Tsu, T. Kawakami, and M. Pniel, 1998. Overview of the Advanced Spaceborne Thermal Emission And Reflectance Radiometer (ASTER), IEEE Trans. Geosci. Rem. Sens., 36, 1062-1071.
- Yuhas, R.H., A.F.H. Goetz, J.W. Boardman, 1992. Discrimination Among Semi-Arid Landscape Endmembers Using The Spectral Angle Mapper Algorithm (SAM). AVIRIS Airborne Geosci. Workshop Proc. 1992. 147-149.

#### **Instrument Websites:**

- ASTER Website: <http://asterweb.jpl.nasa.gov/>
- AVIRIS Website: <http://malaku.jpl.nasa.gov/aviris.html>
- TES Website: <http://tes.asu.edu/>
- THEMIS Website: <http://themis.la.asu.edu/>